1-1-2011

Pathological and Biomedical Characteristics of Spinal Cord Injury Determined Using Diffusion Tensor Imaging

Tsang-Wei Tu
Washington University in St. Louis

WASHINGTON UNIVERSITY IN ST. LOUIS

Department of Mechanical Engineering and Materials Science

Dissertation Examination Committee:

Philip V. Bayly, Chair
Sheng-Kwei Song, Co-Chair
Joseph J.H. Ackerman
Ramesh K. Agarwal
Guy M. Genin
Larry A. Taber

Pathological and Biomedical Characteristics of Spinal Cord Injury Determined Using Diffusion Tensor Imaging

by

Tsang-Wei Tu

A dissertation presented to the
Graduate School of Arts and Sciences
of Washington University in
partial fulfillment of the
requirements for the degree
of Doctor of Philosophy

August 2011

Saint Louis, Missouri

Abstract

Traumatic spinal cord injury (SCI) is the most devastating injury that often causes the victim permanent paralysis and undergo a lifetime of therapy and care. It is caused by a mechanical impact that ultimately causes pathophysiological consequences which at this moment in time are an unresolved scientific challenge of great social impact. Scientists have long used animal contusion models to study the pathophysiology of SCI in the discovery of progressive secondary tissue degeneration, demyelination, and apoptosis. More importantly, most therapies that have gone to human clinical trial were first validated in spinal cord contusion models.

Magnetic resonance imaging (MRI) is the modality of choice to noninvasively detect the soft tissue injury, particularly suitable for assessing the tissue integrity in SCI. However, the convention MRI lacks capability of detecting and evaluating the injury severity acutely, probably resulting in lost opportunities of effective prognostication or treatment stratification for SCI patients. Diffusion Tensor Magnetic Resonance Imaging (DTMRI, DTI) is an emerging technique known to provide dynamic contrast reflecting the progression of the underlying pathology in CNS tissues. In this study, we hypothesized that axial ($\lambda_{\parallel}$) and radial ($\lambda_{\perp}$) diffusivity derived from DTI is sensitive to the pathological alteration in spinal cord white matter (WM) tract and could be used as potential biomarkers detecting and characterizing the axonal and myelin damage in SCI.

A mouse model of contusion SCI was examined using DTI, behavioral assessment, and histology to test our hypothesis. Techniques employed including the simplification of diffusion weighting scheme, the implementation of diffusion weighted multiple spin-echo sequence, and verified for setting up the experimental protocol and data processing procedures. Secondly, the hypothesis was test on the projects comparing the change of these biomarkers on both the myelinated and dysmyelinated shiverer mice cooperating with histological analysis, and behavioral assessment. Finally, a finite element analysis (FEA) of contusion SCI was deployed to provide evidences of injury mechanics correlated with the injury patterns detected by diffusion MRI for a better characterized animal model of contusion SCI.

Acknowledgements

This dissertation is the result of many years of continuous work which I have been supported and encouraged by many people. I am in debt to many professors, family members and friends who directly or indirectly have contributed to this work. First, I would like to thank my advisor, Dr. Sheng-Kwei Song for his guidance, commitment and mentoring during these years at Washington University. Being trained as a hydraulic engineer, I very appreciate the chance he gave me to try out in the biomedical MR lab when I knew nothing about MR and neuroscience, a completely different world to me. His expertise in animal models made this study a fascinating experience, which allowed me to grow not only as an engineer but as a person too. Having the opportunity of working with Professor Song has been a challenge and an honor for me.

I am also grateful to Dr. Philip Bayly for his valuable helps and ideas with the finite element analysis portion of this dissertation. His idea inspired me to utilize my engineer expertise and just learned MR technology on solving a complex biological question, the direction I would like to pursue in the future. Dr. Joong Hee Kim, the master who trained me after I joined Dr. Song's lab, is another person I would like to express my gratitude. Not only the experiment skills but also his insistence of perfection in experimental design and data has taught me a great deal. I would also like to express my sincerest gratitude to the members of my committee, Dr. Joseph Ackerman, Dr. Ramesh Agarwal, Dr. Guy Genin, Dr. Larry Taber, for their time, help and support. Their valuable comments, suggestions and technical insights greatly developed and improved the content of this dissertation.

I would like to take this opportunity to thank my former and recent colleagues at the Biomedical MR Laboratory, in particular Dr. William Spees, John Engelbach, Dr. Mark Conradi, Ying-Jr Amanda Chen, Chia-Wen Chiang, Tsen-Hsuen Lin, Dr. Mingqiang Xie, Dr. Qing Wang, Dr. Yong Wang, Dr. Peng Sun, Dr. Matt Budde, Dr. Jeff Anderson, and Jun-Yi Yin for their collaboration, suggestions and great assistance. I wish to thank the faculty in the BMRL for providing such a great environment of learning the world of MR. I also like to thank the University of Missouri Spinal Cord Injury Program for giving me the financial support on finite element analysis – DTI studies. I also like to thank my friends who fulfill my life these years in St. Louis, where a place was completely new to me six year ago and now another home!

I cannot finish without expressing my deepest gratitude to family in Taiwan for their continuous support, dedication, love, patience and encouragement during my study away from home.

Tsang-Wei William Tu
Washington University in St. Louis
August 2011

To my family, the best of my love

Table of Contents

List of Figures

List of Tables

Nomenclature and Abbreviations

Nomenclature

S_0	Signal Intensity of a spin echo without diffusion weighted
S	Diffusion weighted signal intensity
M_z	Longitudinal Magnetization
t	Time
TR	Repetition Time
TE	Echo Time,
T1	Spin-Lattice relaxation time
T2	Spin-Spin relaxation time
D	Diffusion coefficient
$\vec{G}(t)$	Diffusion-sensitizing gradient
$\varphi(t)$	Spatially dependent phase shift
$< \varphi^2 >$	Variance of a Gaussian phase distribution
γ	Gyromagnetic ratio
B_0	Static magnetic field
$\vec{r}(t)$	Location of nuclear spin
Δ	Time between the onset of the first and second gradient pulses
δ	Time between the onset of a trapezoidal pulse and the end of its plateau
ε	Rise time of the trapezoidal ramp
b	Diffusion weighting factor
b_d	Diffusion gradients
b_i	Imaging gradients
b_{di}	Cross-terms of both diffusion gradients and imaging gradients
b_d	Desired diffusion gradient
η	White noise
v_i	Eigenvectors of diffusion tensor
λ_i	Eigenvalues of diffusion tensor
Tr	Trace of diffusion tensor
<D>	Mean apparent diffusion coefficient
$\lambda_{\|\|}$	Axial diffusivity
$\lambda_{\perp}$	Radial diffusivity
$D_{\|\|}$	Parallel Diffusivity
$D_{\perp}$	Perpendicular Diffusivity
d_i	*i*th complex data value
A_i	Amplitude of the *i*th signal value
θ	Phase of the *i*th signal value
n_i	Complex noise
dR_i	Real part of the *i*th complex signal
dI_i	Imaginary part of the *i*th complex signal
n_{Ri}	Real part of the complex noise
n_{Ii}	Imaginary part of the complex noise
σ	Standard deviation of the noise prior probability
D	All of the imaging data
I	Background information

$P(\theta\|\sigma DI)$	Posterior probability for the phase
$P(\theta\|\sigma I)$	Prior probability for the phase
$P(A\|\sigma I)$	Joint prior probability for the amplitudes
W	Constants derived from the sufficient statistic of the phase
X	Constants derived from the sufficient statistic of the amplitude
$\widehat{\boldsymbol{\theta}}$	Estimated voxel-wise phase
S_i	Original signal
S_{pi}	Phased signal
U	Hyperelastic strain energy density function
$\bar{\boldsymbol{\lambda}}_{\boldsymbol{\iota}}$	Deviatoric principal stretches
N	Material Parameter
μ_i, α_i, D_i	Temperature-dependent material parameters
μ_0	Initial shear modulus
K_0	Bulk modulus
ν	Poisson's ratio
J^{el}	Elastic volume ratio
$\bar{I}_1$, $\bar{I}_2$	First and second deviatoric strain invariants
C_{10}, C_{01}	Temperature-dependent material parameters
τ_k	Characteristic relaxation time constants in prony series
g_k	Relative relaxations in prony series

Abbreviations

MRI	Magnetic resonance imaging
NMR	Nuclear magnetic resonance
DTI	Diffusion tensor imaging
DTMRI	Diffusion tensor magnetic resonance imaging
DWI	Diffusion weighted imaging
SCI	Spinal cord injury
CNS	Central nerve system
WM	White matter
VLWM	Ventral-lateral white matter
DWM	Dorsal white matter
GM	Gray matter
CSF	Cerebrospinal fluid
FE	Finite element
FEA	Finite element analysis
SMI31	Phosphorylated neurofilament protein
EC/CV	Erithryna cristagalli / Crystal violet
MBP	Myelin basic protein
LFB	Laxol fast blue
PBS	Phosphate buffered saline
BMS	Basso mouse scale
OSU	Ohio state university
ESCID	Electromagnetic spinal cord injury device
IH	Infinite horizon
SD	Standard deviation
FOV	Field of view

T1	Spin-lattice relaxation
T2	Spin-spin relaxation
TR	Repetition time
TE	Echo time
ΔTE	Inter-echo spacing
CPMG	Carr-Purcell Meiboon-Gill
SNR	Signal to noise ratio
PE	Phase encoding
FE	Frequency encoding
RO	Readout
SS	Slice selection
DW	Diffusion weighted
MSE	Multiple spin echo
MAG	Magnitude
ABS	Absorption
FSE	Fast spin echo
EPI	Echo planar imaging
SE	Spin echo
MD	Mean diffusivity
YFP	Yellow florescence protein
FA	Fractional anisotropy
RA	Relative anisotropy
Asd	Anisotropy standard deviation
AI	Anisotropy index
DAI	Diffusion anisotropy index
RF	Radio frequency
DPI	Days post injury
ADC	Apparent diffusion coefficient
ROI	Region of interest
MSP	Maximum principal strain

Chapter 1. Introduction

Spinal cord together with brain makes up the central nerve system (CNS). It is a tubular bundle of nerves that is encased in the bony vertebral column and is attached to the brain stem [1, 2]. The spinal cord connects the peripheral nervous system for transmitting neural signals between the brain and the rest of the body and also acts as a minor coordinating center responsible for some simple reflexes, such as the withdrawal reflex. The peripheral region of the cord contains sensory and motor white matter (WM) tracts. Internal to this peripheral region is the gray, butterfly shaped central region made up of nerve cell bodies [2]. WM is composed of myelinated axons, which connect various gray matter (GM) areas of the brain to the peripheral tissues. The three meninges covering the spinal cord, the outer dura, the middle arachnoid, and the inner pia mater, are continuous with that in the brainstem and cerebral hemispheres (Fig. 1-1). Cerebrospinal fluid (CSF) in the subarachnoid space is also a part of the brain CSF. The cord is stabilized within the dura mater by the connecting denticulate ligaments which extend from the enveloping pia mater laterally between the dorsal and ventral roots. The dural matter ends at the vertebral level of the second sacral vertebra.

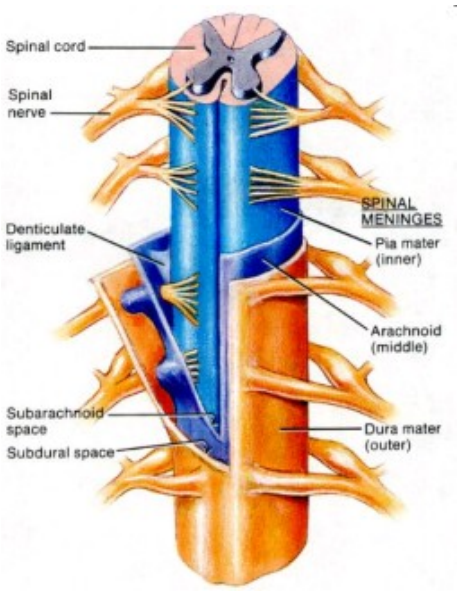

Figure 1-1. Structure of human spinal cord (Figure is adapted from www.homebusinessandfamilylife.com/spinal_cord.html).

1.1 Traumatic SCI and Animal Model

Traumatic spinal cord injury (SCI) is one of the most devastating injuries a person can suffer. It is typically associated with major trauma from motor vehicle accidents (37%), violence (28%), falls (21%), sports-related (6%), and other (8%) [3-5]. The SCI occurs when a traumatic event causes damage to the cells in the spinal cord or when the nerve tracts are severed that relay signals within the spinal cord. Most commonly, cord injuries include contusions (a bruising of the spinal cord), compressions (pressure put on the spinal cord), lacerations (nerve fibers which are severed or torn), and central cord syndrome (damage to the corticospinal tracts in the cervical region of the spinal cord) [6].

The estimated size of the population in the USA with traumatic spinal-cord injury is 183,000–230,000 with 11,000 cases of injury happen each year [3, 5, 7]. Average age at injury is 31 years, with the greatest frequency between 15 and 25 years; 82% of the

patient are male. Most human SCIs are caused by transient compression or contusion of the spinal cord, depending on where the spinal cord and nerve roots are damaged, the symptoms can vary widely, from pain to paralysis to incontinence. The average lifetime cost of treating an individual with traumatic spinal-cord injury is between US$500,000 and $2 million, dependent on factors such as extent and location of injury [5]. Total direct costs of caring for individuals with spinal-cord injury exceed $7 billion per year in the USA. However, SCIs at this moment in time are an unresolved scientific challenge of great social impact.

Scientists have long used animal spinal cord contusion models to study the pathophysiology of SCI [8-10]. Contusion models played a significant impact in the discovery of progressive secondary tissue damage, demyelination, and apoptosis in SCI. Most therapies that have gone to human clinical trial were first validated in spinal cord contusion models. In the model, spinal cord is compressed at the site of impact resulting in longitudinal lengthening of the neighboring segments mimicking the bruising of the spinal cord [11]. Tissue near the epicenter of the spinal cord is most vulnerable, suggesting that the mechanical loads are highest in this anatomical region. Large-caliber myelinated axons in the surrounding WM are highly susceptible to mechanical damage due to stress concentrated at the nodes of Ranvier [12]. The rate, magnitude, and duration of the biomechanical insult dictates the injury severity affecting functional outcome [10, 13].

Three devices are currently widely used for the study of spinal cord contusion injuries in rodents [10]. One of the earlier devices is the New York University impactor [14-16], which is designed as a weight-drop model. The two newer contusion models, the Ohio State University Electromagnetic SCI Device (ESCID) [9, 17, 18] and the Precision Systems and Instrumentation Infinite Horizons (IH) [19] impactors, are

displacement- and force-defined devices, respectively. All these devices can provide read-outs of tissue displacement, while the IH and ESCID devices can also measure the actual force delivered to the spinal cord upon impact. The Washington University SCI device was designed by Prof. Philip Bayly modifying from the OSU device using an electromagnetic actuator and a cantilever beam to generate a more controllable displacement of the indentation (Fig. 1-2) [20]. Laser displacement sensor, force load cell and accelerometer can be installed on the device for measuring the mechanical parameters during the indentation. The calibration curves of these units are presented in Fig. 1-3. The location and procedure of T9 contusion SCI are illustrated in Fig. 1-4.

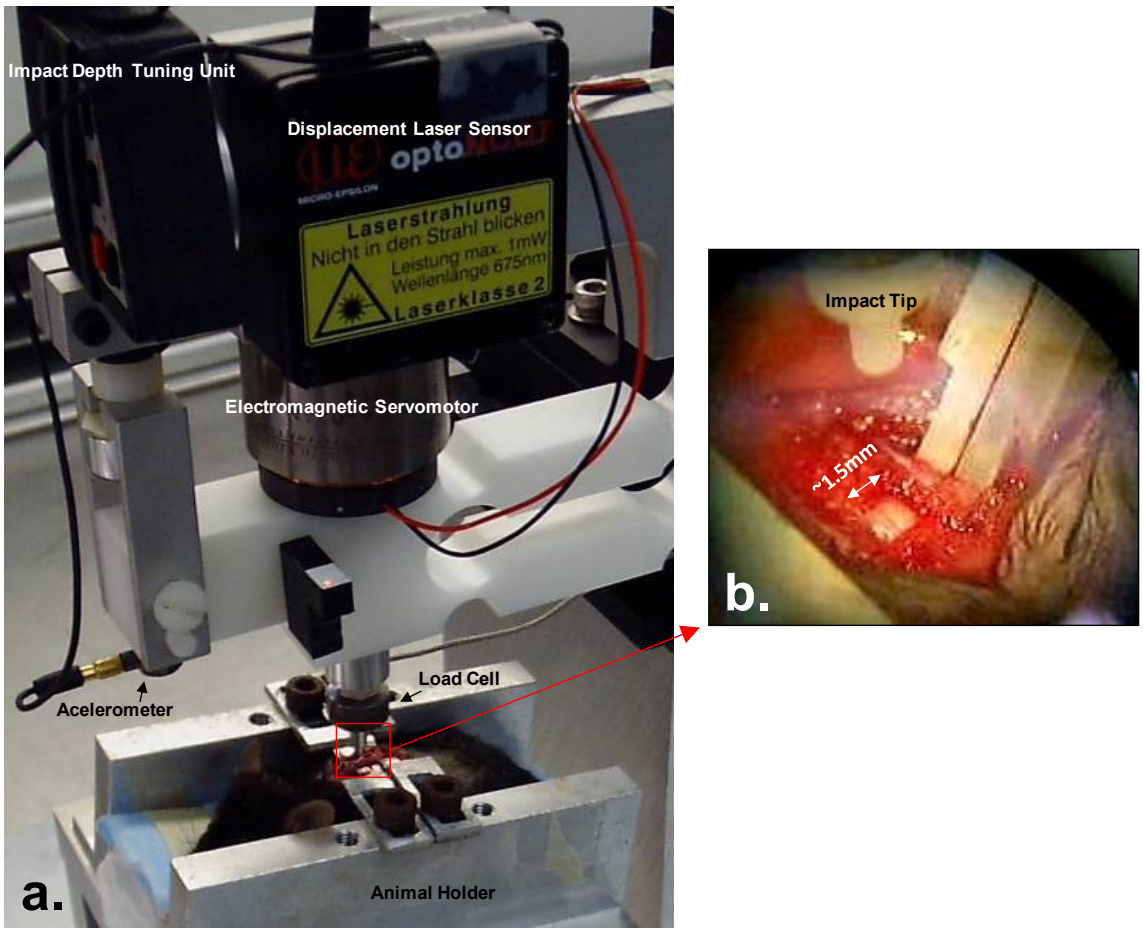

Figure 1-2. The Washington University impactor and functional components generating graded mouse SCI (a), the zoom-in picture of the laminectomy site and holding forceps (b).

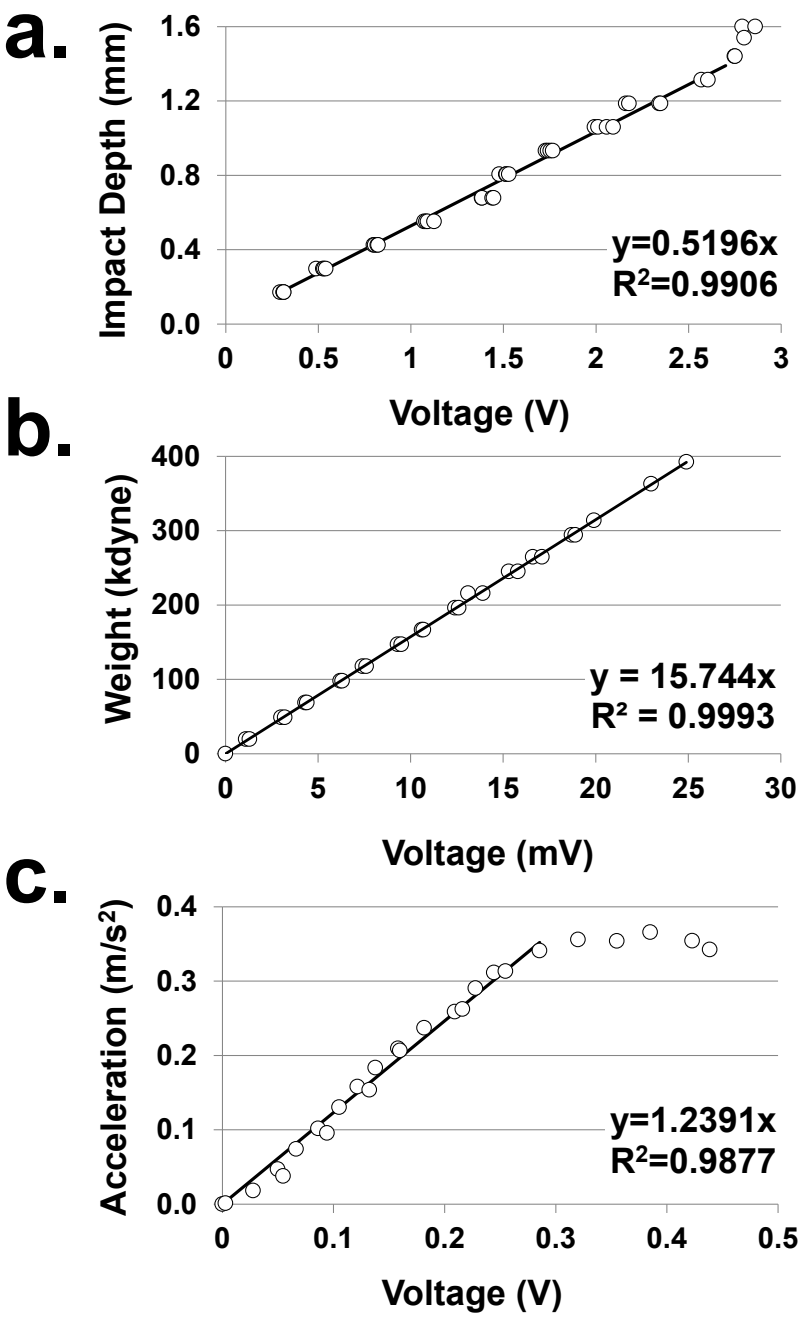

Figure 1-3. The calibration curves of the mechanical measurement units on the Washington University impactor, (a) Distance measuring laser sensor, (b) Load cell and (c) Accelerometer. The calibration curves demonstrate linear relationships between mechanical measurements on displacement, force and acceleration and voltage outputs suggesting accurate control of the unit.

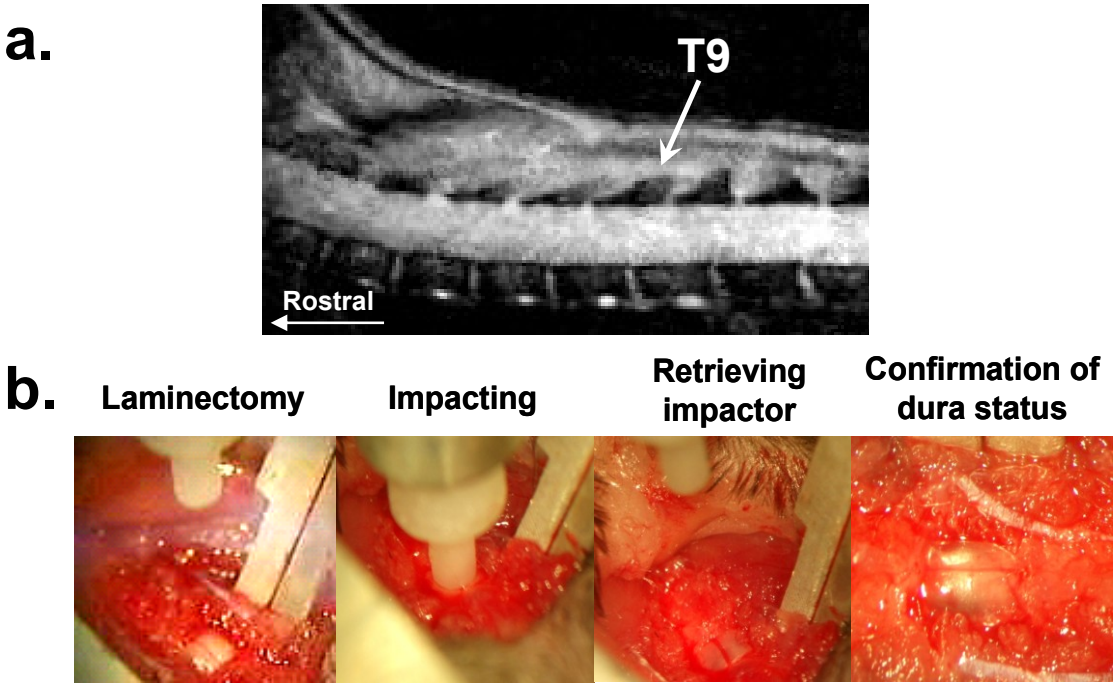

Figure 1-4. Surgical site (a) and sequential steps of SCI contusion (b). After dorsal laminectomy at the T9 vertebral level, mice received impact at 0.2 m/sec speed and displacement ranging from 0.3 – 1.0 mm utilizing Washington University impactor to generate graded contusion SCI.

1.3 Methods of Studying Spinal Cord Injury

Histological staining, behavioral assessment, computational simulation, and radiological imaging are the most common techniques for studying contusion SCI [8-13, 19, 21, 22]. Histological staining provides the most detail structural and pathophysiological alterations after contusion SCI. However, histological staining is invasive which may not reveal the *in vivo* conditions. Behavioral assessment characterizes the injury severities *in vivo* by grading the functional outcomes, yet not able to provide detail changes in tissue level. Computational simulation allows a direct comparison of the tissue level states of stress and strain to injury patterns and outcomes [23-27]. Still, a successful computational analysis relies on the comprehensive

understanding of the underlying tissue biomechanical properties and boundary conditions [10, 23-30]. In this section, a brief introduction on methods employed in this dissertation work studying contusion SCI will be presented. The imaging methods, constituting the core of this dissertation, will be described in details in the following several sections.

1.3.1 Behavioral Assessment: Basso Mouse Scale

After the SCI, animals are scored by the hind limb motor function using Basso Mouse Scale (BMS) over a certain recovery period [31]. The BMS is an open field test, with no prior training required, thus no training effect on the score. It is a 4-minute test performed by two or more evaluators for scoring mouse behaviors following the established deficit rule. The BMS was developed using stringent psychometric techniques to ensure accurate prediction of locomotor outcome and good agreement within and across laboratories [31]. Mouse recovery is tested by coordination, paw position and trunk instability, overall scoring from 9 (best) to 1 (worst); subscores from 11 (best) to 0 (worst) (Table 1-1).

Table 1-1. The standardized BMS scoring sheet used to record open field locomotor performance of mice. The score sheet is divided into seven locomotor categories for early (Ankle Movement), intermediate (Plantar Placement, Stepping), and late (Coordination, Paw Position, Trunk Instability, Tail) phases of recovery. The BMS score and subscore are calculated from data entered on the score sheet (Table is adapted from Basso, 2006).

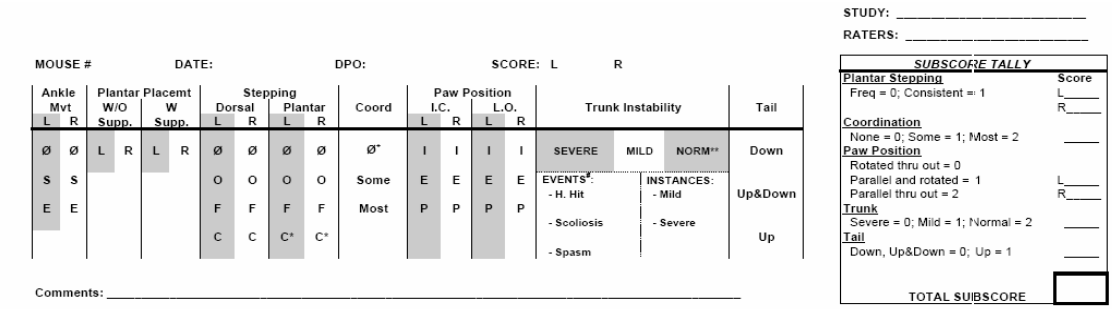

STUDY: _____

RATERS: _____

MOUSE # DATE: DPO: SCORE: L R

Ankle Mvt L	Ankle Mvt R	Plantar Placemt W/O Supp. L	Plantar Placemt W/O Supp. R	Plantar Placemt W Supp. L	Plantar Placemt W Supp. R	Stepping Dorsal L	Stepping Dorsal R	Stepping Plantar L	Stepping Plantar R	Coord	Paw Position I.C. L	Paw Position I.C. R	Paw Position L.O. L	Paw Position L.O. R	Trunk Instability	Tail
Ø	Ø	L	R	L	R	Ø	Ø	Ø	Ø	Ø*	I	I	I	I	SEVERE MILD NORM**	Down
S	S					O	O	O	O	Some	E	E	E	E	EVENTS#: - H. Hit - Scoliosis - Spasm	INSTANCES: - Mild - Severe	Up&Down
E	E					F	F	F	F	Most	P	P	P	P			
						C	C	C*	C*							Up

Comments: _____

SUBSCORE TALLY	
Plantar Stepping	Score
Freq = 0; Consistent = 1	L_____ R_____
Coordination	
None = 0; Some = 1; Most = 2	_____
Paw Position	
Rotated thru out = 0	
Parallel and rotated = 1	L_____
Parallel thru out = 2	R_____
Trunk	
Severe = 0; Mild = 1; Normal = 2	_____
Tail	
Down, Up&Down = 0; Up = 1	_____
TOTAL SUBSCORE	

BMS scores for locomotion over the 21-day period showed a complete recovery in the control group, laminectomy only, while the SCI group showed only partial recovery (Fig. 1-5). Both groups reached plateaus of locomotion recovery around 7 days post injury (DPI). The impact distant at 0.8 mm induced a moderate SCI significantly lower BMS scores (BMS ~ 5) from the control value (BMS ~ 9).

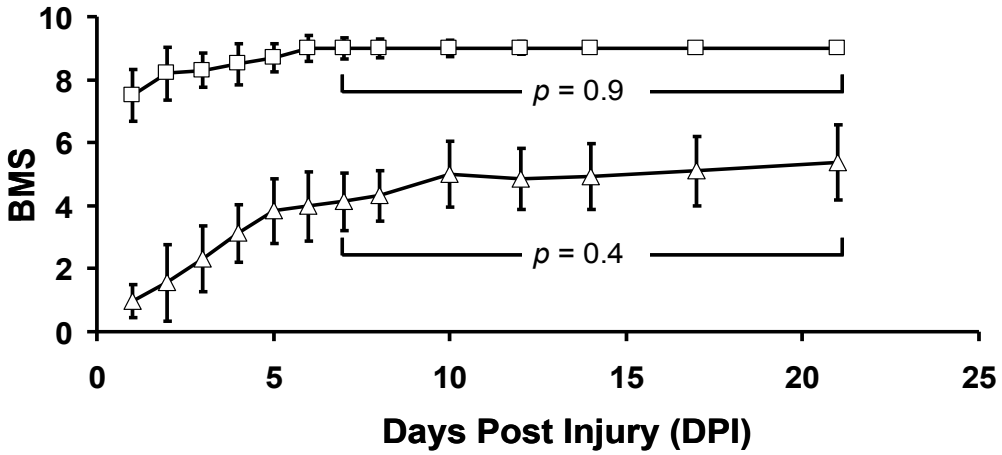

Figure 1-5. Both control and SCI animals showed a significant decrease of hind limb motor function immediately after injury. The recovery from surgery and traumatic event on spinal cords was observed in the sub-acute phase. This steady-state BMS scores are required for precise evaluation of the preserved neuro-function in the contusion SCI. From 7 DPI till the end of the study, the observed BMS scores did not show a statistically significant difference over time.

1.3.2 Histological Analysis

When the animals are ready for histological analysis, they receive a trans-cardiac perfusion under deep anesthesia with 50 mL of 0.1 M phosphate-buffered saline (PBS) (pH 7.4) followed by 200 mL of 0.1 M PBS containing 4% paraformaldehyde (pH 7.4) [9, 20, 32-36]. Following the fixation, the spine is excised, left in the fixative overnight, and decalcified for 48 hr, embedded in paraffin, and then sectioned on a sliding microtome (5 μm). Immunocytochemically, phosphorylated neurofilament staining (SMI31) is performed for axons; myelin basic protein (MBP) or Laxol fast blue (LFB) is used to stain for myelin integrity (Fig. 1-6). Histological sections are examined by a Nikon Eclipse 80i microscope equipped with a 60× oil objective, and digital images will be captured with a Photometrics CCD digital camera using MetaMorph image acquisition software. A Zeiss

(Oberkochen, Germany) LSM510-META laser scanning confocal microscope is used for imaging axons of Ventral-lateral WM (VLWM) using the Z-stack mode (5 optical sections in the z-axis) using a 4x, 10x, and 20x (water immersion; numerical aperture, 1.2) lens with a 488 nm argon laser.

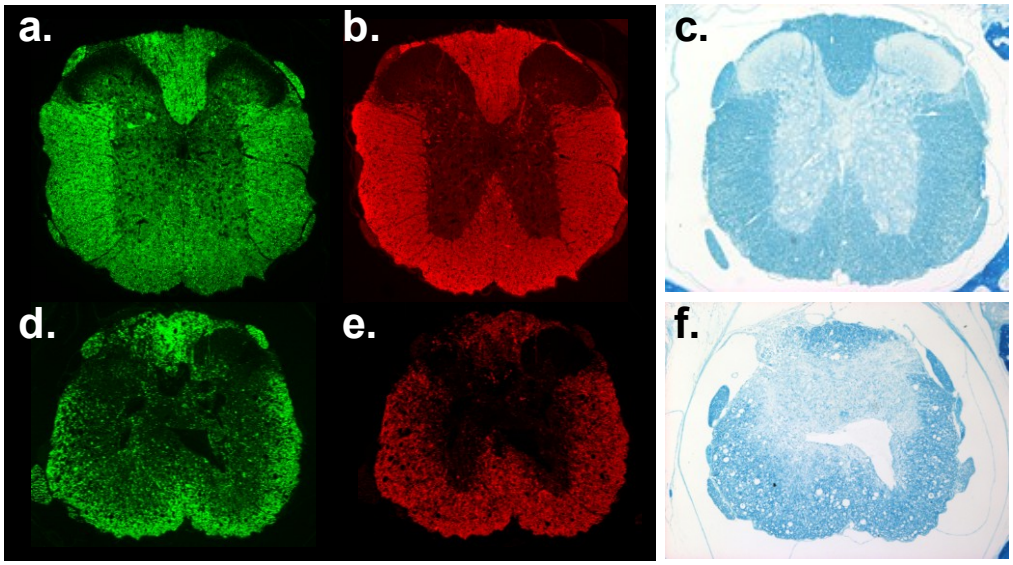

Figure 1-6. Representative histological staining of the control (a, b, c) and injured (d, e, f) mouse spinal cords, (a, d) The SMI31 reacts with a phosphorylated epitope in extensively phosphorylated neurofilament in most mammalian species. (b, e) The Myelin basic protein (MBP) stains for the major constituent of the myelin sheath of oligodendrocytes in the central nervous system. (c, f) The Luxol fast blue stain (LFB) is a commonly used stain to observe myelin under light microscopy. It is the alcohol soluble counterpart of the water soluble alcian blue. The stain works via an acid-base reaction with the base of the lipoprotein in myelin replacing the base of the dye and causing a colour change. Under the stain, myelin fibers appear blue, neutrophil appears pink, and nerve cells appear purple.

1.3.3 Computational Simulation

Computational simulation, such as finite element analysis (FEA), is a numerical technique for finding approximate solutions of partial differential equations and integral

equations [37]. The solution is based on rendering the partial differential equations into an approximating system of ordinary differential equations to be numerically integrated using standard techniques, such as Euler's method and Runge-Kutta method. The FEA is a powerful tool for solving the partial differential equations over complicated domains, when the domain changes, when the desired precision varies over the entire domain, or when the solution lacks smoothness. In SCI, FEA offers a theoretical insight of the tissue level states of stress and strain to injury patterns and predicts injury outcomes [23, 25, 38-40].

FEA simulation in SCI research has been frequently conducted using 2D models due to the longitudinal uniformity of spinal cord structure [24, 30, 41, 42]. Recently, several 3D models have been proposed using simplified geometry of the spinal cord [23, 25, 27]. The 3D model provides insight of the spatial distribution of stress and strain within the spinal cord. We contend that the current FEA model of SCI may be augmented by a noninvasive diagnostic technique that is capable of assessing structural and functional abnormalities *in vivo*. In this dissertation, a commercial FEA software package, Abaqus, was used for the contusion SCI simulation [37]. Abaqus is initially designed to address non-linear physical behavior in 1978. As a result, the package has an extensive range of material models such as hyperelastic material capabilities needed for tissue mechanics. The product is popular with academic and research institutions and has been extensively used in the automotive, aerospace, and industrial products industries.

We started our FEA simulation from a simplified transverse 2D case, which assumed a tube uniform in the longitudinal direction. The impactor therefore became a slate of rigid solid body. The geometry and material property of the 2-D model was

simply a semicircle with hyperelastic and viscoelastic material (Fig. 1-7a). Another 2-D case was developed to show the von-Mises stress from sagittal view (Fig. 1-7b). The boundary conditions were encastred on the downward surface. The hyperelastic material allowed large deformation during the indentation. The 2D simulation provided an unsophisticated examination at the impact site though it failed to reveal the spatial transition. Further than the 2D cases, several more complex 3D cases were built to show the spatial distribution of the stress and strain. The indentation of a hyperelastic cube was first developed (Fig. 1-7c), following a case of a hyperelastic tube of gel placed on a rigid arc (Fig. 1-7d). This 3D case gave a closer look to simulate the indentation on the spinal cord in the vertebrae column.

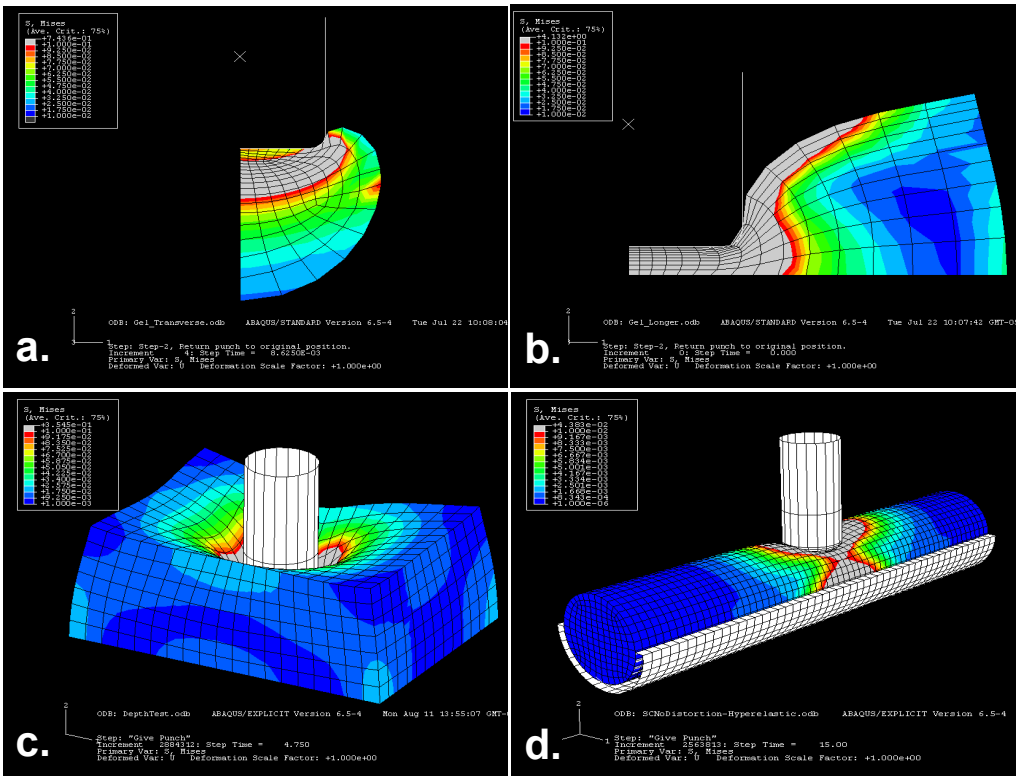

Figure 1-7. Progression of the indentation FEA modeling started from a (a) 2-D transverse case, (b) 2-D sagittal model, (c) 3-D cubic model, and (d) 3-D model of a tube

laying on top of an arc. These trials provided precious fundamentals and experience in developing a successful 3-D FEA SCI model.

With the experience of building FEA indentation models, we then moved to a more complex 3-D modeling which considered more realistic elements in contusion SCI. Base on the *in vivo* high resolution diffusion tensor images, this model was constructed adapting the realistic spinal cord geometries. The model consisted of the mouse spinal cord, with distinct element sets for the GM and WM, the CSF, the dura mater, a rigid spinal cord column and a rigid impactor [23, 25]. The dura, CSF and spinal cord were merged together, while maintaining distinct boundaries. The dura and CSF were partitioned along boundaries of the spinal cord. The dura mater was meshed with reduced integration hexahedral elements, one-element thick, and comprised 1410 nodes and 336 elements. The GM, WM, CSF was meshed with wedge elements, comprised 1530 nodes and 1840 elements. All parts had independent element sets with common nodes at the boundaries to maintain overall continuity with 1880 nodes and 2176 elements in total.

The spinal column is assumed to be a rigid body providing friction to the spinal cord. The coefficient of friction between spinal cord and spinal column was 0.6 and 0.15 between spinal cord and impactor tip. The impactor was placed in direct contact with the exposed dura and prescribed a 0.8 mm displacement penetrating into the spinal cord with the speed of 0.2 m/s. The boundary condition for the spinal column was encastred. The setup of our preliminary FEA model is shown in Fig. 1-8.

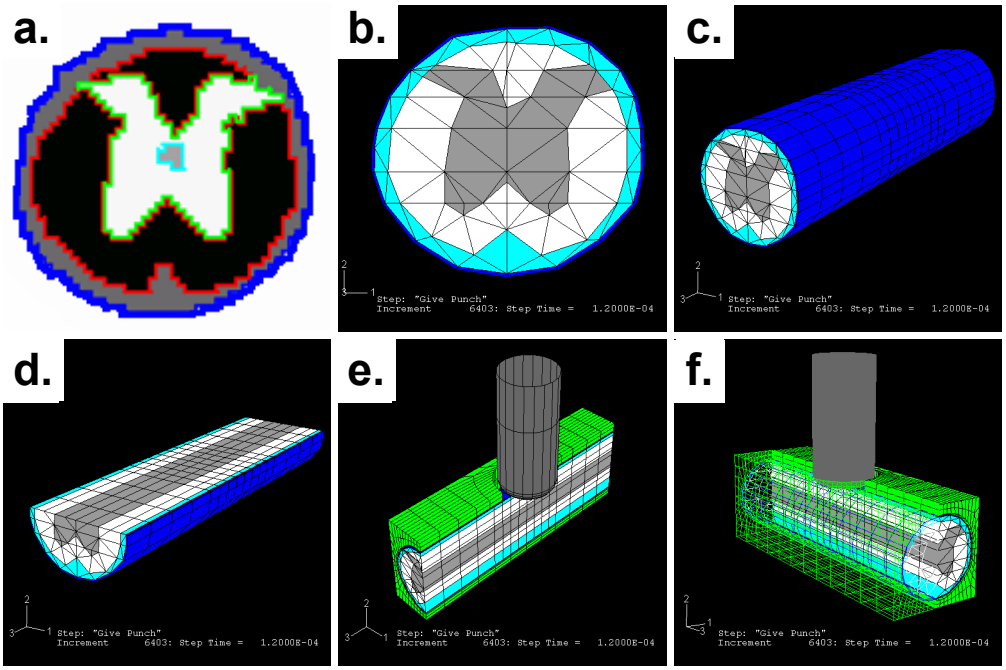

Figure 1-8. The component of the spinal cord was defined based on in vivo DTI maps of a control mouse undergone laminectomy (a): dura (blue), CSF (gray), WM (black), GM (white), and central canal (gray at center). The mesh was generated on the defined component and displayed in transverse (b), longitudinal (c), and horizontal (e) and sagittal (f) cutout views. The region of green represents the spinal column. A friction between spinal column and spinal cord was assigned. A hole was extruded to expose the spinal cord simulating the effect of laminectomy.

Impact tip trajectory was input by applying amplitude module as the moving tip of contusion SCI in Abaqus. The simulation successfully converges describing the process of impact. The resulting von Mises stress contour indicates that the stress concentrates at the impact epicenter. The representative results are shown in Fig. 1-9.

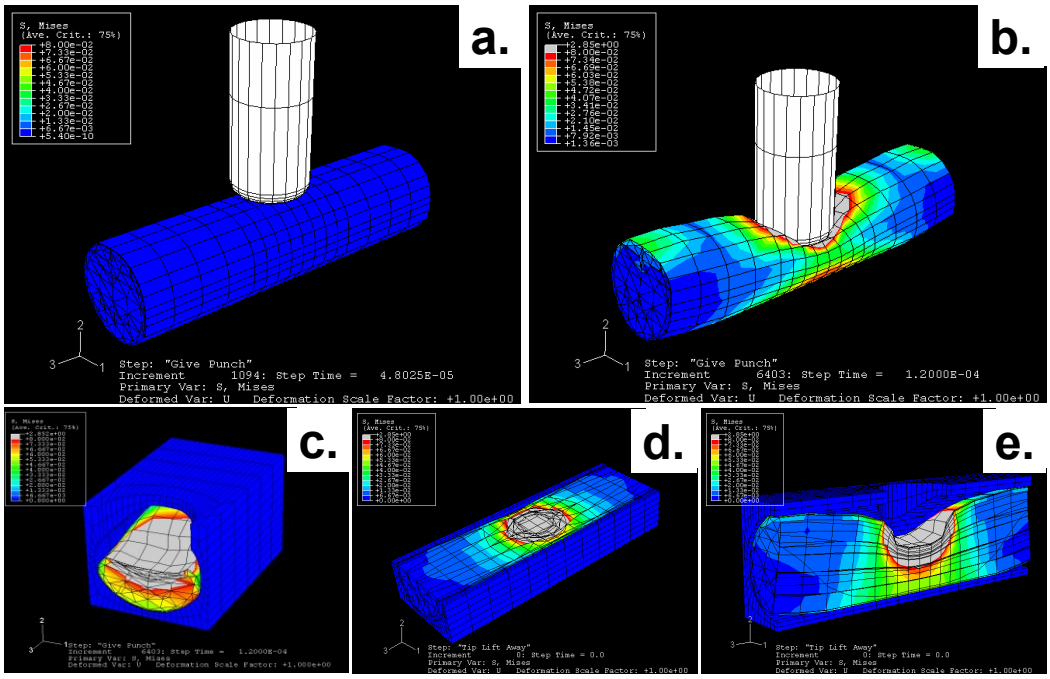

Figure 1-9. Isometric views of von Mises stress in the spinal cord: initial contact (a), at peak compression following simulation of a 0.2 m/s, 0.8 mm displacement impact experiment (b), transverse (c), coronal (d), and sagittal (e) views at the epicenter. The derived von Mises stress contour did not extend beyond the impact site elevating at the epicenter. Similar stress patterns were also seen in the recent published FEA study of rat [23].

1.4 Magnetic Resonance Imaging in SCI

1.4.1 MRI of Spine Anatomy and Function

Magnetic resonance imaging (MRI) is a noninvasive imaging method known to provide dynamic soft tissue contrast to visualize the underlying structure with exquisite details [43-48]. For example, physicians are able to differentiate SCI from musculoskeletal pain with the help of MRI [49]. MRI of the spine shows the anatomy of the vertebrae that make up the spine, as well as the disks, spinal cord and the spaces between the vertebrae through which nerves pass [50]. Furthermore, MRI is capable of

evaluating the extent of spinal cord compression and to stratify therapeutic interventions. Besides the clinical use for diagnosis of CNS diseases, functional assessments of SCI in animal models have also been reported [44, 45, 47]. The MR signal contribution from a specific tissue of interest may be emphasized by adjusting the MR parameters to dynamically change its contrast [51-53]. Multiple MR parameters, such as T1, T2, and diffusion weighted MRI (DWI) determined water apparent diffusion coefficient (ADC) and diffusion anisotropy, will change after tissue injury [54-58]. Among them, ADC is the most sensitive marker for early detection of tissue damage. For example, a decrease in ADC has been observed minutes after acute brain ischemia [59], correlating with ischemia induced cell edema.

1.4.2 Diffusion MRI Assessing Spinal Cord WM Injury

Diffusion MRI generates imaging contrast noninvasively based on measuring the random motion of water protons. The measured diffusion coefficient is anisotropic in the spinal cord WM. The diffusion anisotropy of WM tracts has been considered as reflective of its integrity. Diffusion MRI of the rodent SCI model has been previously described [58, 60-62]. Its ability to assess the extent of normal WM has been demonstrated to effectively evaluate the secondary injury and to predict the functional outcome in the rodent model of SCI [11]. It is ultimately the best way to assess the suitability of an injury model for FEA analysis of SCI in this dissertation.

1.4.3 Animal Preparation for *in vivo* DTI

In order to obtain high resolution diffusion MRI, as well as to avoid physiological rundown during long scans, a custom-made animal holder has been designed and built in our lab (Fig. 1-10). The animal is first anesthetized with an isoflurane and oxygen

mixture (5% for induction and 0.7-1.5% for maintenance). Core body temperature is maintained at 37°C with a circulating warm-water pad. The respiratory exhaust line is connected to a pressure transducer to synchronize DTI data collection with the animal's respiratory rate. An actively decoupled surface coil covering vertebral segments T6 - T12 (15 mm × 8 mm) was used as the RF receiver. A 9-cm i.d. actively decoupled Helmholtz coil was employed as the RF transmitter [32]. All experiments were conducted on a 4.7 T magnet (Oxford Instruments, Abingdon, UK) equipped with a 15-cm inner diameter, actively shielded Magnex gradient coil (60 G/cm, 270 μs rise time). The magnet, gradient coil, and IEC gradient power supply was interfaced with a Varian DirectDrive console (Varian, Inc., Palo Alto, CA) with a Linux operating system.

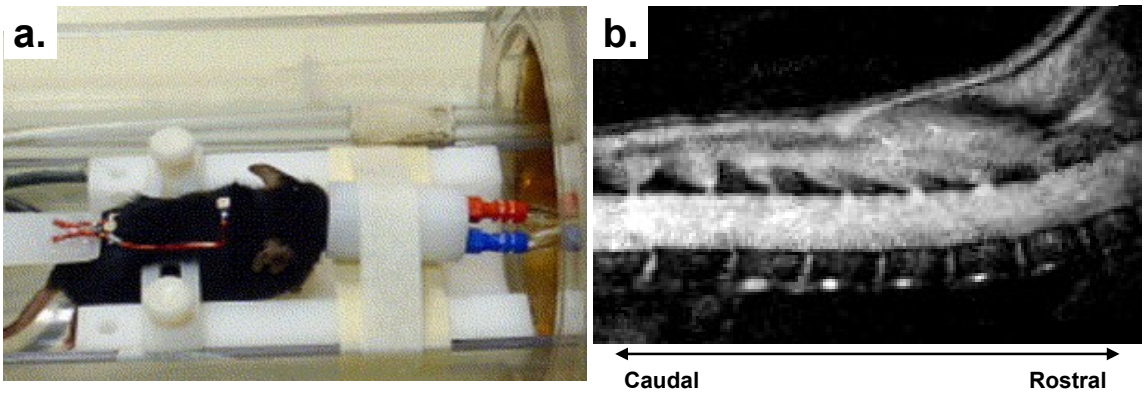

Figure 1-10. (a) Spinal cord restraining device and RF coil configuration for in vivo DTI. (b) Sagittal view of the T1/T2 weighted image of mouse spinal cord.

1.5 Dissertation Outline

This dissertation is consisted of 6 chapters. Chapter one gives an overview of the basic methodology involved in the proposed work. Chapter two describes the basic

principle of diffusion tensor MRI. Chapter three to five describe my research projects addressing three specific aims:

Aim 1: To improve the imaging efficiency of in vivo diffusion MRI allowing high resolution diffusion spinal cord imaging improving throughput.

Aim 2: To study the capability of using DTI injury biomarkers to evaluate the role of myelin sheath in functional recovery in SCI.

Aim 3: To correlate the contusion injury patterns of in vivo MRI with the biomechanical parameters generated using FEA to better understand the mechanism of concomitant distal vascular injury and proximal axonal injury in the acute SCI.

In chapter three, I describe a simplified two-direction diffusion weighted MRI to effectively derive axial and radial diffusivities without the need of full tensor. To further improve the temporal resolution to further increase the throughput, I implemented a multiple-echo spin echo diffusion weighting sequence in Varian scanners. Both were applied to the project in chapter five. In chapter four, in vivo DTI biomarkers were employed to investigate the role of myelin in functional recovery after contusion SCI with comprehensive immunohistochemistry validation. Chapter five combines in vivo DTI with the biomechanical simulation to investigate how the axon and vascular injuries relate to biomechanical parameters.

Chapter 2. The Principle of Diffusion MRI and Its Application on Spinal Cord Injury

2.1 The MRI Basics

Protons of tissue water are the most abundant nuclear spins measured by MRI [63]. A MR image is proton densities measured under spatial encodings at different orientations. One of the commonly used pulse sequences is spin echo (SE) sequence (Fig. 2-1). The signal intensity (S_0) may be expressed as:

$$S_0 = M_Z(1 - e^{-TR/T1})e^{-TE/T2} \quad (2\text{-}1)$$

, where M_z is longitudinal magnetization, TR is the repetition time, TE is the echo time, T1 is the spin-lattice relaxation time, and T2 is the spin-spin relaxation time.

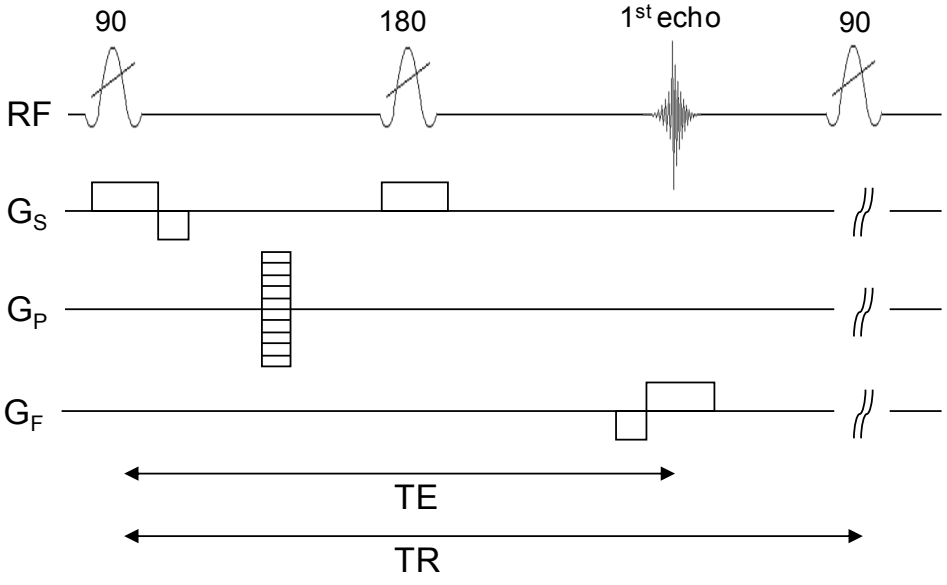

Figure 2-1. A schematic representation of spin echo pulse sequence. In this diagram, RF is the radio frequency pulse; a slice selective 90o pulse followed by an 180o refocusing

pulse. GS, GF, and GP are the slice selective, frequency encoding and phase encoding gradients, respectively. "Echo" represents the signal received from the slice of interest. A short TR and short TE will give a T1-weighted image, a long TR and short TE will give a proton density image, and a long TR and long TE will give a T2-weighted image.

The diffusion-weighted imaging is widely used as a noninvasive and sensitive imaging modality for early detection of CNS injury [33, 58, 64, 65]. Herein, the measurement of diffusion coefficient is briefly reviewed.

2.2 Measuring Diffusion Using MRI

Diffusion is a physical process that involves the translational movement of molecules via thermally driven random Brownian motion [66-68]. The mobility of the molecules can be characterized by the diffusion coefficient, *D*, which is related to the root mean square (RMS) displacement of the molecules over a given time. The contrast of diffusion MRI originates from the random microscopic motion of water protons (i.e., water diffusion). The widely used Stejskal-Tanner pulse sequence places two diffusion gradient pulses along the direction measuring diffusion on each side of the 180° refocusing pulse in the SE sequence (16, 29–31). In a diffusion measurement, the Larmor frequencies are made spatially dependent by applying a magnetic field gradient along one direction (Fig. 2-2).

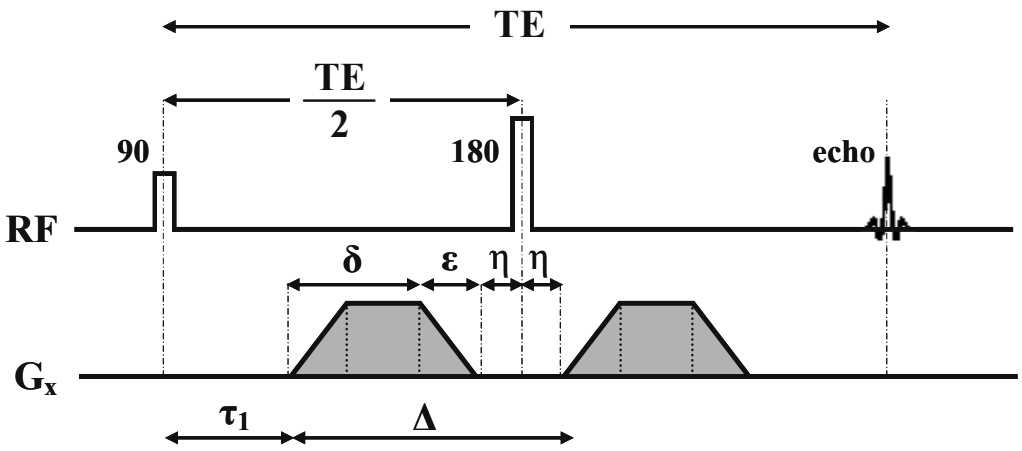

Figure 2-2. A schematic representation of the one-direction (x) Stejskal-Tanner diffusion pulse sequence. Diffusion gradients Gx are applied after 90° pulse and on both sides of the 180° pulse in x direction. The gradients shown in the figure are trapezoidal, where δ is the time between the onset of a trapezoidal pulse and the end of its plateau, ε is the rise time of the trapezoidal ramp, and Δ is the time between the onset of the first and second gradient pulses. The signal is read out as an echo sampled at TE.

When the gradient is applied in the x direction, the Larmor frequency varies with position in the x direction. An identical gradient is placed on each side of the 180° refocusing pulse, so spins that have not moved will realign at the echo time [69]. If spins diffuse randomly, their precession frequency after the refocusing pulse will be different from the frequency before the pulse, and they will not realign perfectly. The faster spins diffuse in the x direction during the spin echo period, the more signal intensity decreases. The amount of signal loss depends on the strength and duration of the magnetic field gradient (represented by the letter *b*) and on the diffusion coefficient of the spin (*D*). The signal intensity (*S*) of the diffusion weighted image in homogeneous, isotropic systems decreases exponentially as *b* increases.

$$S = S_0 e^{-bD} \tag{2-2}$$

, where S_0 is the signal intensity without diffusion-sensitizing gradients; includes contributions from proton density and *T2* relaxation. *D* is the diffusion coefficient, and *b* is the diffusion weighting factor. The *b*-value is determined by the strength and duration of the magnetic field gradient, and will be discussed in section 2.3. In biological systems, signal decay appears to be biexponential (34–37), but monoexponential decay is a reasonable model for *b* factors up to 2,500 s/mm^2. The *D* can be calculated by making measurements at a low *b* factor, b_1, and a higher *b* factor, b_2, with all other pulse sequence parameters identical.

$$S_1 = S_0 \exp(-b_1 D) \tag{2-3}$$

$$S_2 = S_0 \exp(-b_2 D) \tag{2-4}$$

$$S_1 / S_2 = \exp[(b_2 - b_1) D] \tag{2-5}$$

$$D = \ln(S_1 / S_2) / (b_2 - b_1) \tag{2-6}$$

2.3 Calculation of the *b* Factor with Gradient in One Dimension

If we consider a diffusion measurement in a static B_0 field, the diffusion-sensitizing gradient, $\vec{G}(t)$, is applied in a single direction. The spatially dependent phase shift, $\phi(t)$, of a spin over time *t* is:

$$\phi(t) = \gamma B_0 t + \gamma \int_0^t \vec{G}(t') \cdot \vec{r}(t') dt \tag{2-7}$$

where γ is the gyromagnetic ratio, and $\vec{r}(t)$ is the location of the nuclear spin [70]. The first term represents the phase accrual due to the static B_0 field, and the second term is due to the effect of a magnetic field gradient. The phase term of the second part is proportional to the strength of the field gradient, the duration of the gradient, and the spatial location of the spin. It is obvious that the magnetic field gradient can be used to locate a spin by means of the difference in the Larmor frequency. After the first diffusion weighting gradient (before 180° RF pulse), the accumulative phase shift $\phi(t_1)$:

$$\phi(t_1) = \gamma B_0 \cdot (TE/2) + \gamma \int_{\tau_1}^{\tau_1+\delta+\varepsilon} \vec{G}(t) \cdot \vec{r}(t)dt \tag{2-8}$$

After 180° RF pulse, the second diffusion weighted gradient $\vec{G}(t)$ will induce an inverse phase shift $\phi(t_2)$ of the proton spin:

$$\phi(t_2) = -[\gamma B_0 \cdot (TE/2) + \gamma \int_{\tau_1+\Delta}^{\tau_1+\Delta+\delta+\varepsilon} \vec{G}(t) \cdot \vec{r}(t)dt \,] \tag{2-9}$$

During the spin echo period (*TE*), the total phase shift resulting from the diffusion-sensitizing gradient,

$$\phi(TE) = \gamma \int_{\tau_1}^{\tau_1+\delta+\varepsilon} \vec{G}(t) \cdot \vec{r}(t)dt) - \gamma \int_{\tau_1+\Delta} G(t) \cdot \vec{r}(t)dt) \tag{2-10}$$

If protons move between the two diffusion-sensitizing applications, the second gradient cannot perfectly refocus the phases, which leads to signal loss. The displacement function $\vec{r}(t)$ is random and the phase shifts accumulated by individual spins differ causing the signal attenuation. The resultant MR signal is exponentially related to the

variance of a Gaussian phase distribution, $<\phi^2>$, which is equal to the product *bD* in equation (2-2). For the trapezoidal gradient scheme shown in Fig. 2-2 with finite ramping time:

$$b = \gamma^2 G^2 [\delta^2 (\Delta - \frac{\delta}{3}) + \frac{\varepsilon^2}{30} - \frac{\delta \varepsilon^2}{6}] \qquad (2\text{-}11)$$

The value of the measured diffusion coefficient is dependent on the diffusion weighting parameters, such as the diffusion gradient strength and timing, Δ and δ, as well as the direction of the applied gradients.

On account of the diffusion measurements along multiple directions, the accurate calculation of a ***b*** matrix for an imaging sequence requires the inclusion of all gradients including the static background, the imaging, and the diffusion weighting gradients. This makes the calculation of ***b*** matrix a complicated task. The imaging and background gradients have similar effects on the measurement. The following discussion refers both as imaging gradients.

2.4 Diffusion and Apparent Diffusion Coefficient

In an isotropic environment, such as pure water, diffusion coefficient of a molecule is the same in all directions. In an anisotropic environment, such as biological tissues, diffusion coefficient of a molecule is directionally dependent [64, 71, 72]. The underlying cellular microstructure of tissues complicates the situation and influences the measured diffusion coefficient of the diffusing molecules (e.g. intracellular, extracellular, neurons, glial cells, axons) within the tissue.

The diffusion coefficient measured by nuclear magnetic resonance (NMR) is best

known as the apparent diffusion coefficient (ADC). It takes into account that it is not a true measure of the 'intrinsic' diffusion, but rather that it depends on the interactions of the diffusing molecule within the cellular structures over a given diffusion time. By permitting enough time for the diffusing molecules to sample the local environment, the microstructural characteristics of the tissue can be inferred from the measured diffusion properties.

2.5 Diffusion Tensor Model and Diffusion Tensor Images

2.5.1 Diffusion Tensor Model

The ADC value measured using the Stejskal-Tanner diffusion sequence depends on the direction of the sensitizing gradient [71, 73, 74]. The anisotropic diffusion as seen in biological tissues is characterized by a second ranked tensor. It can be described by an axially symmetric 3×3 matrix with six unknown parameters. Thus, six independent diffusion weighting measurements with independent and non-collinear gradients would be necessary to derive the diffusion tensor and the anisotropic diffusion characteristic [70, 75, 76].

2.5.2 Calculation of *b* Matrix with Multiple Gradients

A tensor is not "a matrix" or an "array", but a tensor can be represented by a matrix of its components with respect to a reference coordinate. The gradient direction must be similarly specified by three orthogonal components [66, 70, 75]. Thus, the diffusion weighting factor is also typically described by a 3×3 ***b*** matrix. The orthogonal directions are usually taken to be the *x*, *y*, and *z* axes of the magnet's gradient system (laboratory frame in Cartesian coordinates). The 3D ***b*** matrix consists of six distinct terms: *bxx, byy, bzz, bxy, byx, bxz, bzx, byz, and bzy.* To calculate the signal intensity,

the exponent *bD* in Eq. (2-2) is replaced by the generalized dot product between the ***b*** matrix and the diffusion tensor ***D***:

$$\boldsymbol{b} = \begin{pmatrix} b_{xx} & b_{xy} & b_{xz} \\ b_{yx} & b_{yy} & b_{yz} \\ b_{zx} & b_{zy} & b_{zz} \end{pmatrix};\ \boldsymbol{D} = \begin{pmatrix} D_{xx} & D_{xy} & D_{xz} \\ D_{yx} & D_{yy} & D_{yz} \\ D_{zx} & D_{zy} & D_{zz} \end{pmatrix} \tag{2-12}$$

$$\boldsymbol{b} : \boldsymbol{D} = b_{xx}D_{xx} + b_{yy}D_{yy} + b_{zz}D_{zz} + 2b_{xy}D_{xy} + 2b_{xz}D_{xz} + 2b_{yz}D_{yz} \tag{2-13}$$

$$S = S_0 e^{-\mathbf{b}:\mathbf{D}} \tag{2-14}$$

, where ***b*** and ***D*** are matrices of the components in Cartesian coordinates. In the presence of multi-diffusion gradients and imaging gradients (i.e., background and imaging gradients), there are three gradient terms in the overall ***b*** matrix: $\mathbf{B}_d$ the diffusion gradients; $\mathbf{B}_i$ the imaging gradients; and $\mathbf{B}_{di}$ the cross-terms involving both diffusion gradients and imaging gradients. The $\mathbf{B}_d$ terms are the desired diffusion measurement terms. The $\mathbf{B}_i$ terms also appear in images of different *b* values, and therefore will be canceled in the ratio S_1/S_2.

2.5.3 DTI: Tensor Calculation

The diffusion tensor can be calculated from DWI data collected with diffusion-sensitizing gradients in six or more directions. For an experiment of total N diffusion measurements, M with $b > 0$ and N - M with $b = 0$. One approach is to represent the six distinct tensor elements and the logarithm of the $b = 0$ signal intensity as a seven-element column vector **α** [75]:

$$\boldsymbol{\alpha} = [D_{xx}, D_{yy}, D_{zz}, D_{xy}, D_{xz}, D_{yz}, \ln(S_0)]^T \tag{2-15}$$

, where S_0 is the signal intensity with $\boldsymbol{b}$ = 0. Each $\boldsymbol{b}$ matrix is represented by a six-element row vector $\boldsymbol{b}_i$:

$$\boldsymbol{b}_i = (b_{xxi}, b_{yyi}, b_{zzi}, 2b_{xyi}, 2b_{xzi}, 2b_{yzi}) \tag{2-16}$$

, the seven-element row vector $\boldsymbol{B}_i$:

$$\boldsymbol{B}_i = (-b_{xxi}, -b_{yyi}, -b_{zzi}, -2b_{xyi}, -2b_{xzi}, -2b_{yzi}, 1) \tag{2-17}$$

These row vectors are combined into one large $N \times 7$ $\boldsymbol{B}$ matrix:

$$\boldsymbol{B} = \begin{pmatrix} -b_{xx1} & -b_{yy1} & -b_{zz1} & -2b_{xy1} & -2b_{xz1} & -2b_{yz1} & 1 \\ \vdots & \vdots & \vdots & \vdots & \vdots & \vdots & \vdots \\ -b_{xxN} & -b_{xxN} & -b_{xxN} & -b_{xxN} & -b_{xxN} & -b_{xxN} & 1 \end{pmatrix} \tag{2-18}$$

In the absence of noise, logarithms of the predicted signal intensities are given by an N × 7 column vectors:

$$\xi_i = \boldsymbol{B}_i \alpha = \ln(S_i) = \ln(S_0) - \boldsymbol{b}_i : \boldsymbol{D} \tag{2-19}$$

$$\xi = \boldsymbol{B}\boldsymbol{\alpha} = \begin{pmatrix} -b_{xx1}D_{xx} - b_{yy1}D_{yy} - b_{zz1}D_{zz} - 2b_{xy1}D_{xy} - 2b_{xz1}D_{xz} - 2b_{yz1}D_{yz} + \ln(S_0) \\ \vdots \\ -b_{xxN}D_{xx} - b_{yyN}D_{yy} - b_{zzN}D_{zz} - 2b_{xyN}D_{xy} - 2b_{xzN}D_{xz} - 2b_{yzN}D_{yz} + \ln(S_0) \end{pmatrix} \tag{2-20}$$

The $\boldsymbol{B}$ matrix has a row for each measurement, both b = 0 and b > 0, and the $\boldsymbol{\xi}$ vector contains an element for each measurement. The noisy observed data are represented as an N×1 column vector $\boldsymbol{x}$:

$$\boldsymbol{x} = \begin{pmatrix} \ln(S_1) \\ \ln(S_2) \\ \vdots \\ \ln(S_N) \end{pmatrix} \tag{2-21}$$

The noisy data for each acquisition can then be expressed as:

$$\boldsymbol{x} = \boldsymbol{B}\alpha + \boldsymbol{\eta} = \boldsymbol{\xi} + \boldsymbol{\eta} \tag{2-22}$$

, where **η** is a noise vector.

2.5.4 Measurement of Anisotropy

The diffusion tensor in laboratory frame, ***D***, can be transformed into a local frame by diagonalization to derive eigenvectors and eigenvalues:

$$\boldsymbol{D} = \begin{bmatrix} v_1 & v_2 & v_3 \end{bmatrix} \begin{pmatrix} \lambda_1 & 0 & 0 \\ 0 & \lambda_2 & 0 \\ 0 & 0 & \lambda_3 \end{pmatrix} \begin{bmatrix} v_1 \\ v_2 \\ v_3 \end{bmatrix} = v\Lambda v^T \tag{2-23}$$

, where ***v*** is the principal directions (ν_1, ν_2, ν_3) and ***Λ*** can be used to represent the magnitudes of diffusivities ($\lambda_1, \lambda_2, \lambda_3$) along the principal directions.

Many applications require a metric to assess diffusion anisotropy. Thus, a scalar of “diffusion anisotropy index” or DAI indicates the degree of anisotropy has been adopted to quantitatively evaluate WM integrity. Various forms of DAI have been employed. The most widely used is fractional anisotropy (FA), defined as the standard deviation of the three eigenvalues normalized to the tensor magnitude, Eq. [2-25]. The

relative anisotropy (RA), standard deviation of eigenvalues normalized to ADC, Eq. [2-26], has also been used in the literature [70, 77].

$$FA = \sqrt{\frac{3[(\lambda_1 - < D >)^2 + (\lambda_2 - < D >)^2 + (\lambda_3 - < D >)^2]}{2(\lambda_1^2 + \lambda_2^2 + \lambda_3^2)}} \quad (2\text{-}24)$$

, where $< D >= (\lambda_1 + \lambda_2 + \lambda_3)/3$, is mean ADC. FA ranges from 0 (isotropic) to 1 (anisotropic).

$$RA = \sqrt{\frac{[(\lambda_1 - < D >)^2 + (\lambda_2 - < D >)^2 + (\lambda_3 - < D >)^2]}{\sqrt{3} < D >}} \quad (2\text{-}25)$$

, where RA ranges from 0 (isotropic) to $\sqrt{2}$ (anisotropic).

2.6 Beyond Apparent Diffusion Coefficient

2.6.1 ADC and CNS WM Injury

Water diffusion is sensitive to the underlying tissue microstructure providing a unique measure to assess the CNS tissue integrity. For example, the reduction in the ADC has been observed within minutes after the onset of cerebral ischemia [78], reflecting the underlying cytotoxic edema (cellular swelling). Since the conventional MRI parameters such as T1, T2 and proton density change relatively little at the acute phase of stroke, the decreased ADC has been widely employed to identify cerebral infarction in stroke patients [78]. The increased ADC has also been observed in WM lesions of multiple sclerosis (MS) patients [70, 79].

Characterization of the relation between MR diffusion measurements derived apparent diffusion coefficient and anisotropy (i.e. directional dependence) and the

underlying microstructure of CNS tissues has been a hotly pursued research area. Several biophysical mechanisms have been considered as the cause of anisotropic diffusion and its potential utility in the nervous system. However, a unified theory of connecting diffusion anisotropy and underlying tissue pathology has not been established [71].

2.6.2 DTI in Rodent SCI

For the application of DTI to detect pathophysiology, axial diffusivity ($\lambda_{||}$) and radial diffusivity ($\lambda_{\perp}$) derived using DTI have been used to assess the axonal and myelin damage in contusion SCI [32, 33, 58, 73, 74, 80-86]. They are defined as:

$$\lambda_{||} = \lambda_1 \tag{2-26}$$

$$\lambda_{\perp} = \frac{\lambda_2 + \lambda_3}{2}, \tag{2-27}$$

where λ_1 is the principal eigenvalue and λ_2, λ_3 are the second and third eigenvalue of the diffusion tensor.

In VLWM region, a decreased $\lambda_{||}$ in the hyper-acute phase and an increased $\lambda_{\perp}$ in the chronic phase have been reported in the rodent contusion SCI. In this dissertation, the correlations of DTI biomarkers, biological outcome and underlying injury mechanism of contusion SCI is investigated.

Immediately after contusion SCI, the GM to WM contrast was lost in $\lambda_{||}$ maps at the impact epicenter (Fig. 2-3). The decreased $\lambda_{||}$ reflects axonal damage in VLWM revealing temporal and spatial progression of the injury [32, 33, 58, 80].

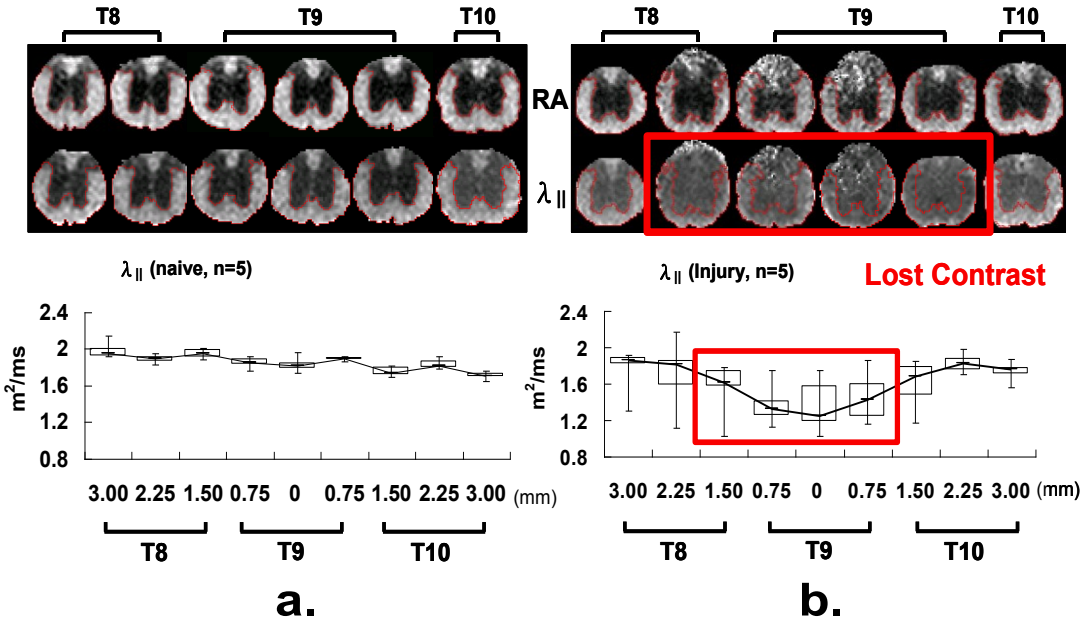

Figure 2-3. RA and $\lambda_{||}$ maps of (a) naïve and (b) injured mouse spinal cords at hyperacute phase. RA maps provide good contrast between GM and WM to distinguish the region of VLWM in control mice. GM-WM tissue contrast loss was observed in four slices of $\lambda_{||}$ map after injury (marked in red box), due to significantly decreased $\lambda_{||}$ (lower panel).

Axonal injury is evidenced by the decreased $\lambda_{||}$ and microscopic findings in yellow fluorescent protein (YFP) mice. Swelling, beading, and fragmentation of YFP+ axons were observed in the injured cords, consistent with the decreased $\lambda_{||}$ (Fig. 2-4). Our findings suggest that $\lambda_{||}$ is a sensitive to axonal injury in the mouse model of contusion SCI allowing determination of the residual VLWM in the acute phase (Fig. 2-5).

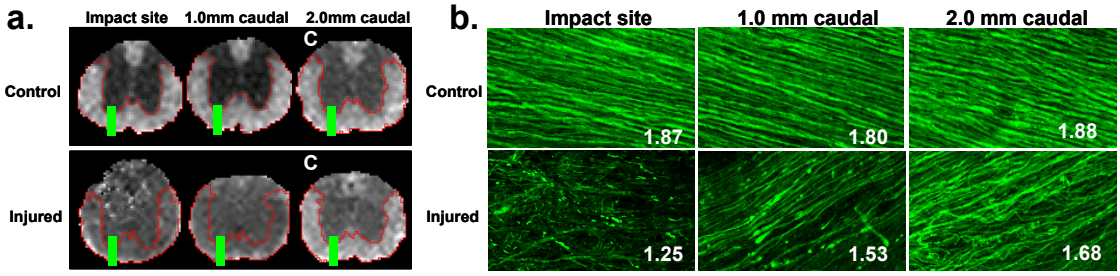

Figure 2-4. Correlation between (a) $\lambda_{||}$ and (b) YFP axon integrity. After contusion SCI at T9 vertebral level, acute $\lambda_{||}$ maps suggest spatially dependent axon disintegration as evidenced by the decreased $\lambda_{||}$. Confocal microscopic images taken from the region marked in $\lambda_{||}$ maps clearly demonstrate the correlation between axonal integrity and $\lambda_{||}$ (numbers in b) where comparable $\lambda_{||}$ were seen in control cords. In contrast, at the injured cord, axons appear incoherently aligned with fragmented cytoskeletons. The extent of $\lambda_{||}$ decrease correlated with the extent of axonal swelling, beading, and cytoskeletal fragmentation.

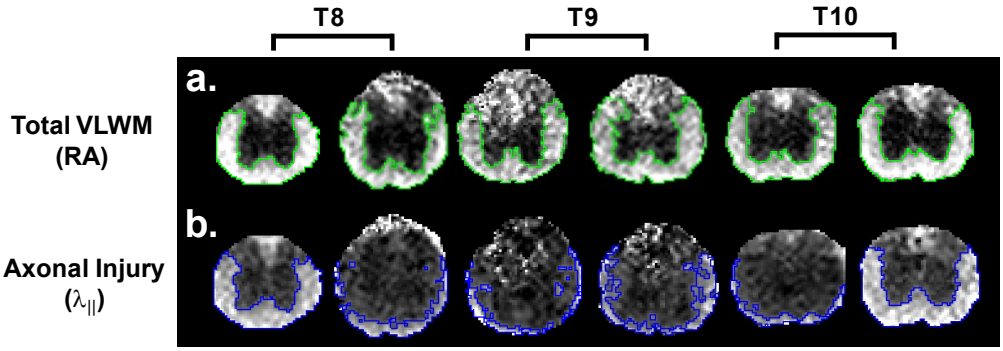

Figure 2-5. Properties of anisotropy (a) and $\lambda_{||}$ (b) in the acute SCI have potential to identify the regions of total WM and the axonal injury immediately after injury. The RA is mostly preserved in VLWM due to the unchanged $\lambda_{\perp}$, however, the $\lambda_{||}$ is sensitive to reflect the axonal integrity in the acute SCI.

2.6.3 Determination of Residual VLWM in Sub-Acute Phase

Except using $\lambda_{||}$ to determine the axonal integrity in the acute phase, we also demonstrated that RA could be used to reflect the integrity of the residual myelinated axons in the sub-acute phase. The RA determined residual VLWM in sub-acute phase is

able to correlate with the chronic neurological outcomes assessed by the hind limb function.

RA maps at acute (~3 hrs) and sub-acute (7 days) phases show the clear evolution after SCI (Fig. 2-6a) [33, 58]. After the segmentation of the residual VLWM, spatial volumes of residual WM for acute, sub- acute injury cord and control cord were calculated and normalized by control cord (Fig. 2-6b) to take into account of the effect of atrophy of the injured cords. The residual VLWM was determined by applying threshold of mean ± 2×SD of RA from control VLWM.

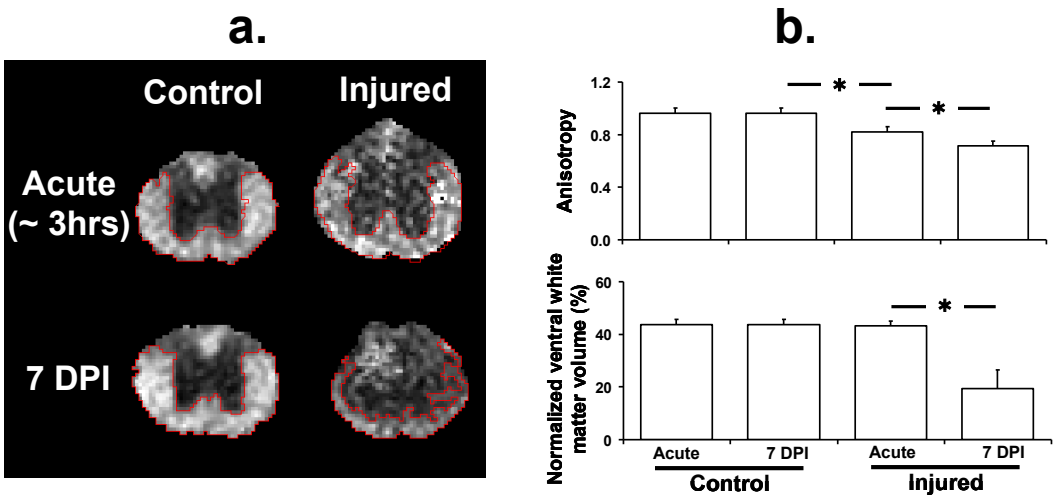

Figure 2-6. The quantified RA of injured cord 7 DPI showed statistically significant 15 % decrease from the controls. (a) The RA map from the injured cord 7 DPI showed significant residual VLWM volume reduction. (b) Acutely, the preservation of RA in the injured cords results in no difference in residual WM compared to the control.

We further examined the acute and sub-acute residual VLWM extent for the prediction of animal's long-term behavioral outcomes (Fig. 2-7). At the acute phase, anisotropy is largely preserved in the VLWM resulting in overestimating residual VLWM volume for accurate assessment of its correlation with animal's long term behavior.

However, at the sub-acute phase (7 DPI), we observed an excellent correlation between residual VLWM and the chronic (21 DPI) BMS score. Our results suggest that the anisotropy map derived from DTI measurements has potential to predict the long-term behavioral outcomes by accurately estimating the extent of the residual VLWM sub-acutely (7-DPI) but not at the hyper-acute phase (less than a few hours).

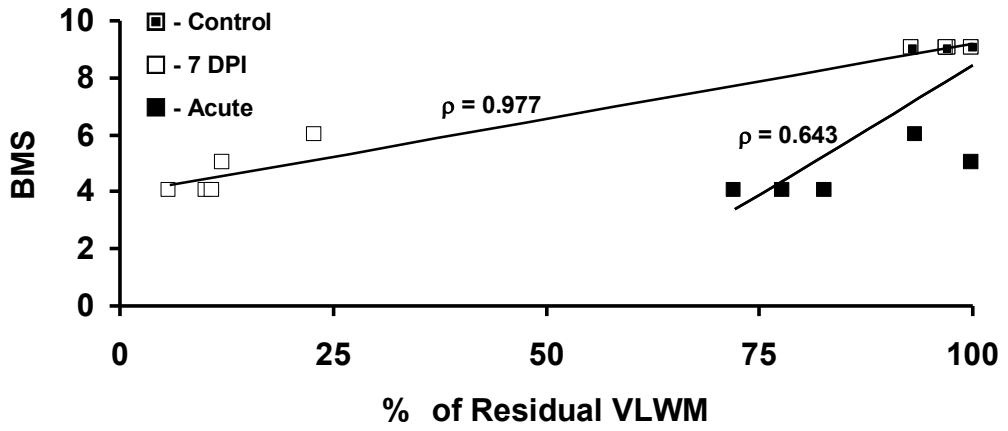

Figure 2-7. The normalized residual VLWM of acute (~3 hrs) and sub-acute (7 DPI) injury cord, including control, are shown with chronic phase (21 DPI) BMS. The correlation of residual VLWM to BMS is shown for between acute and control and between sub-acute (7 DPI) and control.

Chapter 3. Improving Image Quality of Mouse Spinal Cord Diffusion MRI

This Chapter represents a modified version of a manuscript initially published in *Journal of Neurotrauma*. (Tu TW, Kim JH, Wang J, Song SK, "Full tensor diffusion imaging is not required to assess the white matter integrity in mouse contusion spinal cord injury." *Journal of Neurotrauma* 2010 Jan; 27(1):253-62.)

3.1 To Accelerate Scan: Assessing VLWM Integrity in Contusion SCI with Two-Directional DWIs

Abstract

In vivo DTI derived indices have been demonstrated to accurately quantify WM injury after contusion SCI in rodents. In general, a full diffusion tensor requires the acquisition of diffusion weighted images (DWI) along at least six independent directions of diffusion sensitizing gradients. Thus, DTI measurements of rodent central nervous system are time consuming. In this study, diffusion indices derived using the two-direction DWI (parallel and perpendicular to axonal tracts) were compared with those obtained using six-direction DTI in a mouse model of SCI. It was hypothesized that the mouse spinal cord VLWM tracts, T8 – 10 in this study, aligned with the main magnet axis (z) allowing the apparent diffusion coefficient parallel and perpendicular to the axis of the spine to be derived with diffusion weighting gradients in the z and y axes of the magnet coordinate respectively. Compared with six-direction full tensor DTI, two-direction DWI provided comparable diffusion indices in mouse spinal cords. The measured extent of spared VLWM after injury estimated by anisotropy indices, using both six-direction DTI and two-direction DWI were in close agreement and correlated well with histological

staining and behavior assessment. The results suggest that the two-direction DWI derived indices may be used, with significantly reduced imaging time, to accurately estimate spared VLWM in mouse SCI.

3.1.1 Introduction

SCI results in devastating functional disabilities in patients. Due to the interference of spinal shock with functional assessment of SCI patients in the clinical setting, it is important to develop a noninvasive imaging technique for acute evaluation of spinal cord integrity after injury. Diffusion tensor imaging (DTI) has been applied in rodent models of SCI to assess the spinal cord VLWM tract integrity [33, 35, 58, 61, 62, 87-91]. The extent of spared VLWM may be estimated noninvasively using the DTI derived directional diffusivity, i.e. axial ($\lambda_{\parallel}$) and radial diffusivity ($\lambda_{\perp}$), following injury [33, 35, 88].

Multiple directions of diffusion weighting gradients are needed to accurately reflect WM structure in the human brain. The optimal number and orientations of unique gradients in estimating the diffusion tensor quantities has been extensively researched [92-94]. In general, when time is limited, at least six diffusion weighted images (DWI) are required to derive the diffusion tensor. The WM structure of spine is less complicated than that of the brain. Thus, it would be possible in the spine to choose a simpler sampling scheme, to minimize the scan time, while still obtaining adequate information to indentify WM structure [87, 90, 95, 96].

Several *ex vivo* studies have characterized SCI by correlating apparent diffusion coefficient (ADC) values with the degree of injury [88, 89, 91, 95]. Ford et al. [91] measured diffusion coefficients along the longitudinal (z) and transverse (y) axes. They found significant decreases in longitudinal ADC value and increases in transverse ADC

value at 7 days after injury. Based on the assumption of cylindrical symmetry of the excised spinal cord, Gulani et al. [95] showed that four of the six unique elements (D_{zz}, D_{xx}, D_{yy}, D_{xy}) in the diffusion tensor were sufficient to study the spinal cord. Nevo et al. [88] and Schwartz et al. [89] used two orthogonal diffusion gradient directions ($ADC_{||}$ and $ADC_{\perp}$) to demonstrate that the resulting diffusion anisotropy index (AI) was a simple and scalable parameter that documented the tissue degeneration and treatment effect after injury. *Ex vivo* samples offer the advantage of avoiding physiological noise allowing a more controlled data acquisition. However, fixed tissues suffer from complications including anatomic distortion resulting from fixation and the significantly reduced ADC values [90, 97].

Fraidakis et al. [61] used longitudinal (ADC_z) and transverse (ADC_x or ADC_y) diffusion gradients to assess the integrity of the rat spinal cord after injury *in vivo*. Significantly decreased longitudinal ADC_z and increased transverse ADC_x were observed. A quotient $Q_{z/x}$ (= ADC_z/ADC_x) was proposed as a marker reflecting the severity of WM tract degeneration. Clark et al. [96] showed that for a cylindrically symmetric spinal cord, appropriately oriented in the imaging gradient axes, it is possible to estimate the principal diffusivities and rotationally invariant measures by using a pair of diffusion-weighted scans. Gullapalli et al. [98] reported that the principal diffusivities of diffusion tensors reflect morphologic differences between WM tracts that are not well appreciated with either the trace (Tr) or the fractional anisotropy (FA). However, to the best of our knowledge, no studies to date have systematically compared measurements between simplified gradient-encoding schemes, such as two- or four-direction DWI, and the full tensor DTI scheme with appropriate validation using, the “gold-standard,” histology.

In the present study, the two-direction DWI and six-direction DTI measurements were employed to evaluate the extent of spared VLWM in mice after SCI. Results were correlated with histologicallly determined spared VLWM (Laxol Fast Blue, LFB) and open field tests of hindlimb locomotor function, evaluated using the BMS [31].

3.1.2 Materials and Methods

Spinal Cord Injury and Behavioral Assessment

All surgical preparations and pre- and post-surgical care were provided in accordance with Public Health Service Policy on Humane Care and Use of Laboratory Animals and Guide for the Care and Use of Laboratory Animals (Institute of Laboratory Animal Resources, National Research Council, 1996), and with the approval of the Washington University Animal Studies Committee.

Twelve 10 - 12 weeks old female C57BL/6 mice, weighing 18 - 22 g (Harlan Inc., Indianapolis, IN), were anesthetized with an isoflurane/oxygen mixture. Seven mice received mild contusion SCI utilizing a modified Ohio State University (OSU) impactor after dorsal laminectomy at the T9 vertebral level. The remaining five mice underwent a laminectomy without contusion and served as the control. The surgical site was closed in layers with 4-0 vicryl and nylon sutures. Injections of enrofloxacin (2.5 mg/kg) and lactated ringers (1.5 ml) were given subcutaneously. Manual bladder expression in injured mice was performed twice daily throughout the duration of the study [9]. Softened rodent chow was provided. Body weights were measured and compared with preoperative weight daily. High caloric nutrient paste (Nutrical; Evsco, Inc., Buena, NJ) was given to the mice to maintain body weights at 90% of preoperative values. All mice that received impact injuries exhibited partial paralysis with some spontaneous hindlimb

movements. In contrast, the sham-operated animals exhibited essentially normal over-ground locomotion. All injured mice were evaluated by BMS scores daily from 1 to 14 days after injury.

Animal Preparation for in vivo Diffusion MRI

Mice were anesthetized with an isoflurane/oxygen mixture (4.5 - 5% isoflurane for induction and 0.7 - 1.5% isoflurane for maintenance). Core body temperatures were maintained at 37°C with a circulating warm-water pad. The inhalant anesthetic was delivered to the mice through a custom-made nose cone. The respiratory exhaust line was connected to a pressure transducer to synchronize DTI data collection with the animal's respiratory rate [32].

An MRI-compatible device was utilized to stabilize the vertebral column as reported previously [32]. An inductively coupled surface receiver coil covering vertebral segments T6 - T12 (15 mm × 8 mm) was used as the receiver. A 9 cm (inner diameter) Helmholtz coil was employed as the RF transmitter. The alignment of spine segments to the magnet z-axis was carefully adjusted and confirmed by scout images. The entire preparation was placed in a 4.7 T magnet (Oxford Instruments plc, Abingdon, UK) equipped with a 15 cm (inner diameter), actively shielded Magnex gradient coil (60 G/cm, 270 μs rise time). The magnet, gradient coil, and IEC gradient power supply was interfaced with a Varian DirectDrive console (Varian, Inc., Palo Alto, CA).

in vivo Diffusion Tensor Imaging

In vivo diffusion measurements were conducted at 14 days after injury for comparing injury severities among animals after stable functional recovery was reached. A spin-echo sequence, modified by adding Stejskal-Tanner diffusion-weighting gradient

[99], was used. Diffusion weighted images for both six- and two-direction diffusion measurements were performed in an interleaved fashion. The following parameters were used for all measurements: spin echo time (TE) = 38 ms, time between the application of gradient pulses (∆) = 21 ms, diffusion gradient on time (δ) = 7 ms, diffusion gradient amplitude = 12.5 G/cm, number of averages = 8, field of view (FOV) = 1 x 1 cm, and data matrix = 128 x 128 (zero-filled to 256 x 256). The repetition time (TR ≈ 1.2 s) was varied according to the period of the respiratory cycle (~270 ms). A single line of k-space from each of three different image slices was collected with every breath.. Two diffusion-sensitizing, *b* values of 0 and 1.02 ms/μm^2, were used. Nine transverse images (slice thickness = 0.75 mm) were collected covering vertebral segments T8 - T10.

Six diffusion sensitizing gradients were employed, corresponding to the 12 cube edges, for DTI analysis: (Gx,Gy,Gz) = (1,1,0), (1,0,1), (0,1,1), (-1,1,0), (0,-1,1), (1,0,-1). Three eigenvalues (λ_1, λ_2, λ_3) were calculated from the diffusion tensor matrix. Mean diffusivity (<D>) was calculated by <D> = ($\lambda_1+\lambda_2+\lambda_3$)/3. Axial diffusivity was defined as $\lambda_{||} = \lambda_1$. Radial diffusivity was defined as $\lambda_\perp = (\lambda_2+\lambda_3)/2$. The scaled relative anisotropy (Asd) was calculated as:

$$Asd = \frac{\sqrt{(\lambda_1 - < D >)^2 + (\lambda_2 - < D >)^2 + (\lambda_3 - < D >)^2}}{\sqrt{2}(\sqrt{3} < D >)} \quad (3\text{-}1)$$

Asd ranges from 0 to 1, for direct comparison with the anisotropy index (AI), were derived using the two-direction scheme [100].

Two diffusion sensitizing gradients were employed for the two-direction DWI: (G_x,G_y,G_z) = (1,1,0), and (0,0,1). Apparent diffusion coefficient parallel ($D_{||}$) and perpendicular ($D_\perp$) to axonal tracts as well as the AI were directly obtained from the

relationship of signal intensity ($S_n(b)$) to the b value given by equations (3-2) and (3-3) (independent of tensor analysis).

$$S_n(b) = S_0 \cdot e^{-b \cdot D} \tag{3-2}$$

$$D = \frac{\ln\left[S_0(b) / S_n(b)\right]}{b} \tag{3-3}$$

The AI was derived according to Eq. (3-4)

$$AI = \frac{D_{||} - D_{\perp}}{D_{||} + D_{\perp}} \tag{3-4}$$

All parameters were derived from diffusion-weighted images using software written in Matlab (MathWorks, Natick, MA, USA). Three slices were averaged to obtain the value of each vertebral segment. The acquisition time was approximately 3.0 hrs for the six-direction DTI and 1.3 hrs for the two-direction DWI.

Region of Interest Analyses

The boundary between VLWM and ventral gray matter (VGM) was identified on Asd and AI maps. Regions of interest (ROIs) encompassing the total VLWM were manually delineated for VLWM (control and injured cords) and VGM (control cords only) on anisotropy maps. The anisotropy distributions of both VGM and VLWM were obtained from five sham-operated control animals for a histogram analysis of Asd and AI respectively. The mean and standard deviation (SD) were determined and a threshold (mean ± 2 × SD) was used to define the spared VLWM in contusion injured cords on both Asd and AI maps (designated by ROI_{Asd} and ROI_{AI}) (Fig. 3-1). Spared VLWMs of injured cords were then normalized to the total VLWMs of control cords to remove the

atrophic effect of the injured cord for the comparison with the gold-standard histology defined spared VLWM extent.

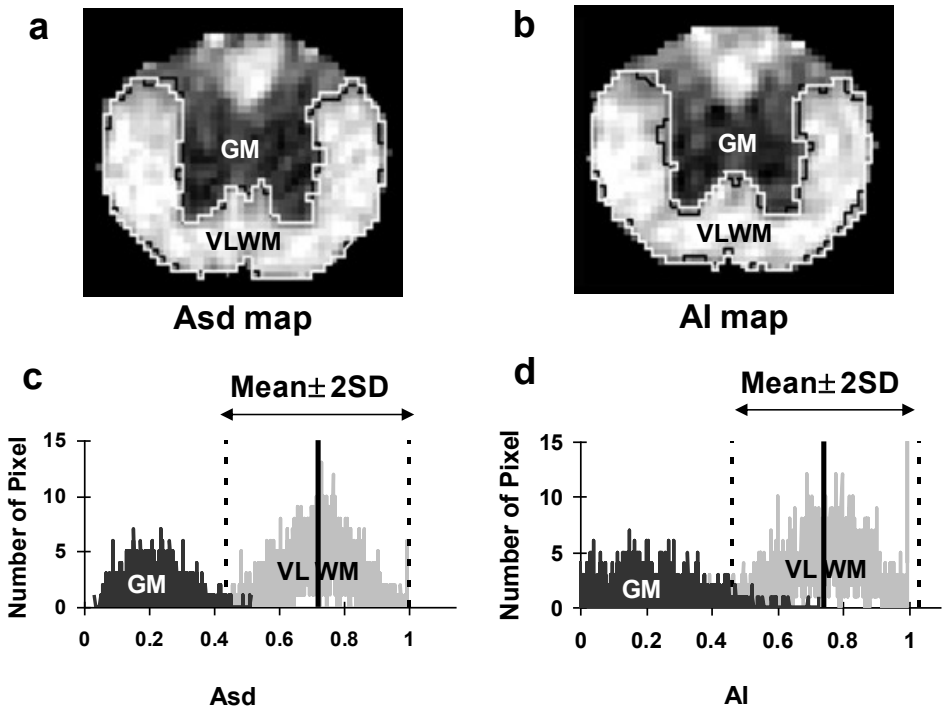

Figure 3-1. The manual (black) and threshold (white) segmentation of normal appearing VLWM in Asd (a) and AI (b) maps of a control cord. Two normal distributions of the pixel numbers of anisotropy were observed in manually defined VGM and VLWM in Asd (c) and AI (d) map. The mean ± 2×SD (95.4% confidence interval) of VLWM was used as threshold to define the region of normal appearing VLWM in the control and injured spinal cords, designated as ROIAsd and ROIAI.

Overlap Index of ROIs

To show that two- and six-direction diffusion measurements were detecting the same region of spared VLWM, an overlap index comparing ROI_{Asd} and ROI_{AI} was calculated to quantify the degree of overlap by:

$$Overlap\ Index = \frac{[(ROI_{Asd} \cap ROI_{AI}) / ROI_{Asd}] + [(ROI_{Asd} \cap ROI_{AI}) / ROI_{AI}]}{2} \quad (3\text{-}5)$$

,where $ROI_{Asd} \cap ROI_{AI}$ are the overlapping pixels. The formula estimates the mean overlap index for the partitions in ROI_{Asd} and ROI_{AI}. Kung et al. [101] performed a Monte Carlo simulation suggesting that this formula is less sensitive to the variation of ROI sizes (i.e. best suited for comparing different-sized ROIs). The index ranges from 0% (completely mismatching) to 100% (completely overlapping).

Behavioral Assessment of Hindlimb Locomotor Function

Animals were scored using BMS over the 14-day recovery period [31]. The test is taken by two or more evaluators for a scoring system from 1 (worst) to 9 (best), plus a subscore tally from 0 (worst) to 11 (best). Mouse hindlimb locomotor function is scored by angle movement, plantar placement, stepping, coordination, paw position, trunk instability, and tail position. In this study, the mild contusion SCIs resulted in BMS scores ranging from 6 to 9 on the injured mice and 9 on the laminectomy controls at 14 days after injury.

Tissue Preparation and Histological Analysis

Immediately after imaging, mice were perfusion fixed under deep anesthesia with 50 mL of 0.1 M phosphate-buffered saline (PBS) (pH 7.4) followed by 200 mL of 0.1 M PBS containing 4% paraformaldehyde (pH 7.4). Following fixation, the spine was excised, left in the fixative overnight, decalcified for 48 hrs, embedded in paraffin, and sectioned on a sliding microtome (5 μm) with the decalcified vertebral column intact. For the examination of the extent of spared VLWM, LFB (Sigma, Saint Louis, MO) staining was conducted. After deparaffinization, rehydration, and immersion in 1% LFB in 95%

ethanol and 0.5% acetic acid, the excess stain was rinsed off and differentiated using 0.05% $LiCO_3$ solution (56°C). Tissue was then mounted for microscopic inspection after completion of differentiation.

Stained sections at the injury epicenter were digitally imaged using a Nikon Eclipse 80i microscope equipped with a 4× objective, and the images were captured with a Photometrics CCD digital camera using MetaMorph image acquisition software (Universal Imaging Corporation, Downington, PA). All images were captured within 1 week following completion of histological staining. The area of positive staining was quantified by the pixel grayscale value threshold of 95.4% of the intensity from the intact nerve root. Spared VLWM area was then normalized to the total VLWM area. All images were calculated using NIH ImageJ v1.37 (Rasband, 1997-2005). All slides were assessed blindly with respect to the injury.

Statistical Analysis

Statistical analysis was performed with SAS version 9.1.3 (SAS Institute Inc., Cary, NC). Data were expressed as mean and standard deviation (SD). Paired student's t-test were performed comparing two- and six-direction diffusion measurements with $p < 0.05$ regarded as statistically significant. Correlations between normalized normal appearing VLWM areas determined by AI, and Asd were examined with Pearson correlation using 7 injured animals, each with 9 slices. The images correlated with LFB and BMS were obtained from one slice at the injury epicenter. Correlation coefficient (*r*) with *p*-value is reported.

3.1.3 Results

Diffusion index maps, acquired from both DTI and DWI at 14 days after injury, provide similar tissue contrast in the control cords (Fig. 3-2). WM appeared bright in both Asd and AI maps. The less anisotropic gray matter appeared dark. In both maps, the distinct border between GM and WM enabled manual segmentation of dorsal WM (DWM), GM, and VLWM. Furthermore, the cerebrospinal fluid (CSF) is hyperintense in both $\lambda_{\perp}$ and $D_{\perp}$ maps facilitating segmentation of the parenchyma of the cord. Unlike the more complete diffusion information provided in the full tensor image, the two-direction DWI scheme only measured the diffusion perpendicular and parallel to the spinal cord tract. The alignment of the spinal cord to the magnet z-axis was reaffirmed by the consistency between the directions of principal diffusion in DTI (Fig. 3-2g) and the magnet z-axis.

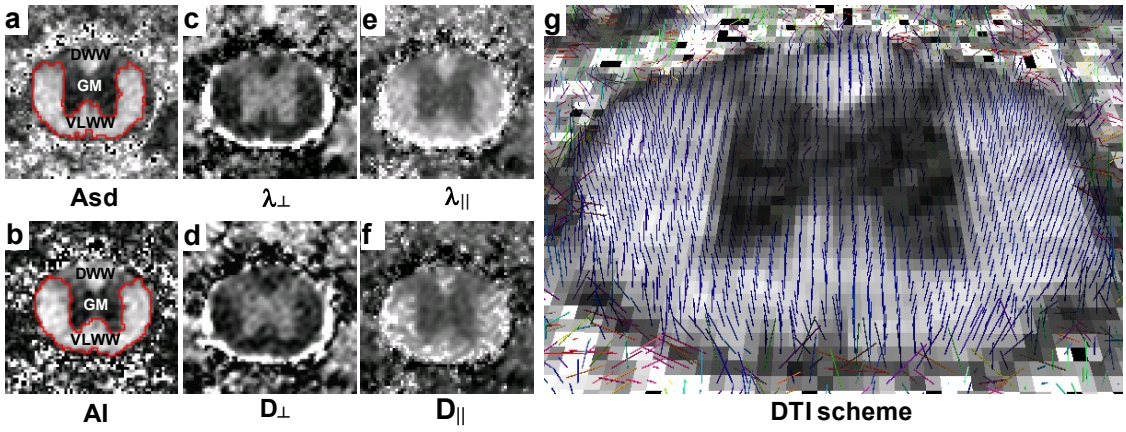

Figure 3-2. Representative control spinal cord images of T9 vertebra level obtained from DTI and DWI: diffusion anisotropy, Asd and AI (a, b); diffusivity transverse to the VLWM tract, $\lambda_{\perp}$ and $D_{\perp}$ (c, d), and diffusivity parallel to the fiber tract, $\lambda_{||}$ and $D_{||}$. (e, f). Cerebral spinal fluid (CSF) is clearly seen in the $\lambda_{\perp}$, $D_{\perp}$, $\lambda_{||}$ and $D_{||}$ maps enabling the identification of the cord parenchyma. Regions of DWM (DWM), VLWM and GM are readily visualized in the anisotropy maps, as well as in all other diffusion index maps. The manually

segmented ROI of GM and VLWM were used to quantify the group-averaged parameters of each region. The pixel-based whisker plots show the principal diffusion direction obtained by DTI scheme (g, with Asd background) based on the calculation of tensor eigenvectors in each pixel.

The group-averaged diffusion parameters of the manually segmented VLWM and GM in the control spinal cord are listed in Table 3-1. Consistent with our previous reports, $\lambda_{||}$ was higher in VLWM than in GM and $\lambda_{\perp}$ was higher in GM than that in VLWM [32, 33, 58]. The same trend was also seen in $D_{||}$ and $D_{\perp}$. Overall, $\lambda_{||}$ and $D_{||}$ were approximately seven-fold the values of $\lambda_{\perp}$ and $D_{\perp}$ in VLWM, and two-fold those in GM. $D_{||}$ was slightly lower than $\lambda_{||}$ in both GM and VLWM (~10%, $p < 0.01$), while $D_{\perp}$ and $\lambda_{\perp}$ had no significant difference. AI was slightly higher than Asd in VLWM (~3%, $p < 0.05$). However, there was no difference between AI and Asd in GM except in the T10 vertebral segment (~10%, $p < 0.05$).

Table 3-1 The group-averaged diffusion parameters from six-direction DTI and two-direction DWI scheme of the manually segmented VLWM and GM in the control spinal cord.

ROI	Segment	Asd	AI	*p*	$\lambda_{\perp}$ ($\mu m^2/ms$)	$D_{\perp}$ ($\mu m^2/ms$)	*p*	$\lambda_{||}$ ($\mu m^2/ms$)	$D_{||}$ ($\mu m^2/ms$)	*p*
VLWM	T8	0.70 ± 0.02	0.73 ± 0.04	< 0.05	0.28 ± 0.03	0.29 ± 0.04	0.59	2.07 ± 0.10	1.84 ± 0.14	< 0.01
	T9	0.71 ± 0.02	0.75 ± 0.03	< 0.05	0.26 ± 0.02	0.26 ± 0.03	0.45	2.01 ± 0.07	1.80 ± 0.11	< 0.01
	T10	0.71 ± 0.02	0.74 ± 0.02	< 0.05	0.24 ± 0.03	0.25 ± 0.03	0.19	1.93 ± 0.09	1.73 ± 0.08	< 0.01
GM	T8	0.26 ± 0.04	0.26 ± 0.04	0.99	0.55 ± 0.06	0.57 ± 0.04	0.29	1.07 ± 0.08	0.98 ± 0.08	< 0.05
	T9	0.22 ± 0.03	0.24 ± 0.05	0.37	0.59 ± 0.04	0.59 ± 0.04	0.97	1.03 ± 0.07	0.96 ± 0.08	< 0.05
	T10	0.21 ± 0.03	0.17 ± 0.03	< 0.05	0.58 ± 0.04	0.60 ± 0.04	0.14	0.95 ± 0.05	0.85 ± 0.04	< 0.01
VLWM/GM	T8	2.75 ± 0.36	2.84 ± 0.31	0.45	0.45 ± 0.11	0.50 ± 0.05	0.16	1.94 ± 0.10	1.88 ± 0.13	0.16
	T9	3.28 ± 0.42	3.27 ± 0.59	0.96	0.39 ± 0.09	0.45 ± 0.05	0.06	1.95 ± 0.09	1.87 ± 0.11	0.07
	T10	3.56 ± 0.54	4.55 ± 0.68	< 0.01	0.39 ± 0.10	0.42 ± 0.04	0.89	2.04 ± 0.06	2.04 ± 0.06	0.27

In the injured cord, the contrast between VLWM and GM were reduced in the diffusion index maps of both schemes (Fig. 3-3). The evolution of diffusion parameters from T8 to T10 was monitored by manual ROI analysis. The trends of AI, $D_{||}$, and $D_{\perp}$ paralleled that of Asd, $\lambda_{||,}$ and $\lambda_{\perp}$ (Fig. 3-4). Both DTI and DWI detected a similar trend of

decreased diffusion anisotropy, decreased axial diffusivities, and increased radial diffusivities in the VLWM tract, indicating axonal injury and myelin damage.

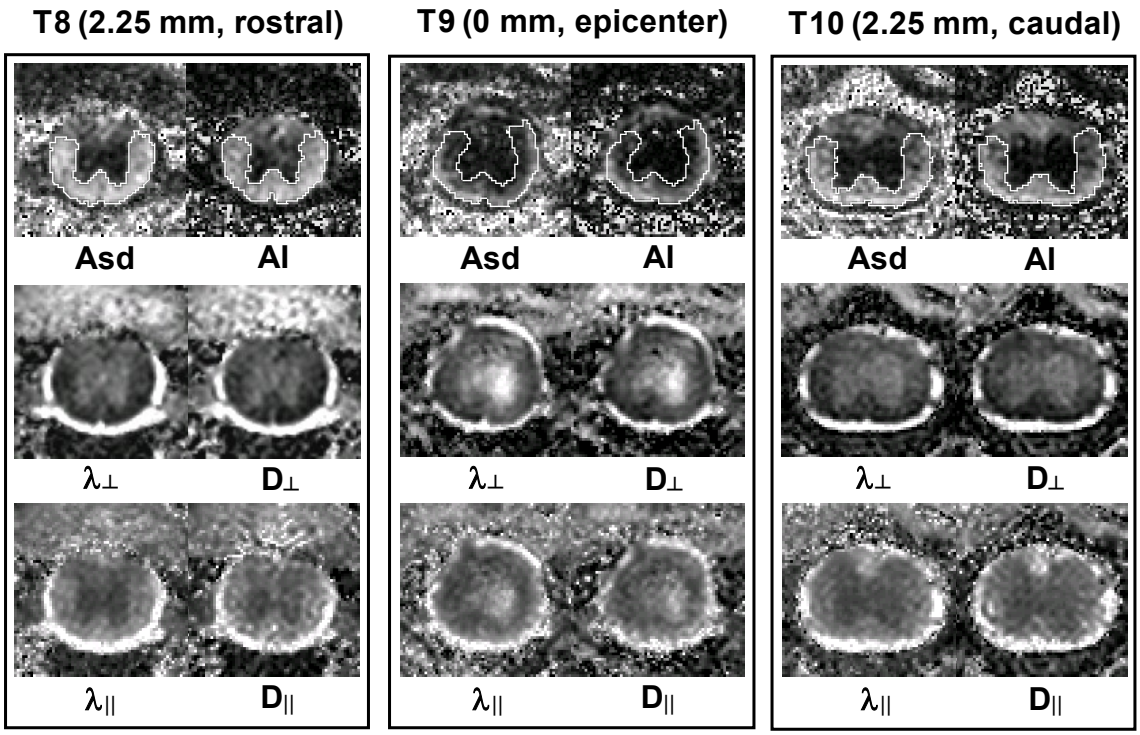

Figure 3-3. Representative images of the injured spinal cord from DTI (left column in each panel) and DWI (right column in each panel) covering segments of T8 (2.25 mm rostral), T9 (0 mm, epicenter), and T10 (2.25 mm caudal) are presented. Both schemes provide good quality images of the injured cords enabling easy ROI analysis. The manually segmented ROIs of total VLWM on the anisotropy maps at T8, T9 (epicenter), and T10 were used to quantify the group-averaged value of each slice (data shown in Fig. 3-4). In the Asd and AI maps, the residual normal appearing VLWM represents the spared VLWM, where the myelinated axons are mostly intact.

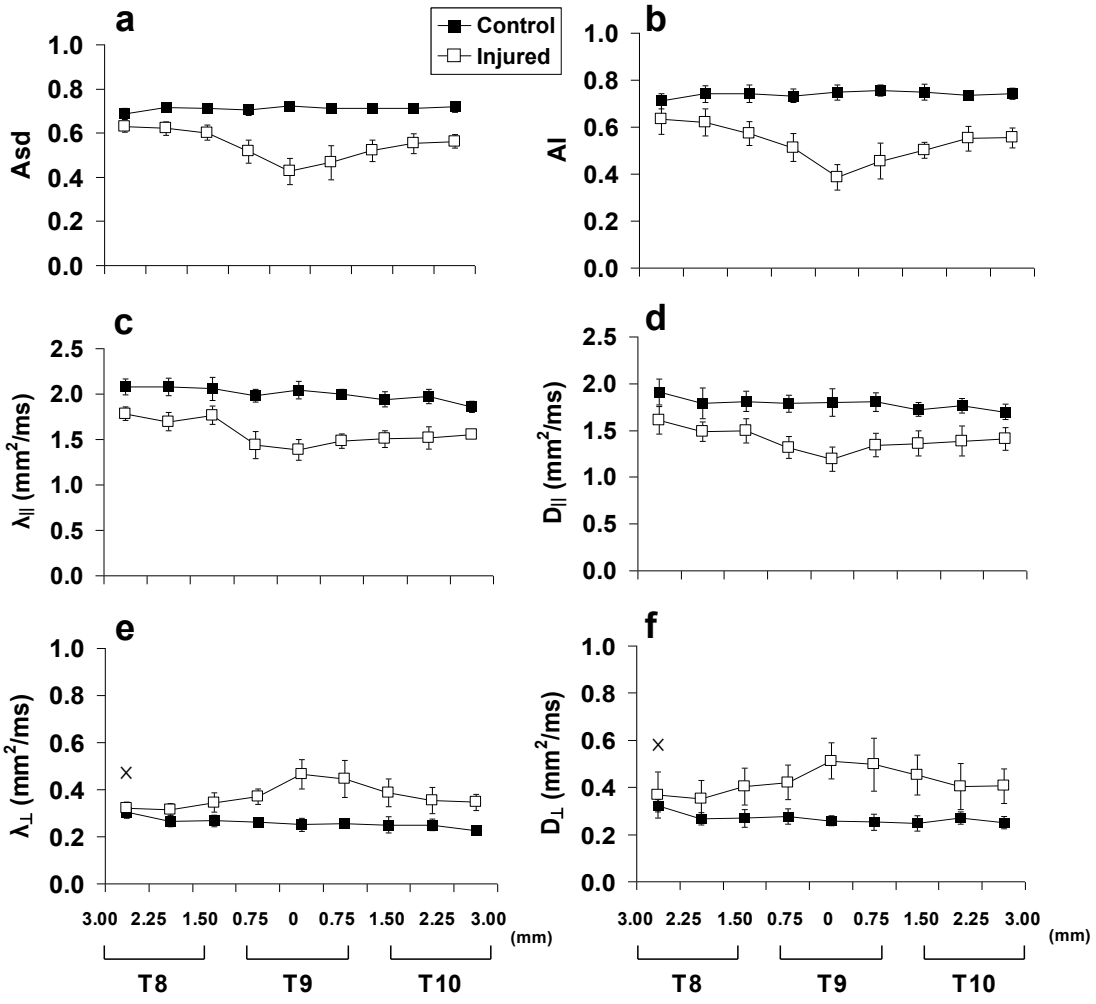

Figure 3-4. Spatial evolutions of DTI (a, c, e) and DWI (b, d, f) parameters from T8 to T10 in the control (■) and injured (□) cords. Decreased $\lambda_{||}$ and $D_{||}$ (c, d), and increased $\lambda_{\perp}$ and $D_{\perp}$ (e, f) are seen at the injury epicenter. At 14 days following the contusion SCI, both DTI and DWI measured the same trend of changing diffusion indices reflecting both axon and myelin damages at the site of impact. Group-averaged Asd and AI of a contusion injured spinal cord clearly demonstrate the spatial evolution of the injury. The quantification was done by manually defined ROIs of total VLWM. All parameters between the control and injured groups are statistically significantly different at all image slices except the first slice, marked with ×, of $\lambda_{\perp}$ and $D_{\perp}$.

After applying thresholds to the Asd (0.42) and AI (0.48) maps, the regions of normal appearing VLWM were compared and evaluated by the overlap index (Fig. 3-5a).

A greater than 93% agreement in Asd- and AI-detected normal appearing VLWM was evident with a significant ROI overlap. The difference between ROI_{Asd} and ROI_{AI} existed mainly at the border of VLWM where partial volume effect is inevitable transitioning between tissue types (Fig. 3-5b). The similar agreement was also seen in the normal appearing VLWM of the injured cords. However, the degrees of overlap at the injury epicenter (75.9 ± 5.4 %) were relatively lower than that at sites 0.75 mm rostral (85.7 ± 2.2 %) or caudal (83.2 ± 3.0 %) to the epicenter. The degrees of overlap of control cords showed no difference among all segments. The normalized area measured using Asd or AI from T8 to T10 was comparable (Figs. 3-6a and 3-6b).

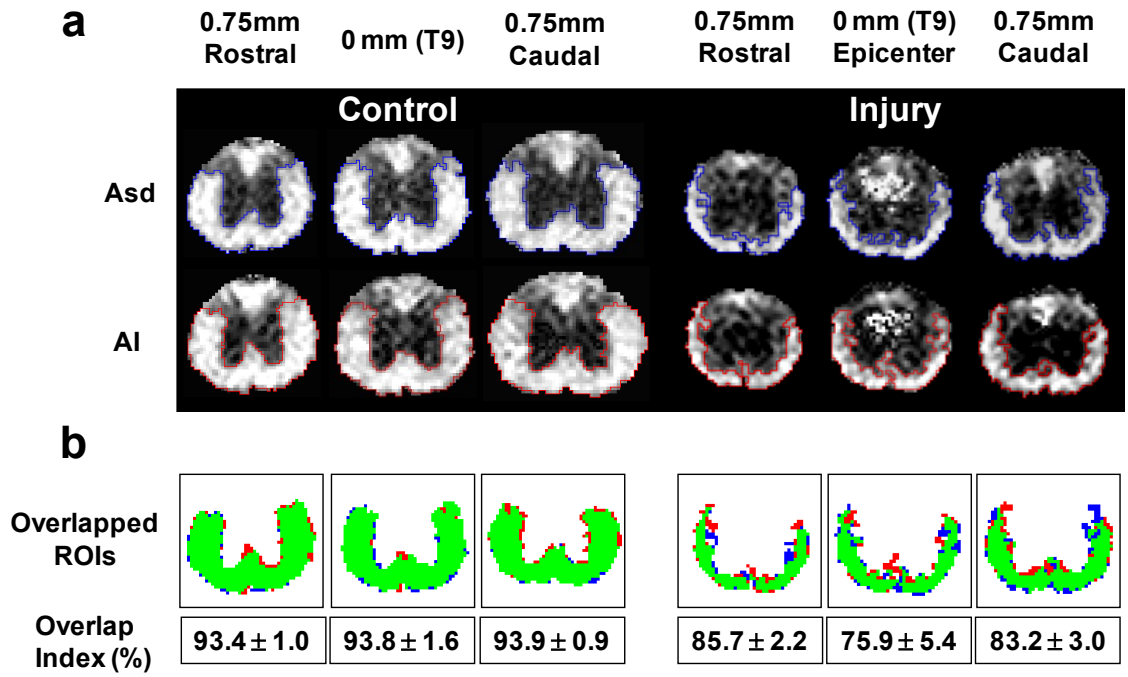

Figure 3-5. (a) Normal appearing VLWM of control (left panel) and injured cords (right panel) were estimated using Asd and AI thresholds. Three representative images from each cord (epicenter, i.e., 0 mm, and 0.75 mm rostral and caudal to the epicenter) at T9 vertebra level were compared. (b) The pixels identified within both ROI_{Asd} and ROI_{AI} are color coded in green. The inconsistent pixels are marked in red (outside of ROI_{Asd}) and blue (outside of ROI_{AI}). The major discrepancy is seen at the border of GM-WM and

parenchyma-CSF. In general, the overlap index averaged ~94% for the control cords (n = 5), and ~80% for that of injured cords (n = 7).

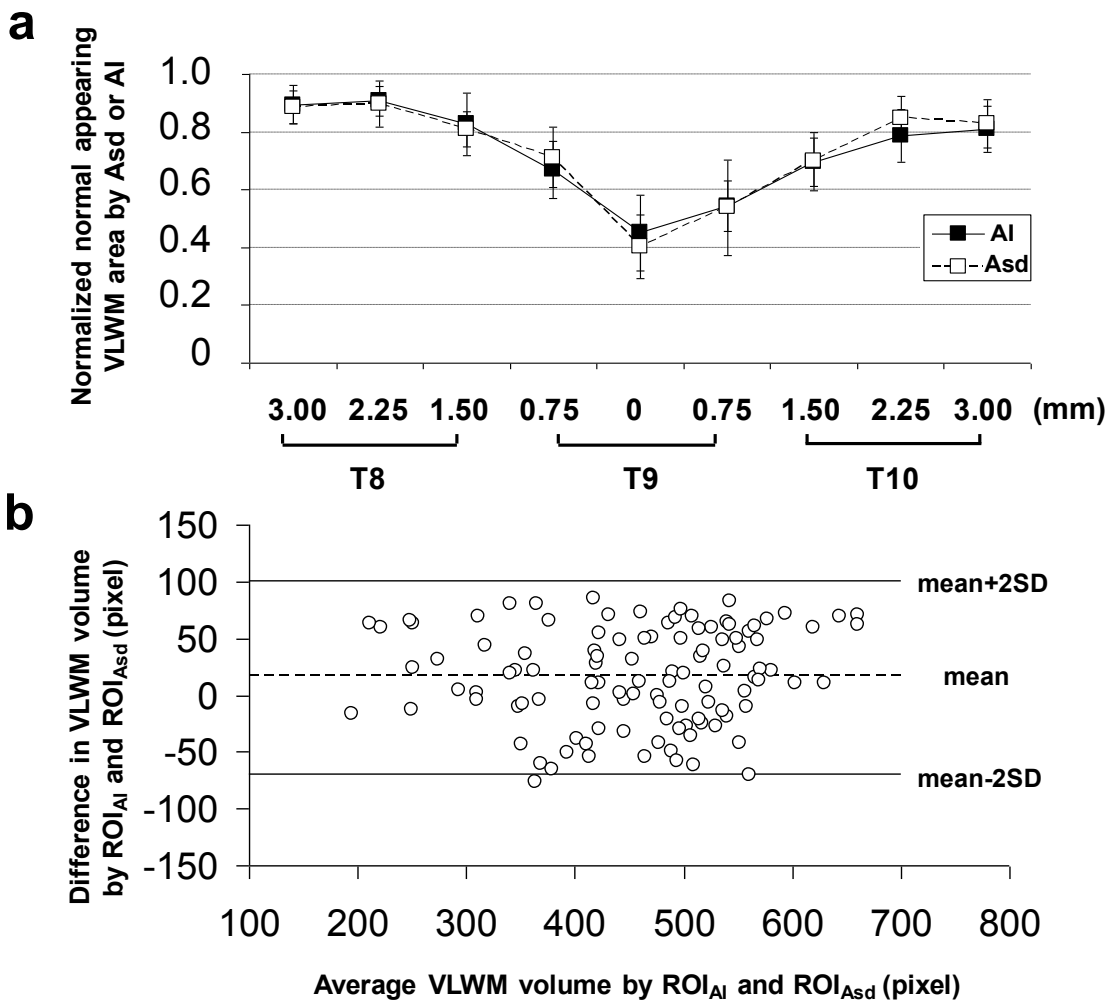

Figure 3-6. (a) The normal appearing VLWM areas of the injured cords were assessed using Asd and AI. The areas were normalized by the amount of total VLWM of the control cords ($r = +0.89$, $n = 63$, $p < 0.0001$). (b) Bland-Altman plot displays the difference of normal appearing VLWM areas determined by Asd and AI against the average of Asd and AI assessments from the 108 paired measurements in the study. The difference between normal appearing VLWM measurements using Asd and AI lies within the limit of agreement (95%, mean $\pm$ 2 x SD).

The spinal cords were stained with LFB to assess the contents of spared VLWM from the epicenter at 14 days after injury. Myelinated tracts of the DWM, VLWM were

stained blue in normal controls (Fig. 3-7a). After the contusion SCI, the injury resulted in extensive loss of LFB stained area in the WM (control: 0.98 ± 0.04 mm2, injury: 0.61 ± 0.15 mm2). The MR determined normal appearing VLWM and LFB determined spared VLWM were in close agreement (Fig. 3-7b). Furthermore, the spared VLWM areas also correlated with BMS (Fig. 3-7c).

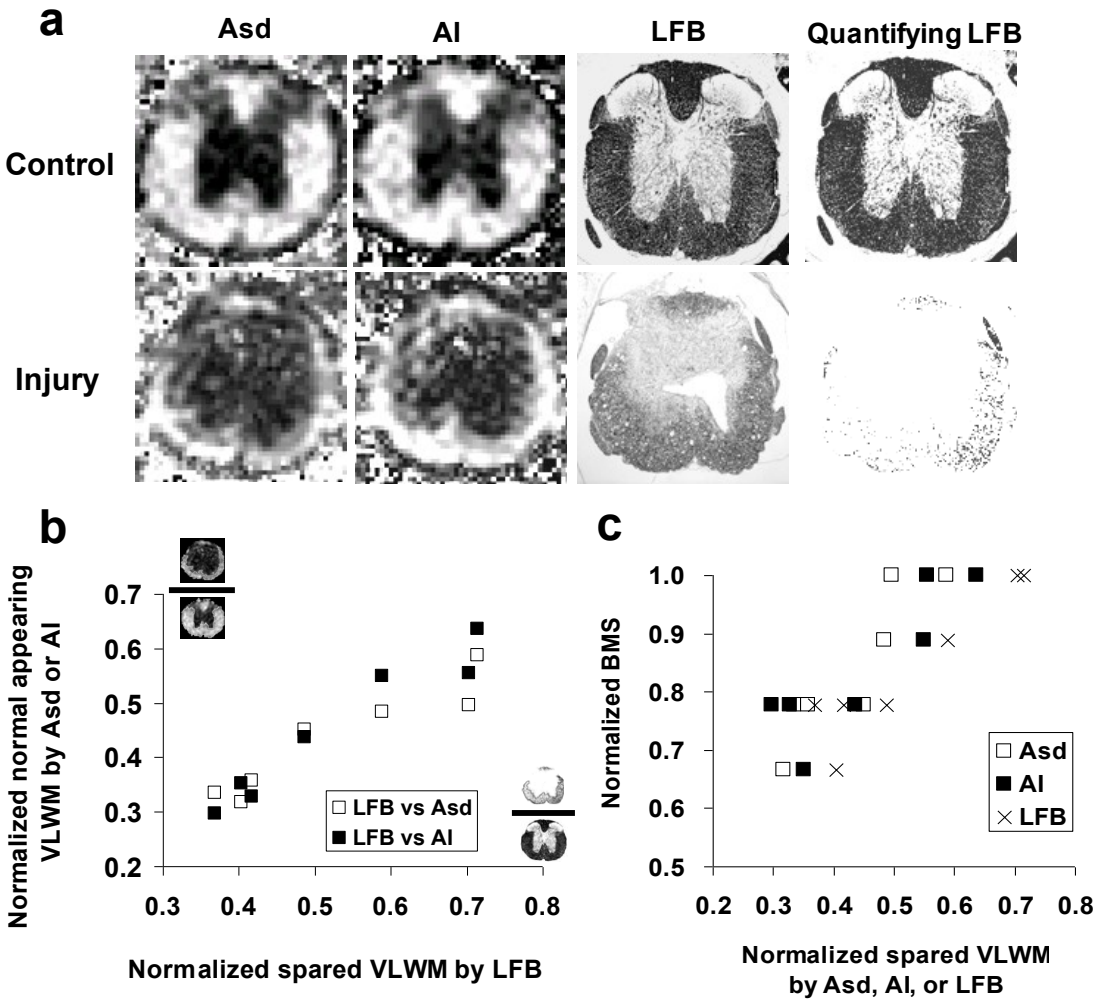

Figure 3-7. (a) Corresponding images of Asd, AI, and LFB staining. The gray-scaled LFB images are normalized by the LFB staining intensity of the uninjured nerve roots to quantify the extent of spared VLWM. In the control cords, images from DTI, DWI, and histological staining show a similar pattern across the region of VLWM, indicating the integrity of axons and myelin sheaths. For the injured cords, mild to moderate WM

injuries were observed in the histological maps at the impact epicenter at 14 DPI, consistent with the Asd and AI maps. (b) The correlation between the normalized LFB and Asd/AI assessed normal appearing VLWM. (LFB vs. Asd: r = +0.97, n = 7, p (correl) < 0.001; LFB vs. AI: r = +0.95, n = 7, p (correl) = 0.001). (C) Spared VLWM areas assessed using all three methods correlated well with the BMS scores at 14 DPI. (LFB vs. BMS: r = +0.86, n = 7, p (correl) = 0.01; Asd vs. BMS: r = +0.89, n = 7, p (correl) < 0.01; AI vs. BMS: r = +0.87, n = 7, p (correl) = 0.01).

3.1.4 Discussion

In this study, the capability of detecting mouse spinal cord VLWM injury using six-direction DTI and two-direction DWI was compared. Our results showed comparable image qualities from both schemes allowing segmentations of the region of DWM, GM, and VLWM. Fourteen days after injury, both $\lambda_{||}$ and $D_{||}$ decreased, while both $\lambda_{\perp}$ and $D_{\perp}$ increased suggestive of axonal and myelin damage respectively. Significant overlap of Asd and AI determined normal appearing VLWM was observed: ~93% for the control cords and ~80% for mild-to-moderately injured cords. The detected spared VLWM were validated by LFB staining and correlated with the BMS scores. The acquisition time for the two-direction DWI was 57% shorter than the time required for the six-direction DTI.

The role of DTI parameters in evaluating the contusion SCI WM pathology was recently investigated [33, 35, 58, 61, 62, 88, 91]. The decreased $\lambda_{||}$ correlated with axonal injury, while the increased $\lambda_{\perp}$ reflected myelin damage. Loy et al. [58] further demonstrated that $\lambda_{||}$ is able to differentiate the injury severity in the hyper-acute phase (within 6 hrs of injury). Our other reported studies also demonstrated that increased $\lambda_{\perp}$ paralleled the myelin damage secondary to retinal ischemia in the mouse optic nerve [74, 102]. The diffusion anisotropy reflects the combined effect of $\lambda_{||}$ and $\lambda_{\perp}$, and is capable of detecting WM integrity (without distinguishing axonal vs. myelin damage) [33, 35].

Similarly, the measured $D_{||}$ and $D_{\perp}$, from the two-direction DWI, also reflected the axonal and myelin injury in the present study (Fig. 3-4). Although statistically significant differences were seen between $\lambda_{||}$ and $D_{||}$ (~10%) as well as Asd and AI (~3%) in the control animals, the two-direction DWI indices correctly reflected the injury extent in the SCI animals as assessed by DTI. At 14 days after injury, our data showed the decreased $\lambda_{||}$ and $D_{||}$ and the increased $\lambda_{\perp}$ and $D_{\perp}$ in the SCI animals without a significant difference between the two schemes of measurements. The difference between the $\lambda_{||}$ and $D_{||}$ in the control animals might be caused primarily by the inherently different signal attenuations between different diffusion encoding schemes (i.e. six-direction 12-cube-edge and two-direction orthogonal encoding). The data from the injured cord group still demonstrated the adequacy of two-direction DWI in detecting axonal and myelin damages.

The efficacy of therapeutic interventions on the functional recovery of rodent SCI has been evaluated by examining the extent of spared VLWM [8, 103, 104]. In a series of rat studies, Basso and colleagues [105] analyzed locomotor outcomes after mild, moderate, or severe spinal cord contusion with extensive (> 40%), intermediate (15% - 40%), or minimal (1% - 14%) tissue sparing determined by LFB staining at the lesion epicenter. They found that locomotor recovery was extensive after mild SCI with extensive axonal sparing (> 40%), but was quite limited after severe SCI with little sparing (as low as 1% - 2%). Our recent study investigating the effect of different impact speeds ranging from 0.1 to 0.4 m/s on the severity of contusion SCI [35] demonstrated that *in vivo* DTI estimated spared VLWM content in the sub-acute phase correlated well with those determined using postmortem histology and behavioral test in the chronic phase.

In the present study, all the injured mice showed intermediate to extensive recovery, with 30% - 60% preserved normal appearing VLWM. Although LFB staining consistently estimated larger preserved VLWM areas than MR measurements, probably due to the residual myelin debris, the correlation between histology and MR images was statistically significant. Most importantly, the MR estimated extent of spared VLWM correlated with behavioral scores (Fig. 3-7c). These findings support that tissue sparing at the lesion epicenter determined in the sub-acute phase (7 - 14 day after injury) correlates with the chronic behavioral disability (14 - 21 days after injury) in the experimental spinal cord contusion.

Early studies using two-direction DWI scheme to study the spinal cord have been performed by accurately aligning the cord to the magnet axes. This was easily achieved on *ex vivo* tissues. However, for an *in vivo* study, it is more difficult to align the spinal cord to the magnet axes of reference. If the segment of interest fails to align with an axis in the magnet frame of reference while the diffusion weighting gradient is still aligning with the magnet axes, the measured ADC values need to be corrected [96]. In the current study, we attempted to reproduce the literature finding with the spine and diffusion weighting gradients aligning with the magnet axes. The correct cord alignment was confirmed by the fact that the principal eigenvector of the WM tract (Figs. 3-2g and h) derived from the DTI were parallel to the magnet z-axis. However, when imaging of the entire human spinal cord is attempted, the curvature of the spine would make it difficult to align the axis of the spine with the magnet z-axis. To employ the two-direction DWI for ADC measurements in this instance, parallel and perpendicular diffusion weighting gradients would need to be aligned according to the curvature of different segments. As the gradients can be manipulated arbitrarily nowadays, small segments of spine could be imaged in this fashion by first assessing directionality with scout images

and then applying appropriate orthogonal gradients. The only drawback of using two-direction DWI would be the need to group the spinal segments according to its curvature of the SCI patients during the planning of scout images. However, this will not prohibit its use since segmented imaging of a human spine is typically necessary even for the DTI data acquisition.

3.2 To Gain SNR: Multiple Spin-Echo DTI and Phased Absorption Images

Abstract

Diffusion MRI using a Stejskal-Tanner spin-echo (SE) sequence remains one of the best approaches in the rodent central nervous system due to its unrivaled image quality and ease of use. Since diffusion weighted (DW) SE requires lengthy scan time, a DW multiple spin echo (MSE) variation has been introduced. In this design, images from multiple echoes are averaged in order to improve the signal-to-noise ratio (SNR) without increasing the imaging time. However, images averaged using complex data suffer from artifacts caused by phase variations resulting from the imperfect 180-pulse, diffusion weighting, and physiological motion; whereas images averaged using magnitude values suffer from non-Gaussian noise distributions reducing the SNR gain and measurement accuracy. Herein, we demonstrate the benefit of averaging DW MSE images using appropriately phased absorption mode images eliminating phase artifacts and noise correlations of DW MSE applications. Our data indicates that averaging through absorption mode MSE images could yield a 1.85-fold increase compared to the magnitude averaged MSE images and 2.4-folds increase in SNR compared to the single SE images. We applied this acquisition procedure to show its advantage in studying a mouse model of spinal cord injury (SCI).

3.2.1 Introduction

A spin-echo (SE) sequence incorporating the Stejskal-Tanner diffusion-weighting (DW) gradient has been commonly used to achieve the needed high resolution and signal-to-noise ratio (SNR) for diffusion MRI of the rodent central nerve system [33, 58, 74, 99]. However, DW SE is hindered by long acquisition times that can limit throughput and make the diffusion measurement more vulnerable to bulk movement such as respiratory motion as well as the within tissue motions [106]. These motion artifacts severely degrade data quality resulting in inaccurate diffusion coefficient estimation. One potential sequence design is to increase efficiency of data acquisition by applying a train of refocusing pulses following the radio frequency (RF) excitation to acquire multiple echoes [107, 108].

Echo planar imaging is the fastest imaging sequence known using a gradient echo train to acquire an image in a fraction of second [109]. However, it cannot be used in the high resolution spinal cord imaging due to large susceptibility distortions. On the other hand, the spin-echo based multiple echo sequence, such as fast-spin-echo (FSE), retains the high spatial resolution of the spin-echo techniques while achieving a faster acquisition time through the use of multiple echoes [110-112]. The FSE multiple echo sequences are not without their own complications. Image blurring and ghosting are two common artifacts originated from amplitude and phase modulations of the FSE k-space data [106, 110, 112, 113]. The phase variation along the phase-encoded direction could become more complicated in the FSE when the diffusion gradients are applied.

An alternative way of sampling multiple echo k-space data is a multiple-echo spin echo (MSE) type of sequence [95]. In MSE, each echo fills its own independent k-space before signal averaging. The advantage of MSE imaging scheme is to maximize the

signal averaging in each phase encode (PE) step without bringing in extra phase error due to PE gradient. This approach is expected to improve signal-to-noise ratio (SNR) and provide additional T2 estimation from a series of spin echo train [114]. MSE imaging schemes are usually the choice if high quality image is desired, while the FSE is better for a faster acquisition, but trading off some of the image quality.

Ideally, signal averaging using complex data maximizes the SNR increase. In practice, however, the phase variations caused by motion or hardware imperfections often results in significant signal degradation when averaging multiple echoes [106, 113]. Averaging multiple-echo images using absolute-value images, i.e. magnitude images, avoid the image-to-image phase variation. Multiple echo SE-EPI acquisition to improve the acquisition efficiency was investigated previously [114]. Theoretically, comparing to the SNR of a single echo image, a three-echo MSE image could achieve a 1.36-fold increase of SNR in the white matter (WM) region (T2=80ms). However, generating a magnitude image changes the noise of original complex image from a Gaussian to a Rician distribution. Upon averaging multiple magnitude images, the noise distribution reduces skewness but moves the mean to a non-zero offset. This results in elevating the measured pixel intensity and limiting the SNR gain through averaging. Although a non-zero mean noise distribution has little effect at high SNR, it can bias measurements at low SNR (18-20, 34), a critical issue in diffusion-weighted images and the resulting diffusion tensor calculations [115-117].

Alternatively, appropriately phasing the complex MSE data prior to averaging allows the theoretical gain in SNR of multiple echoes to be fully realized while eliminating phase artifacts. Herein, we demonstrate the advantage of averaging MSE data with absorption-mode images phased using Bayesian probability theory. It eliminates phase artifacts, noise correlations, and improves SNR by nearly 1.85-fold compared to the conventional

magnitude averaged MSE images without additional increases in acquisition time. We applied this acquisition procedure to show its advantage in studying a mouse model of spinal cord injury (SCI).

3.2.2 Materials and Methods

Multiple Spin Echo Data Acquisition

A conventional Stejskal-Tanner DW sequence was modified to acquire MSE by a variable-length Carr–Purcell–Meiboom–Gill (CPMG) train of 180° pulses (Fig. 3-8). Inter-echo spacing (ΔTE) was minimized in order to maximize the signal from each of the echoes in T2 decay. Because this violates the CPMG conditions, suppression of secondary echoes was crucial [95, 118, 119]. Crusher gradients of alternating polarity in the slice-select direction were experimentally optimized in a water phantom**.** Modified sinc 180° pulses were used to compensate for pulse imperfection [95, 120]. All experiments were conducted on a 4.7 T magnet (Oxford Instruments, Abingdon, UK) equipped with a 15-cm inner diameter, actively shielded Magnex gradient coil (60 G/cm, 270 μs rise time). The magnet, gradient coil, and IEC gradient power supply is interfaced with a Varian DirectDrive console (Varian, Inc., Palo Alto, CA) with a Linux operating system.

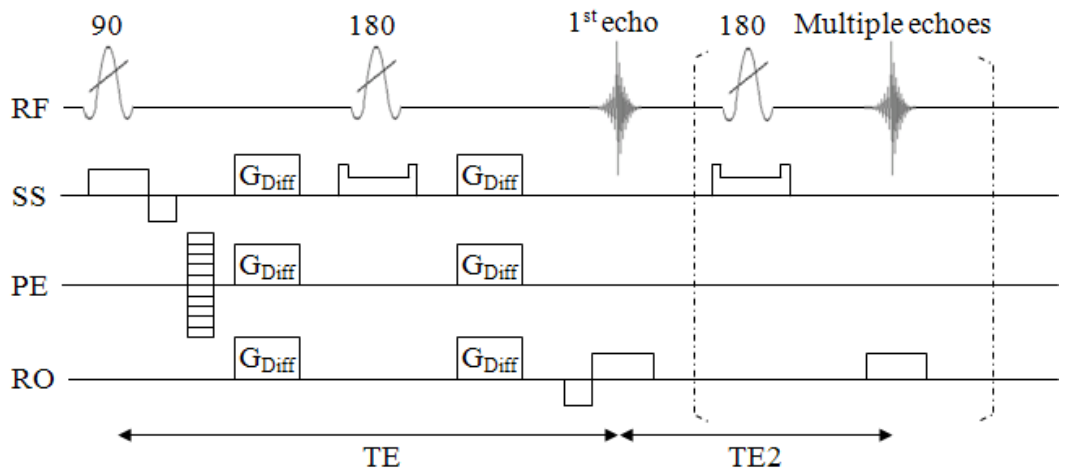

Figure 3-8. DW MSE pulse sequence diagram. A conventional pulsed gradient spin-echo diffusion preparation is followed by a multiple echo readout. The phase encode step and the diffusion gradient pair are outside the MSE acquisition loop ensuring each of the multi-slice MSE undergoing the same diffusion weighting in the same k-space line. A crusher gradient pair is added into the refocusing pulse to eliminate secondary echoes by alternating the sign for each successive echo.

Absorption Mode Image Generation

Absorption mode images were generated using Bayesian probability theory to independently estimate the phases for each echo from the multiple echo chain [121, 122]. In the Bayesian analysis, given the standard deviation of the noise prior probability, σ, all of the data, *D*, and the background information, *I,* the posterior probability for the phase, $P(\theta|\sigma DI)$, is used to estimate the phase, θ. The appendix gives the details of the Bayesian calculation. The full derivation is given in Bretthorst's original papers [121, 122]. Once the pixel-wise phase is estimated, the coherent signals are phased using:

$$S_{pi} = S_i exp\{-i\hat{\boldsymbol{\theta}}\}, \quad (3\text{-}6),$$

where the S_i is the original *i*th voxel signal, S_{pi} is the value if the i'th voxel after phasing, and $\widehat{\boldsymbol{\theta}}$ is the estimated phase. Theoretically, the absorption mode image gives a $\sqrt{2}$ increase in SNR since the full signal is recovered and only half of the noise is presented in the real channel [121, 122]. The phased diffusion weighted images (DWIs) were then averaged for least-square fitting the diffusion tensor [123].

Imaging Studies

The DW MSE sequence was first applied on a cylindrical 1-cm diameter tube of water placed in a custom-made solenoid coil for imaging at 17^{o} C. Six diffusion sensitizing gradients were employed for deriving diffusion tensor imaging (DTI): (Gx,Gy,Gz) = (1,1,0), (1,0,1), (0,1,1), (-1,1,0), (0,-1,1), (1,0,-1). The other acquisition parameters were: TR 1500 ms, TE 30 ms, ΔTE 12 ms, Δ 15 ms, δ 5 ms, b-value 0 and 1000 s/mm^2, FOV 3 × 3 cm^2, data matrix 128 × 128, number of echoes (ne) 16, number of averages 2, and acquisition time 30 min.

The in vivo DW MSE data was acquired on the mouse spinal cord. Female C57BL/6 mice, weighing 18 - 22 g, underwent T9 contusion SCI (n = 5) or sham operated control (n = 5) following previously reported procedures [33, 58, 124, 125]. All surgical preparations, pre-, and post-surgery care were provided in accordance with the Public Health Service Policy on Humane Care and Use of Laboratory Animals, Guide for the Care and Use of Laboratory Animals (Institute of Laboratory Animal Resources, National Research Council, 1996), and with the approval of the Washington University Animal Studies Committee. At seven days after surgery, all mice underwent in vivo DTI of spinal cord using DW SE and DW MSE sequences. Mice were anesthetized with an isoflurane/oxygen mixture (5% isoflurane for induction and 0.7 - 1.5% isoflurane for maintenance). Body temperature was maintained at 37° C by a circulating warm-water

pad. Actively decoupled Helmholtz volume coil and saddle-shape surface spine coil were used as the transmit-receive pair. DWIs were acquired with TR ~1200 ms, TE 31 ms, ΔTE 12 ms, Δ 15 ms, δ 5 ms, b-value 0 and 1000 s/mm^2, FOV 1 × 1 cm^2, data matrix 128 × 128 (zero-filled to 256×256), slice thickness 1 mm, ne 4, number of averages 4, and the acquisition time was ~60 min. A crusher gradient pair of 10 G/cm with 1 ms duration was added in the slice selection direction for all experiments. The b-values of the diffusion gradient were taken into account for all imaging gradients by numerical integration of the following equation [75, 93]:

$$b = \gamma^2 \int_0^t \left[\int_{t'}^t G(t'')dt''\right]^2 dt', \quad (3\text{-}7)$$

Averaging Method Comparison

The multiple echoes, generated using MSE sequence, were averaged using magnitude images (MSE-Magnitude), or absorption mode images (MSE-Absorption). The comparison was first conducted on the phantom data. Three eigenvalues (λ_1, λ_2, λ_3) were calculated from the diffusion tensor matrix. The eigenvalue-derived parameters including trace of the mean diffusivity (Tr), axial diffusivity ($\lambda_{\|}$), radial diffusivity ($\lambda_{\perp}$), and relative anisotropy (RA) were calculated as previously reported [74, 84]. Region-of-interest (ROI) based comparisons between different methods of echo averaging were performed. The ROI of the phantom image encompassed the center portion of the tube; the ROI for the contusion SCI images encompassed the ventro-lateral white matter (VLWM). The estimated SNR was calculated according to the literature with consideration of the skewed Rician noise distribution for combining the sum-of-squares magnitude images [126-129]. Values of Tr and RA were reported for the phantom study. A paired student's t-test was performed to compare the DTI parameters between the control and the injured spinal cords. For statistical tests, both the probability of rejecting

the null hypothesis (p-values) and the standardized difference between means (Cohen's D) were reported as indicated [130]. Significance was set at p-value < 0.05.

3.2.3 Results

The effect of signal averaging through complex images, magnitude images and absorption mode images are illustrated in Fig. 3-9 and Fig. 3-10. The center of the k-space, i.e. maximum signal, was shifted along both readout and phase encoding directions between the first and second echoes (Figs. 3-9b, f). This results in an obvious phase mismatch between the first and second echoes (Fig. 3-9c, g). Phasing using Bayesian probability theory to produce absorption mode images removes the phase difference between successive echoes (Figs. 3-9d, h). Phase artifacts can be avoided by adding magnitude images as opposed to complex images (Fig. 3-10a b). However, the resulting Rician noise reduced the SNR gain (Fig. 3-10e). The noise distribution of the complex averaging appeared to be a Rayleigh distribution (Fig. 3-10d, g), while that of the magnitude averaging was a Rician distribution with a non-zero offset (Fig. 3-10g). The absorption-mode image averaging provided the best tissue contrast while maintaining a Gaussian distributed noise (Fig. 3-10c, f). The noise distribution of the MSE images after phasing exhibited a mean zero and therefore there was no noise bias in these images (Fig. 3-10g).

Phantom Study

The difference of *b*-value between each echo was ~7s/mm^2 in our imaging setting. Compared to the *b*-value of 1000s/mm^2, it is less than 1% and could be neglected. The non-DW MSE images of water phantom are shown in the Figure 3-11. Images from odd and even echoes have a different phase pattern, which will lead to artifacts in complex

image averaging. After phasing, the absorption mode image averaging shows a superior $\sqrt{2}$ increase in SNR compared to the magnitude averaging methods (Fig. 3-11c). This increase of SNR improves to 1.84-fold when averaging up to 3 echoes. Table 3-2 lists the mean Tr and RA values in the phantom ROIs used for the SNR analysis. The measured Tr of a water phantom was not different between four acquisition procedures. However, the RA values of the MSE are smaller and closer to isotropic than those obtained with SE-Magnitude with one or two averaging.

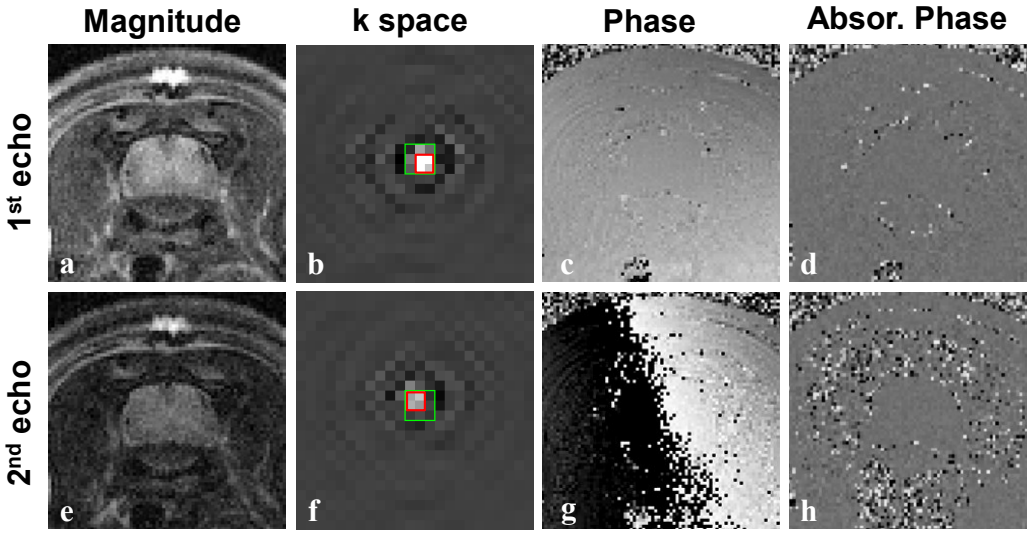

Figure 3-9. Phasing the images using Bayesian probability theory removes phase differences between successive echoes. In vivo mouse spinal cord images of the first (upper panel, a-d) and second echoes (lower panels, e-h). The k-space center (marked in black) is shifted along the geometric center of the image (marked in white) between the first and second echoes (b, f), as a result of phase variation seen in the MSE phase images (c, g). After appropriately phasing to generate the absorption-mode images, no such phase variation between echoes is seen in the absorption mode phase images (d, h).

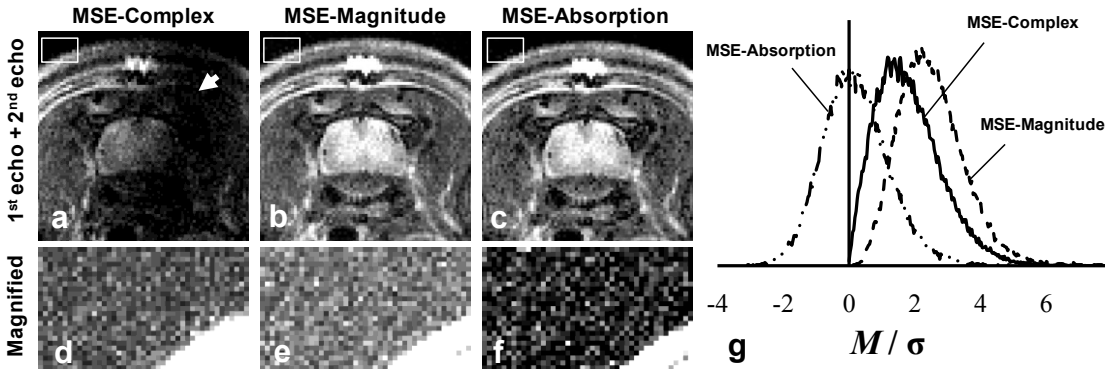

Figure 3-10. Averaging absorption mode images removes phase artifacts and preserves the noise characteristics. (a) Averaging MSE images using complex values results in an artifact (white arrow) due to incoherent phases between successive echoes. (b) Averaging magnitude images removes the phase artifact but results in non-zero offset Rician noise distribution which reduces the SNR improvement and may bias the diffusion tensor parameter estimates. (c) Averaging absorption-mode images eliminates errors due to phase artifacts and Rician noise. These absorption mode images display the greatest SNR of the three reconstruction methods and provide excellent tissue contrast in the spinal cord. The noise level of each image is shown in the expanded rectangular region (d-f). The images shown here are on the same intensity scale. Note that the non-zero mean Rician noise elevates the mean pixel intensity in the magnitude-averaged image (e). The noise distributions are measured in the noise-only region (g). The measured pixel intensity, M, is normalized by the noise standard deviation, σ.

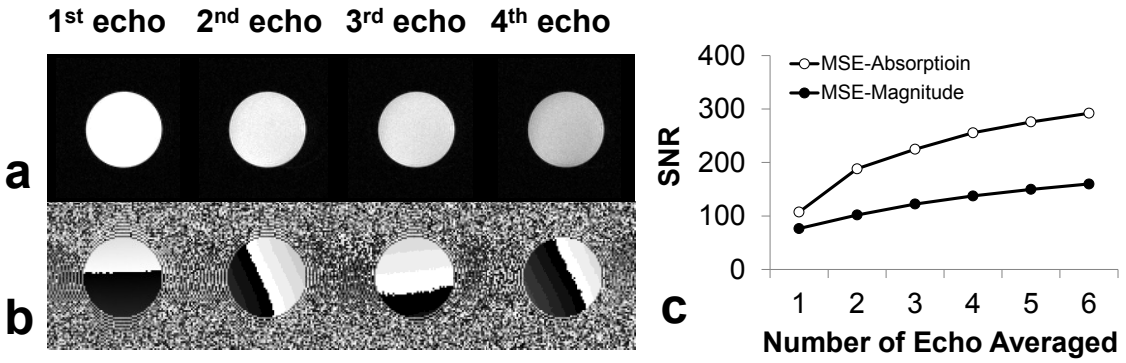

Figure 3-11. Magnitude (a) and phase (b) multiple echo images of a water phantom. The SNRs of the averaged multiple echo images (c). MSE-absorption shows superior SNR compared to the MSE-Magnitude.

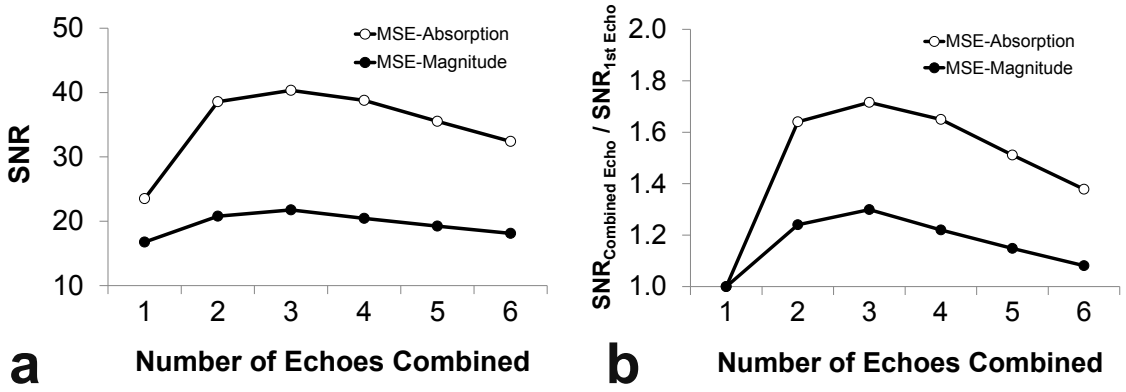

Figure 3-12. SNR (a) and SNR increase ratio (b) of the averaged MSE images. Signals are obtained from the VLWM of the mouse spinal cord. MSE-Absorption images clearly show higher gain in both SNR and the relative SNR increase.

in vivo Study on Mouse Spinal Cord Injury

Measuring from the VLWM in the non-diffusion (b = 0) mouse spinal cord images, the ratios of SNR increase of three echo averaging to that of the single SE were 1.30±0.08 for MSE-Magnitude image, and 1.85±0.06 for MSE-Absorption image; the measured SNRs were 21.77±1.42, and 40.34±1.72, respectively (Fig. 3-12). The

averaging methods of MSE data were compared between the control and injured spinal cords to test the sensitivity of detecting WM injury. The MSE-Absorption images provided the best image quality with the least noise in RA, Tr, $\lambda_{||}$, and $\lambda_{\perp}$ maps (Fig. 3-13). The measured diffusion parameters of the VLWMs are listed in Table 3-3. Decreased $\lambda_{||}$ and increased $\lambda_{\perp}$ were evident in the injured VLWMs, suggestive of axonal injury and myelin damage respectively at seven days post injury [33, 124, 125]. The difference between the control and injured group was more apparent in the MSE-Absorption maps than the MSE-Magnitude maps and in good agreement with those obtained with SE-Magnitude with four averaging. Correspondingly, the MSE-Absorption data showed statistically more significant changes (smallest p-value) with greater effect size (larger Cohan's d) between the control and injured groups.

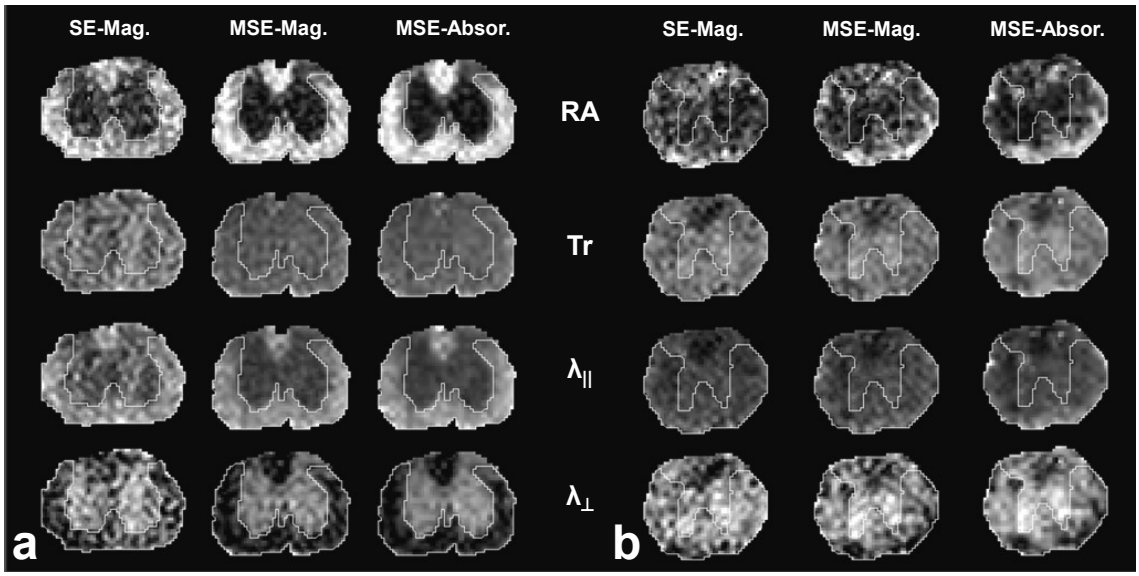

Figure 3-13. Diffusion index maps of spinal cords from the control (a) and contusion SCI (b) mice. The diffusion index maps are calculated from the average of two diffusion dataset and three echoes for MSE. The MSE-Absorption maps clearly show superior image quality of the mouse spinal cord facilitating the identification of both the control and injured spinal cord structure.

Table 3-2. Comparison between the mean RA and Tr values in a water phantom from the same dataset as in Fig. 3-11.

Method	Tr ($\mu m^2/ms$)	RA
SE-Magnitude (NEX=1)	5.79±0.14	0.079±0.03
SE-Magnitude (NEX=2)	5.77±0.11	0.064±0.02
MSE-Magnitude (NEX=1, Echoes=3)	5.83±0.08	0.048±0.02
MSE-Absoroption (NEX=1, Echoes=3)	5.85±0.08	0.047±0.02

Table 3-3 Comparison of SE-Magnitude, MSE-Magnitude and MSE-Absorption in diffusion parameters. Significant level (p-value) and effect size (Cohan's d) are reported between the control (n=5) and the injured spinal cords (n=5). All measurements except trace show significant difference ($p < 0.05$), and all measurements show a large effect ($d > 0.8$) between control and injury groups. MSE-Absorption measurements show the smallest p-value and the largest Cohan's d values.

Method	Group	RA		$\lambda_{\parallel}$ ($\mu m^2/ms$)		$\lambda_{\perp}$ ($\mu m^2/ms$)		Tr ($\mu m^2/ms$)	
SE-Magnitude (NEX=4)	Control	1.02±0.03	p<0.0001, d=13.21	1.94±0.12	p<0.0001, d=8.62	0.25±0.02	p<0.0001, d=7.21	2.48±0.09	p=0.07, d=2.07
	Injury	0.60±0.04		1.30±0.04		0.42±0.03		2.28±0.09	
SE-Magnitude (NEX=2)	Control	0.93±0.04	p<0.001, d=5.33	1.80±0.14	p<0.001, d=4.13	0.31±0.03	p<0.01, d=3.01	2.68±0.15	p=0.07, d=1.35
	Injury	0.62±0.08		1.38±0.10		0.46±0.07		2.48±0.18	
MSE-Magnitude (NEX=2, Echoes=3)	Control	0.98±0.02	p<0.0001, d=10.71	1.82±0.13	p<0.001, d=5.27	0.29±0.03	p<0.0001, d=5.03	2.45±0.18	p=0.19, d=1.51
	Injury	0.60±0.05		1.32±0.09		0.45±0.04		2.23±0.04	
MSE-Absoroption (NEX=2, Echoes=3)	Control	1.03±0.03	p<0.0001, d=15.06	1.96±0.13	p<0.0001, d=8.14	0.28±0.02	p<0.0001, d=8.26	2.42±0.17	p=0.07, d=2.12
	Injury	0.59±0.04		1.29±0.06		0.43±0.02		2.27±0.06	

3.2.4 Discussion

Signal averaging of complex data is a common practice to improve SNR. The effectiveness of this approach relies on the consistent phase of the acquired echoes, a condition not attainable in DW MSE dataset (Fig. 3-9b, f). Signal averaging of magnitude data has been widely employed in order to avoid the problems involved in incoherent phases of the MSE, [95, 118, 119]. Individual magnitude images are obtained as the

pixel-wise square root of the sum of squares of the real and the imaginary images. This operation results in the Rician distribution of the associated noise at low SNR [115, 116, 126]. Averaging through the magnitude images increases the measured pixel intensity with a higher noise level.

Absorption-mode images improve upon magnitude image averaging since the Gaussian noise distribution is preserved [121, 122]. If the phasing analysis was successful, only noise had left in the imaginary image. The coherent real signal, free of phase complication, was computed for each echo estimated independently from the multiple echo chain. Thus, the imaginary channel is not used in averaging: only the real images are averaged. As a result, averaging of phased absorption images from multiple echoes produces the SNR gain theoretically achievable when averaging without introducing phase artifacts. This solves both the phase incoherence problem, and the bias of the Rician noise distribution.

Bayesian probability analysis relies on the correct prior knowledge of the signal amplitude phase, and noise. This prior information can influence the accuracy of the resulting phase parameter estimation. For instance, DW MRI can inherently have low SNR when high b-values or long echo times are employed. In such a case of very low SNR image (SNR < 3), there is insufficient information for accurate phase estimation [121, 122]. The estimated noise standard deviation might be significantly larger than the true noise distribution. Thus, the effects of very low SNR echoes from the multiple echo acquisition should not be considered when using absorption mode images, although the averaging of magnitude images in this case may lead to considerably less accuracy. Also, irregular bulk movement in the DWIs, which are highly sensitive to motion artifact, can also introduce bias affecting the determination the noise standard deviation.

Several other methods could also potentially be used to deal with these issues of averaging MSE dataset. First of all, the phase variation between even and odd echo could be minimized by applying a more complicate phase cycle of the RF pulse train, though the variation may not be completely eliminated for echo averaging through complex data [131]. Alternative approaches such as Rician noise removal [115], or using maximum likelihood [117] could also be used to estimate the diffusion tensor from the averaged magnitude MSE images. More complicated, a joint analysis of unaveraged echoes that incorporates both estimations of the diffusion measurements as well as effects of T2 decay may provide a further increase in accuracy of the parameter estimates than could otherwise be obtained [123, 132]. The comparison of these MSE data processing methods is beyond the scope of this study and worthy to do to facilitate the high resolution diffusion MRI applied not only in animal but also in human studies.

In the present study, the SNR gain in VLWM was achieved by averaging up to three echoes. The optimal number of echoes to be added is determined by both the T2 relaxation of sample of interest and the hardware capabilities [118]. Clearly, short T2 relaxation time constants limit the number of echoes that can be utilized. Furthermore, the number of echoes is also limited by the RF refocusing pulse durations, imaging gradient rise times, and acquisition bandwidth. Since the goal of the MSE sequence was to gain SNR, ΔTE was minimized resulting in a non-CPMG condition. Sufficient crusher gradient pairs surrounding the refocusing pulses were necessary to reduce stimulated echoes [107, 108, 110]. In our Varian NMR spectrometer, the maximum gradient is 62 G/cm with 270ms rise time. In a typical data matrix of 128×128 with a 1 cm^2 field of view, the minimum achievable ΔTE was 12 ms, allowing 3 echoes for signal averaging to gain SNR in the VLWM region. This additional increase in SNR comes without an increase in

acquisition time. The gain in SNR led to a greater sensitivity to differences in diffusion properties between control mice and those with a spinal cord contusion injury. The effect sizes between the two groups were greatest with the MSE-Absorption for all DTI parameters. Therefore, the MSE absorption-mode averaging will allow either the use of smaller number of animals to achieve the same significance or detection of smaller differences. Our results indicate that the averaged absorption mode MSE images yields a SNR increase about 185% compared to the magnitude averaged MSE images. Using the absorption-mode multi-echo averaging and the DW MSE sequence affords the generation of in vivo DTI with significant time saving and image quality improvement.

3.2.5 Conclusion

We have implanted an MSE-Absorption acquisition procedure and demonstrated the advantage in improving the SNR without an increase in imaging time, phase artifacts or correlated noise compared to magnitude averaging. Our results indicate that averaging through absorption mode MSE images could yield a 2.4-fold increase in SNR compared to the single SE images. Thus, the proposed method should benefit the DWI by substantially improving throughput or increasing spatial resolution.

3.2.6 Appendix: Phasing the images using Bayesian probability theory

If d_i represents the *i*'th pixel in a complex image, then the pixels are related to the phase through a model given by:

$$d_i = A_i exp\{-i\theta\} + n_i \ \ (1 \leq i \leq N), \tag{3-8}$$

where A_i is the amplitude of the *i*th pixel and θ is the phase, n_i represents the complex noise, with total number of complex data value, *N*. Separating the complex model into its real parts, dR_i, and imaginary parts, dI_i, one has

$$d_{Ri} = A_i cos\theta + n_{Ri}, \tag{3-9}$$

$$d_{Ii} = -A_i sin\theta + n_{Ii}, \tag{3-10}$$

where n_{Ri} and n_{Ii} represent the real and imaginary parts of the complex noise. Given the standard deviation of the noise prior probability, σ, all of the data, *D*, and the background information *I*, the posterior probability for the phase, $P(\theta|\sigma DI)$, is computed by applying Bayes' theorem:

$$P(\theta|\sigma DI) = \frac{P(\theta|\sigma I)P(D|\sigma\theta I)}{P(D|\sigma I)}, \tag{3-11}$$

where the prior probability for the phase, $P(\theta|\sigma I)$, represents what is known about the phase before acquiring the data; the direct probability for the data, $P(D|\sigma\theta I)$, is a marginal probability from which the dependence on the amplitudes has been removed, and $P(D|\sigma I)$ is a normalization constant. If this probability density function is normalized at the end of the calculation, one obtains

$$P(\theta|\sigma DI) \propto P(\theta|I)P(D|\theta\sigma I), \tag{3-12}$$

Applying the sum and product rules of the probability theory and omitting constant terms that will cancel upon normalization, the posterior probability can be rewritten as:

$$P(\theta|\sigma DI) \propto P(\theta|I) \int dA P(A|\sigma I)\, P(D|A\theta\sigma I), \tag{3-13}$$

where $P(A|\sigma I)$ is the joint prior probability for the amplitudes. The probability for the data, i.e. the likelihood, given the parameters is represented by $P(D|A\theta\sigma I)$. The prior probability for θ will be assigned a uniform bounded prior:

$$P(\theta|I) = \begin{cases} \frac{1}{2\pi} & if\ 0 \le \theta \le 2\pi \\ 0 & \text{otherwise} \end{cases}, \tag{3-14}$$

The amplitude prior will be assigned as a generalized Gaussian of the form:

$$P(A|\beta\sigma I) \propto \sigma^{-N} exp\left\{-\frac{\beta^2}{2\sigma^2}\sum_{k=1}^{N}\sum_{l=1}^{N} A_k U_{kl} A_l\right\}, \tag{3-15}$$

where the hyperparameter, β, part of *I*, expresses how strongly this prior information is believed, and the matrix, U_{kl} specifies how the amplitudes are related to each other. The derivations of the estimated amplitudes and the posterior probabilities are given in Bretthorst, here we just give the results: the image voxels are given by:

$$\sum_{l=1}^{N} V_{kl}\hat{A}_l = d_{Rk}\cos\theta + d_{Ik}\sin\theta, \tag{3-16}$$

where

$$V_{kl} = \delta_{kl} + \beta^2 U_{kl}, \tag{3-17}$$

where δ_{kl} is a Kronecker delta function. Equation (3-16) can be rewritten as:

$$\widehat{A_l} \equiv \hat{a}_i\cos\theta + \hat{b}_i\sin\theta, \tag{3-18}$$

where $\hat{a}_i$ and $\hat{b}_i$ are the coefficients in equation (3-16) multiplying through by the inverse of the V_{kl} matrix. The posterior probability for the phase then has the form of:

$$P(\theta|\sigma DI) \propto exp\left\{\frac{\sqrt{W^2+X^2}\cos(2\theta+\varphi)}{4\sigma^2}\right\}, \tag{3-19}$$

where W, X are given by,

$$W \equiv \sum_{i=1}^{N}\left(\hat{a}_i d_{Ri} - \hat{b}_i d_{Ii}\right), \tag{3-20}$$

$$X \equiv -\sum_{i=1}^{N}\left(\hat{a}_i d_{Ii} + \hat{b}_i d_{Ri}\right), \tag{3-21}$$

and

$$\varphi = \tan^{-1}\frac{X}{W}. \tag{3-22}$$

Talyor expanding Eq. (3-19) around $\theta_{max} = -0.5\theta$, the estimated phase is given by:

$$\widehat{\boldsymbol{\theta}} = \theta_{max} \pm \sqrt{\frac{8\sigma^2}{\sqrt{W^2+X^2}}}. \tag{3-23}$$

Finally, the absorption mode images can be generated according to the following equation:

$$S_{pi} = S_i \exp\left\{-i\widehat{\boldsymbol{\theta}}\right\}, \tag{3-24},$$

where the S_{pi} is the phased signal, S_i is the original signal, and $\hat{\theta}$ is the estimated voxel-wise phase. The phased signals can be projected entirely to the real channel.

Acknowledgements

This study is supported in part by NIH/NINDS R01 - NS047592, R01 - NS054194, and P01- NS 059560. We gratefully thank Dr. Larry Bretthorst for his valuable advice on the data analysis and manuscript, Dr. William Spees for his suggestion and advice on the pulse sequence implementation.

Chapter 4. The impact of Myelination on Axon Sparing and Locomotor Functional Recovery

Abstract

The dysmyelinated axons of shiverer mice exhibit characteristics similar to early postnatal axons before myelination. Except lacking of compact myelin sheath, the patterns of neuronal activity and axonal connectivity are relatively comparable to those of wild-type myelinated axons. Their unique white matter environment is of our interest to study the impact of myelin sheath on functional recovery in response to traumatic spinal cord injury (SCI). We applied in vivo DTI and immunohistochemistry analysis to investigate the role of compact myelin sheath affecting axon integrity and the resultant locomotor function in a time series. The current study to date is the first to document the injury response on shiverer mice. We found that myelin sheath is critical to present in a high level hind limb function. However, when the functional outcome is limited, such as, in the chronic phase after injury, the amount of spared axon plays the role. Our data also support that the DTI biomarkers, axial and radial diffusivities, are capable of noninvasively detecting the axon and myelin integrities in response to the injuries on both myelinated and dysmyelinated white matter environments.

4.1 Introduction

Dysmyelinated shiverer mutants (shi) lack the essential myelin basic protein (MBP) required to form the major dense line of myelin sheath [133]. The compact myelin is absent in shiverer mice when the MBP level is less than 25% of normal [134]. The tremor of shiverer mice starts about 12 days after birth; progresses leading to increased frequency and duration of tonic seizures with age [135]. Shiverer mice have a shorter life

span ranging between 50 and 100 days. Interestingly, shiverer mice exhibit neither axonal degeneration nor inflammation besides dysmyelination [136]. Although shiverer mice exhibit slightly deteriorated axonal conduction, the patterns of neuronal activity and functional connectivity in shiverer mice remain comparable to those of wild-type myelinated axons [137]. Thus, shiverer mice represent a unique model to investigate the effect of myelin sheath on axonal damages after spinal cord injury (SCI).

Diffusion tensor imaging (DTI) measures the diffusion property of water molecules in the living tissues. It has been applied to assess the integrity of white matter tracts in rodent models of SCI [20, 33, 34, 36, 58, 62, 138]. The extent of axon and myelin damages has been estimated noninvasively using the DTI derived axial ($\lambda_{\parallel}$, describing water diffusion along fiber tracts) and radial diffusivity ($\lambda_{\perp}$, describing water diffusion across the fiber tract) respectively where decreased $\lambda_{\parallel}$ was associated with axonal injury and increased $\lambda_{\perp}$ reflected myelin damages [33, 83, 84, 139, 140]. These DTI derived biomarkers have successfully assessed axon and myelin integrities in both myelinated and dysmylinated white matters [83, 141-143].

The objective of this study is to examine the effect of dysmyelination on the in vivo DTI biomarkers of the white matter injury and to investigate its impact on locomotor function during the course of SCI. The extent of spared axon and myelin sheath after contusion SCI was assessed longitudinally using in vivo DTI followed by the end-point histology on dysmyelinated shiverer mice and the heterozygous littermates. Both DTI and histological findings were correlated with their locomotor function assessed using Basso mouse scale (BMS). Results suggest that myelin sheath is critical to maintain the higher hind limb function performance before SCI. At the chronic phase of SCI where significant myelin loss was severe, the hind limb function was primarily correlated with the extent of spared axons.

4.2 Materials and Methods

All surgical preparations and pre- and postsurgical cares were provided in accordance with Public Health Service Policy on Humane Care and Use of Laboratory Animals and Guide for the Care and Use of Laboratory Animals (Institute of Laboratory Animal Resources, National Research Council, 1996), and with the approval of the Washington University Animal Studies Committee.

Animals and Spinal Cord Injury

Adult (8 to10-week-old) female shiverer mice (shi-/-), and their heterozygous littermates (shi +/-) were used in this study. Spinal cord injury and sham operation were performed on both shiverer and heterozygous mice (N = 6, each group). The injury groups of mice were anesthetized with an isoflurane/oxygen mixture and received severe contusion SCI (displacement: 1.1mm, velocity: 0.2m/s) utilizing a modified Ohio State University (OSU) impacter after dorsal laminectomy at the T9 vertebral level. All mice showed complete paralysis with no ankle movement after injury. The sham-operated animals underwent a laminectomy without contusion and served as the control. The surgical site was closed in layers with 4-0 vicryl and nylon sutures. Injections of enrofloxacin (2.5 mg/kg) and lactated ringers (1.5 ml) were given subcutaneously. Manual bladder expression of the injured mice was performed twice daily throughout the duration of the study ([9]. Softened rodent chow was provided. Body weights were measured and compared daily with the preoperative weight. High-calorie nutrient paste (Nutrical; Evsco, Inc., Buena, NJ) was given to the mice to maintain body weights at 90% of their preoperative values. Daily BMS scoring was performed on all mice from 1 to 21 days post injury (DPI).

in vivo DTI

An MRI-compatible device was utilized to stabilize the vertebral column as reported previously [32]. Mice were anesthetized with an isoflurane/oxygen mixture (4.5 – 5% for induction and 0.7 – 1.5% for maintenance) to be placed in the MRI scanner. Core body temperatures were maintained at 37°C with a circulating warm-water pad. The inhalant anesthetic was delivered to the mice through a custom-made nose cone. The respiratory exhaust line was connected to a pressure transducer to synchronize DTI data collection with the respiratory rate. An inductively coupled surface receiver coil covering vertebral segments T6 – T12 (15 mm × 8 mm) was used as the receiver. A 9-cm (inner diameter) Helmholtz coil was employed as the RF transmitter. The entire preparation was placed in a 4.7 T magnet (Oxford Instruments plc, Abingdon, UK) equipped with a 15-cm (inner diameter) actively shielded Magnex gradient coil (60 G/cm, 270 μs rise time). The magnet, gradient coil, and IEC gradient power supply were interfaced with a Varian DirectDrive console (Varian, Inc., Palo Alto, CA).

In vivo DTI were conducted on all mice at five time-points: naïve, hyperacute (~3hrs), sub-acute (7 DPI), sub-chronic (14 DPI), and chronic (21 DPI) phases. A spin-echo sequence, modified by adding Stejskal–Tanner diffusion-weighting gradient [99], was used with the following parameters: echo time (TE) = 38 ms, diffusion gradient interval (Δ) = 18 ms, diffusion gradient time (δ) = 6 ms, diffusion gradient amplitude = 8.5 G/cm, b value = 1.02 ms/μm^2, six diffusion-sensitizing gradients: (Gx,Gy,Gz) = (1,1,0), (1,0,1), (0,1,1), (-1,1,0), (0,-1,1), and (1,0,-1), number of averages = 4, field of view (FOV) = 1 × 1 cm, and data matrix = 128 × 128 (zero-filled to 256 × 256). The repetition time (TR ≈ 1.2s) was varied according to the period of the respiratory cycle (≈270 ms). Nine transverse images (slice thickness = 0.75 mm) were collected covering vertebral segments T8 – T10. The acquisition time was approximately 2.5 hrs. Three eigenvalues

(λ1, λ2, λ3) were calculated from the diffusion tensor matrix by least square regression. The eigenvalue-derived parameters including mean diffusivity (MD), Trace (Tr), axial diffusivity ($\lambda_{||}$), radial diffusivity ($\lambda_{\perp}$), and relative anisotropy (RA) were calculated as previously reported. All parameters were derived from diffusion-weighted images using software written in Matlab (MathWorks, Natick, MA).

Region of Interest Analyses

Previous literatures have reported that the $\lambda_{||}$ may be used to determine the integrity of axons allowing the assessment of the area of spared axons (A_{SA}) non-invasively [34, 36, 58]. Clear contrast between the GM and VLWM was seen in the $\lambda_{||}$ maps of both heterozygous and shiverer spinal cords (Fig. 4-2). The distribution of $\lambda_{||}$ in both GM and VLWM were obtained from five sham-operated control animals of each group for a histogram analysis. The mean and standard deviation (SD) were determined and a threshold (mean ± 2 × SD) was used to define the A_{SA} in the injured cords (Fig. 4-2). A_{SA} of injured cords were then normalized to the total spinal cord area and total VLWM area of the control cords to remove the atrophy effect for comparing between groups and with the gold-standard histology. The RA maps show the extent of spared VLWMs accounting for both axonal and myelin integrity allowing the region of interest (ROI) determination of group averaged DTI biomarkers. Statistical analysis was performed by one-way ANOVA comparing shiverer and heterozygous mice with $p < 0.05$ regarded as statistically significant. Data were expressed as mean ± standard deviation (SD).

Behavioral Assessment of Hindlimb Locomotor Function

The mouse hind limb locomotor function was assessed daily using BMS over the 21-day recovery period [31] by two raters scoring from 0 (worst) to 9 (best) with a sub-

score tally from 0 (worst) to 11 (best) to evaluate angle movement, plantar placement, stepping, coordination, paw position, trunk instability, and tail position.

Immunohistochemistry Analysis

Immediately after imaging at 21DPI, mice were perfusion fixed under deep anesthesia with 50 mL of 0.1 M phosphate-buffered saline (PBS) (pH 7.4) followed by 200 mL of 0.1 M PBS containing 4% paraformaldehyde (pH 7.4). Following fixation, the spine was excised, left in the fixative overnight, decalcified for 48h, embedded in paraffin, and sectioned on a sliding microtome (5 μm) with the decalcified vertebral column intact. Tissues were stained for Erithryna cristagalli/Crystal Violet (EC/CV) for myelin/neuron survival, myelin basic protein (MBP) for the myelin integrity, and phosphorylated neurofilament protein (SMI31) for spared axon. Tissue was then mounted for microscopic inspection after completion of differentiation. Stained sections at the injury epicenter were digitally imaged using a Nikon Eclipse 80i microscope (Nikon Corporation, Tokyo, Japan) equipped with a 4× objective, and the images were captured with a Photometrics CCD digital camera using MetaMorph image acquisition software (Universal Imaging Corporation, Downington, PA). All images were captured within 1 week following completion of histological staining. The spared axon area was normalized to the total cord size area and total VLWM area of the control cords on account of atrophic effect and shrinkage during fixation. All slides were assessed blindly with respect to the injury.

4.3 Results

Due to the profound tremors, the naïve shiverer mice exhibited impaired hind limb function with consistent plantar stepping, some to most coordination, and rotated paws

at initial contact and lift off (BMS = 6). The naïve heterozygous controls showed normal hind limb function (BMS = 9) (Fig. 4-1). Severe contusion injury resulted in complete paralysis (BMS = 0) on both heterozygous and shiverer mice. Both groups of animals showed similar hind limb function deficits throughout the time course after SCI. Though a slightly faster recovery and better hindlimb function was seen in shiverer mice, the difference was not significant.

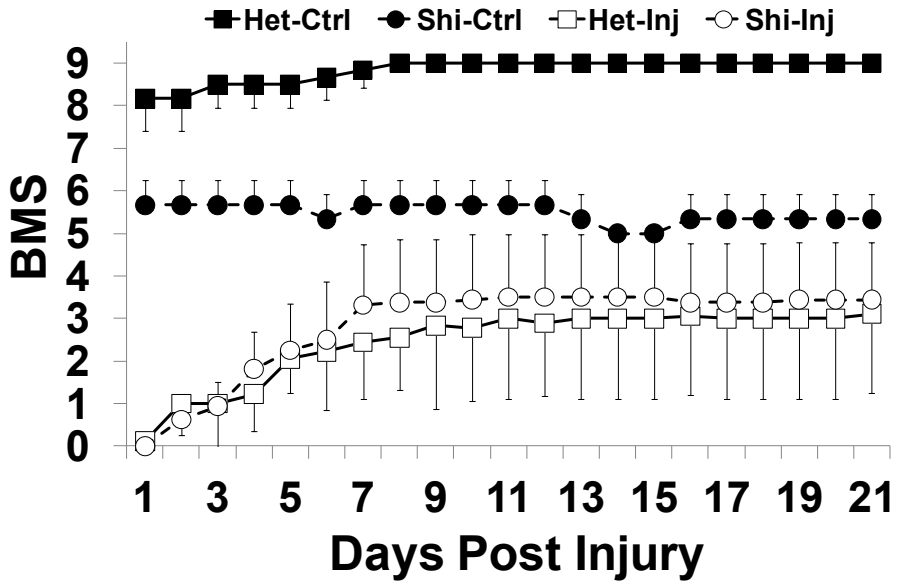

Figure 4-1. The control shiverer and heterozygous mice behave differently in hind limb function. The naïve heterozygous controls showed normal hind limb function, and the naïve shiverer had impaired hind limb function with severe tremor affecting their locomotor function. After contusion SCI, both shiverer and heterzygous mice showed a significant decrease of hind limb motor function and recovery in the sub-acute phase (7~9 DPI). The BMS scores, however, did not show significant difference between the injured shiverer and heterzygous mice. N=6 in each group.

The $\lambda_{||}$ map provided clear GM to WM contrast in both heterozygous and shiverer mice enabling the segmentation of normal appearing from the injured axons (Fig. 4-2). The $\lambda_{||}$ threshold allowed determining the extent of spared axons longitudinally after SCI.

Longitudinal T2W images show the spinal cord and hemorrhages areas to confirm the location of injury epicenter (Fig. 4-3). The $\lambda_{\perp}$ maps clearly revealed the difference in myelination between the heterozygous (Fig. 4-3a) and shiverer mice (Fig. 4-3b). Contrast in RA maps exhibited the GM to WM contrast resulting from the combined effect of axon and myelin sparing after injury.

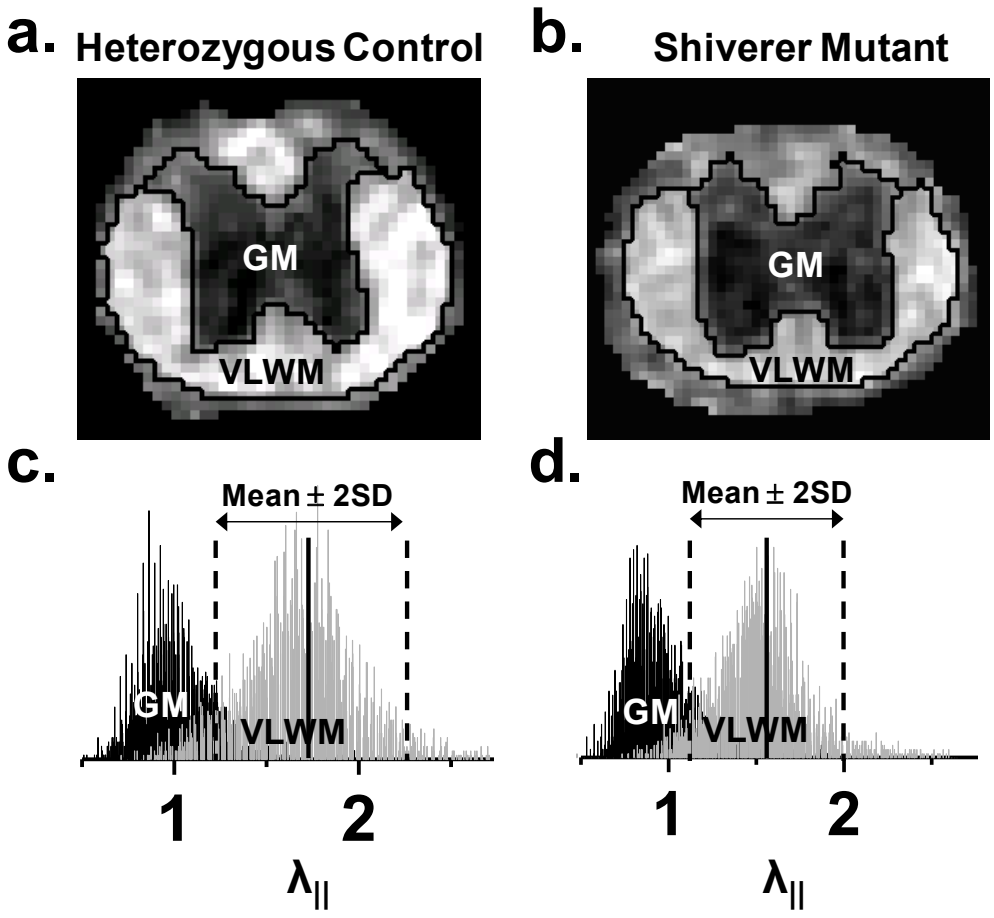

Figure 4-2. $\lambda_{||}$ maps show clear tissue contrast both in heterozygous and shiverer spinal cords (a, b). Two normal distributions are seen in manually defined GM and VLWM allowing segmentation of the spared VLWM (c, d). Smaller mean and standard deviation in $\lambda_{||}$ are observed in shiverer VLWM. The mean±2SD of $\lambda_{||}$ is used as threshold to define the region of normal-appearing VLWM in the control and injured spinal cords of shiverer and heterozygous mice.

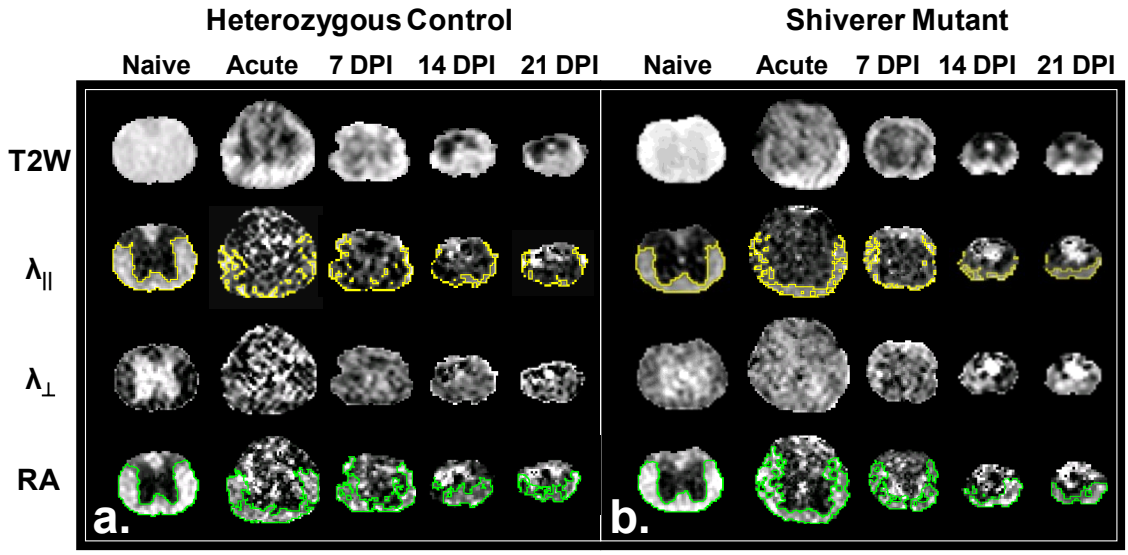

Figure 4-3. Longitudinal DTI maps of the contusion injured spinal cords of heterozygous (a) and shiverer (b) mice. Originally, the heterozygous cords show clear tissue contrast between GM and VLWM in $\lambda_{||}$, $\lambda_{\perp}$ and RA maps. Comparing to the heterozygous spinal cord, the shiverer spinal cord shows lower tissue contrast originated from the dysmelinated VLWM that increases $\lambda_{\perp}$ and decreases $\lambda_{||}$, and RA. The contrast is not clear in the $\lambda_{\perp}$ map. After contusion SCI, T1W images show profound hemorrhage and tissue swelling in the acute phase, and tissue shrinkage in the secondary injury phases. Spared axons along the injury progress are clearly demonstrated in the $\lambda_{||}$ maps (delineated in yellow ROIs). The myelin integrity shown in $\lambda_{\perp}$ maps indicates that heterozygous cords experience extensive demylination, while the tissue contrast in the shiverer cords is not apparent throughout the injury progress. The RA maps show the effects of both axonal injury and demyelination allowing determining the total VLWM area along the injury (delineated in green ROIs).

Significant differences in the total cord area were observed between heterozygous and shiverer mice at 7 and 21DPI (Fig. 4-4a). Except naïve cords, no significant difference was seen in areas of the spared axons between heterozygous and shiverer mice (Fig. 4-4b). The area of spared axons normalized to the total cord area exhibited no significant differences between the heterozygous and shiverer mice throughout the time course of the study (Fig. 4-4c). When normalized to the area of VLWM, the more

significant atrophic change was seen in both strains of mice (Fig. 4-4d). The heterozygous mice showed a more rapid decrease of spared axon area normalized to VLWM than that of the shiverer mice. There were no statistically significant differences in normalized areas of spared axons between the two strains of mice from 7 DPI through the end of the time course.

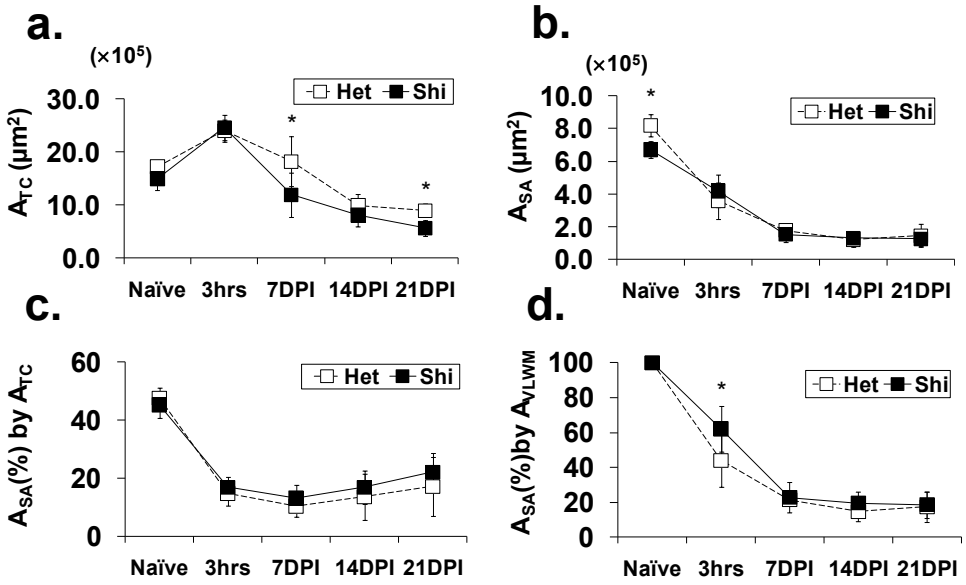

Figure 4-4. Evolution of total cord size area (A_{TC}) (a), spared axon area (A_{SA}) (b), percent spared axon proportion to total VLWM (c), and percent spare axon proportion to total cord size area. The cord sizes are similar between the shiverer and non-shiverer mice before and immediately after SCI. Both groups suffered severe whole cord atrophy, severer in shiverer than heterpzygous mice (a). The shiverer mice have smaller VLWM initially. After SCI, however, both groups show similar amounts of spared VLWM area (b). When taking into account of atrophy effect of the A_{TC}, the percent spared VLWM is no difference between heterozygous and shiverer mice throughout the injury progress (c). The difference patterns of VLWM degeneration become obvious when taking into account the VLWM atrophy only. The heterozygous shows drastic decrease of the percent spared VLWM areas immediately after SCI, while the shiverer preserves more spared VLWM. But shiverer mice experience more secondary degeneration in the sub-acute phase (7DPI) than the heterozygous, so that the percent spared VLWM areas become the same in the chronic phase (d). (* $p<0.05$)

Prior to SCI, the $\lambda_{||}$ was lower in naïve shiverer than that of the heterozygous mice (Fig. 4-5a). After SCI, the time course of $\lambda_{||}$ did not statistically differ between heterozygous and shiverer mice (Fig. 4-5a) exhibiting the most significant decrease at 3 hrs after injury, statistically indistinguishable from the lowest value at 7 days after injury. At baseline, the VLWM $\lambda_{\perp}$ of shiverer mice was 0.4 ± 0.07 $\mu m^2/ms$, significantly higher than that of the heterozygous mice ($0.2 \pm 0.03x$ $\mu m^2/ms$) (Fig. 4-5b). After SCI, the VLWM $\lambda_{\perp}$ in shiverer mice remained unchanged up to 14 DPI. In contrast, the VLWM $\lambda_{\perp}$ of heterozygous mice increased but not exceeding the baseline value of shiverer mice from 3 hrs after injury up to 14 DPI. Both shiverer and heterozygous VLWM $\lambda_{\perp}$ increased above the baseline shiverer mice value at 21 DPI. The diffusion anisotropy of VLWM from heterozygous mice was higher than that of the shiverer mice at the baseline. After injury, the differential reduced becoming equal from 7DPI until the end of the time course at 21 DPI (Fig. 4-5c).

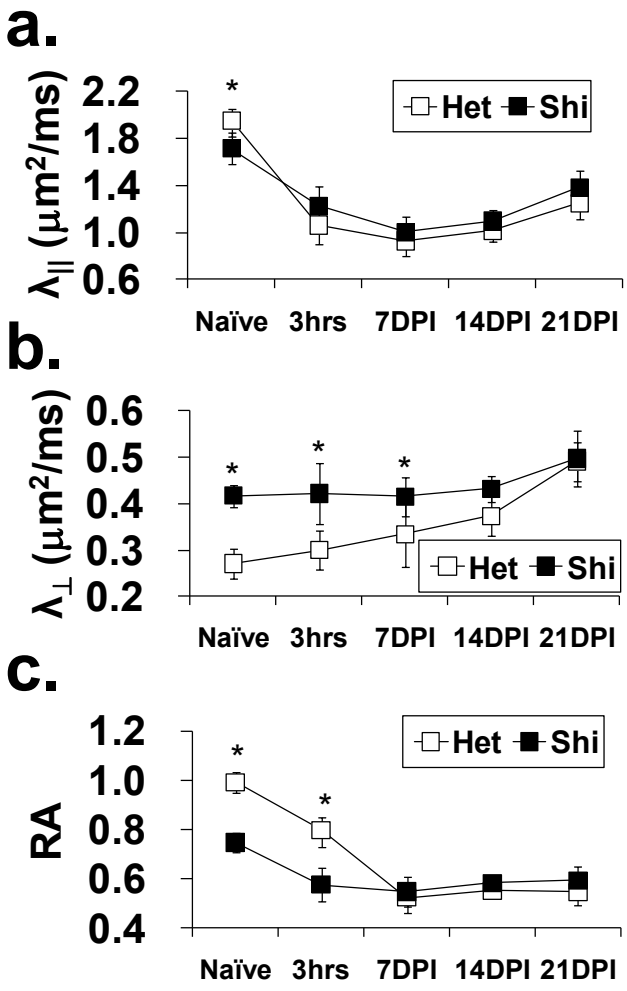

Figure 4-5. Group averaged $\lambda_{||}$ (a), $\lambda_{\perp}$ (b) and RA (c) in the SWM at each injury phase. The $\lambda_{||}$ is lower in naïve shiverer mice. After SCI, the $\lambda_{||}$ show no significant difference between heterzygous and shiverer mice. Originally, the $\lambda_{\perp}$ of the shiverer mice is 1.5 folds of that of heterzygous mice. The $\lambda_{\perp}$ of the shiverer mice does not change throughout the injury progress, indicating no demyelination occurred. Meanwhile, the $\lambda_{\perp}$ of the heterzygous mice shows continuous increase suggesting severe demyelination in the myelinated VLWM. Two groups of mice show the same $\lambda_{\perp}$ in the chronics phase. Significant difference of RAs is seen between two groups of mice. The VLWM of the shiverer mice has smaller axon, more microstructures, and incomplete myelin sheath that are reflecting on the smaller RA. The RAs change insensitively due to the slow process of demyelination. After 7DPI, there is no significant difference between heterozygous and shiverer mice. (* $p<0.05$)

The BMS score of shiverer mice was 6 before SCI, a significantly worse function than the heterozygous mice (Fig. 4-1). After 21 DPI, the BMS of shiverer and heterozygous mice was below 6 and indistinguishable between the two groups of mice (Fig. 4-6a). It is also worth noting that $\lambda_{\perp}$ of shiverer and heterozygous mice were also comparable and larger than the control values of the shiverer mice before injury (Fig. 4-6a). The area of axon sparing revealed that near 100% of axons in both shiverer and heterozygous mice were normal (Fig. 4-6b). The BMS data suggested that the extent of axon sparing played a critical role in the hindlimb function after SCI.

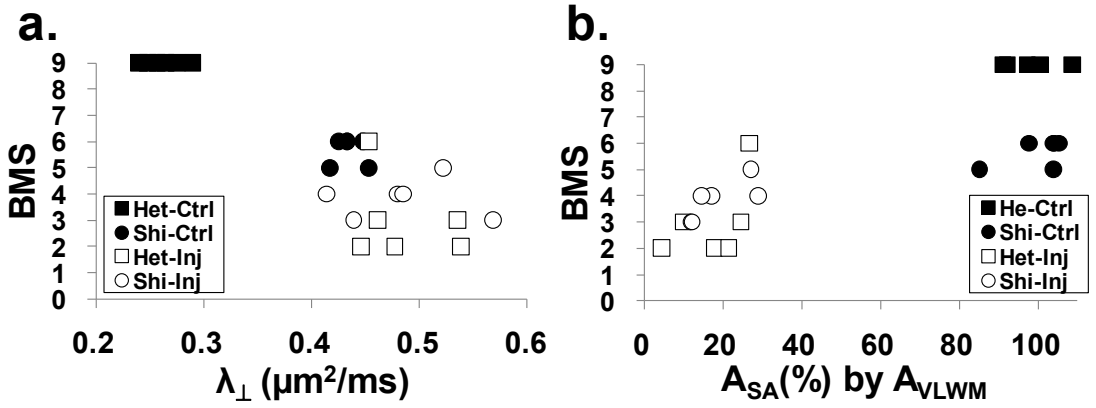

Figure 4-6. Correlation plots between BMS vs $\lambda_{\perp}$ (a), and BMS vs A_{SA}% by A_{VLWM} (b) at 21DPI. The heterzygous control mice show significantly low $\lambda_{\perp}$ than the other groups of mice. Both shiverer and heterozygous control mice show similar amount of A_{SA}% by A_{VLWM}, but their BMS scores are significantly different. A positive correlation between BMS vs A_{SA}% by A_{VLWM} is found in the injured group of mice when their hindlimb function is limited below BMS=6.

Histological analyses of myelin/neuron integrity of control and injured cords from both groups of mice were performed using EC/CV staining respectively (Fig. 4-7a-h). The area of the total cord area was comparable in control shiverer and heterozygous mice. After injury, shiverer mice endured more severe atrophy than that of the heterozygous mice (Fig. 4-7i). The VLWM of the control shiverer mice was significantly

smaller than that of the heterozygous mice (Fig. 4-7j). After injury, significant atrophy of VLWM was seen in both groups of mice (Fig. 4-7j). The VLWM area normalized to the total cord area was not changed in heterozygous mice after injury, while significant decrease in normalized VLWM area was seen in the shiverer mice (Fig. 4-7k). Lesions in shiverer mice occupied a larger proportion of A_{TC} than that in heterozygous (Fig. 4-7l). Normal MBP staining was seen in heterozygous mice (Fig. 4-8a, e, i) while shiverer mice exhibited negative MBP staining (Fig. 4-8c, g, i). At 21 DPI, heterozygous mice showed significant loss of MBP staining intensity indicating severe myelin loss (Fig. 4-8b, f, i). The shiverer mice cords remained MBP negative at 21 DPI (Fig. 4-8d, h, j). Control cords of both shiverer and heterzygous showed comparable amount of SMI-31 staining (Fig. 4-9a, c). The axonal caliber was larger in heterozygous cord (Fig 4-9e, g). SMI-31 staining was largely lost at 21 DPI in both groups (Fig. 4-9b, d), suggesting severe axonal loss (Fig. 4-9f, h). After corrected for tissue shrinkage, ~40% loss of SMI-31 positive area was seen in both groups (Fig. 4-10i, j).

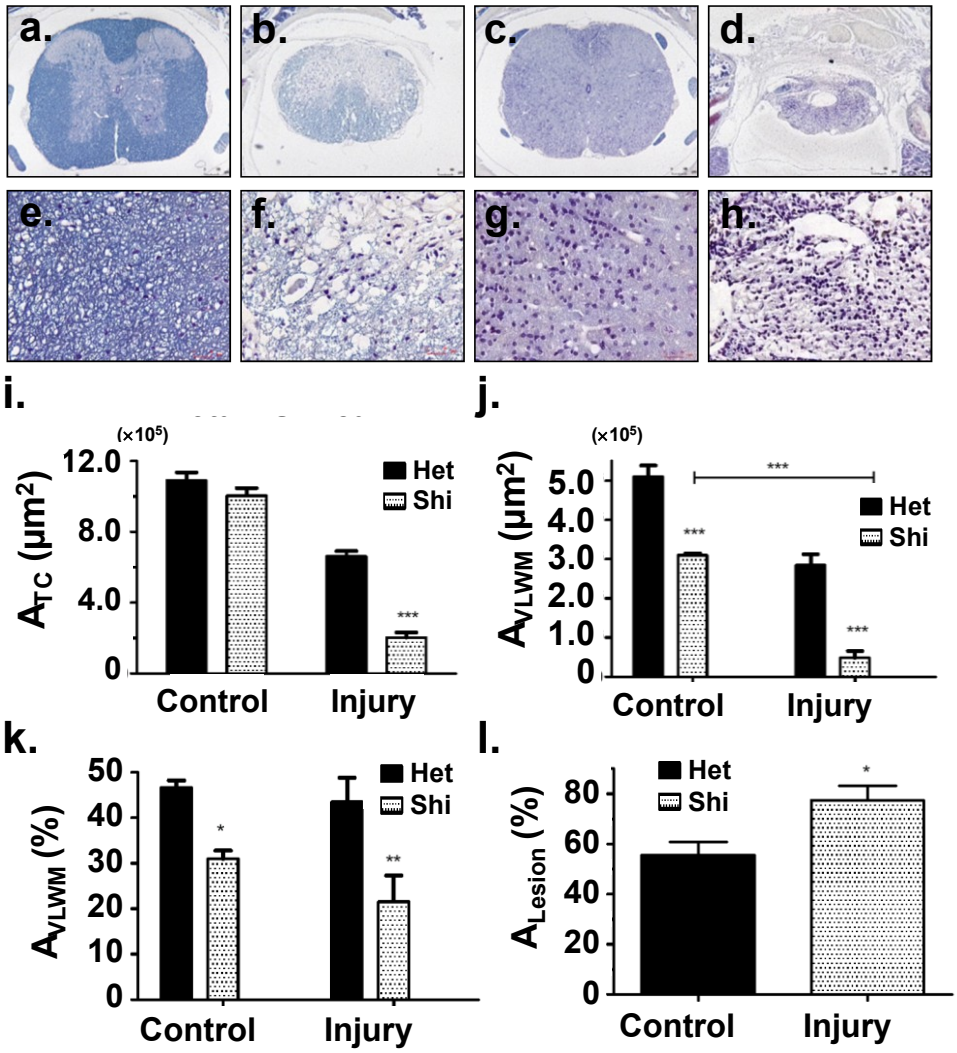

Figure 4-7. EC/CV stain for myelin/neuron survival of heterozygous control (a, e), heterozygous injury (b, f), shiverer control (c, g), and shiverer injury (d, h). The total cord size areas of two control groups are comparable. The injured cord of shiverer mice endure significantly more atrophy than that of heterozygous (i). The VLWM areas of the control shiverer mice is significantly smaller than that of the heterozygous and further shrink more after injury (j). On account of the atrophy of the initial A_{TC}, two groups of injured cords show similar percent VLWM area (k). Lesions in shiverer mice occupy a larger proportion of CS areas than that in heterozygous after corrected for shrinkage (l).

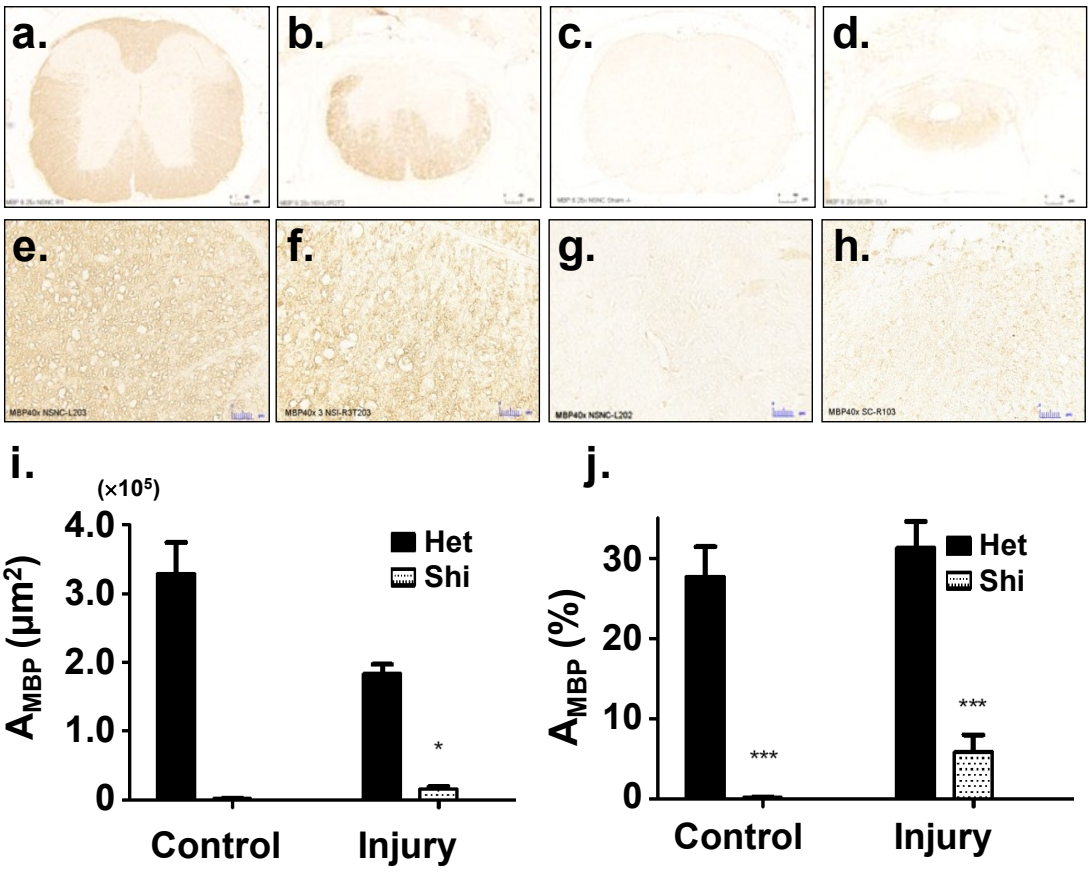

Figure 4-8. MBP stain for myelin basic protein in heterozygous control (a, e), heterozygous injury (b, f), shiverer control (c, g), and shiverer injury (d, h). Heterozygous mice show normal for MBP stain (a, e, i). Shiverer mice congenitally lack of MBP and show almost no positive stain for MBP (c, g, i). At the chronic stage of SCI, heterozygous mice show significant loss of stain intensity indicating severe demylination (b, f, i). The stain intensity does not change between the shiverer control and injured cords (d, h, j).

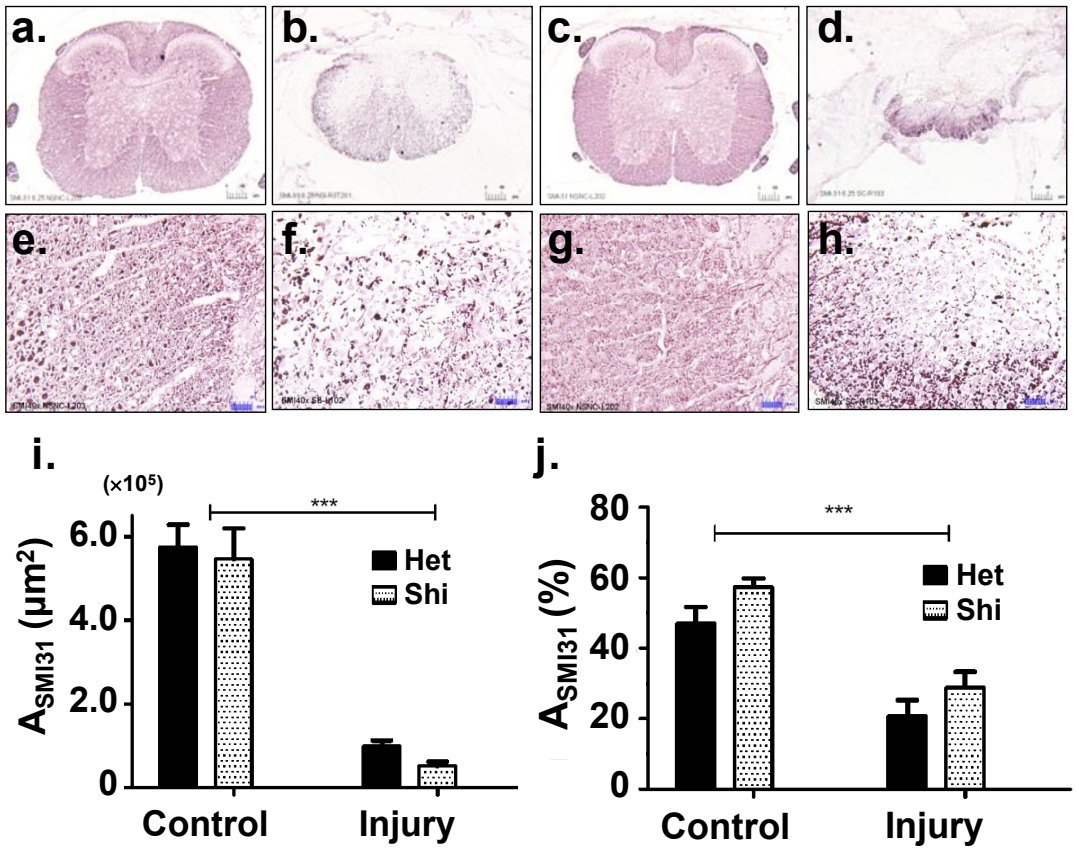

Figure 4-9. SMI31 stain for phosphorylated neurofilament protein in heterozygous control (a, e), heterozygous injury (b, f), shiverer control (c, g), and shiverer injury (d, h). Control cords of both shiverer and heterzygous show comparable amount of SMI31 stains in the low power images. The heterozygous cord, however, has larger axon caliber (e, g). SMI31 stains are greatly lost after injury in both groups, suggesting severe axonal loss in the chronic phase (i). After corrected for shrinkage, the percent SMI31 areas show a ~40% loss in both groups. SMI31 stain in the heterozygous is lost more than that in the shiverer without significance (j).

4.4 Discussion

Without compact myelin, the dysmyelinated axons exhibit decreased axonal caliber, increased cytoskeletal densities, reduced slow axonal transport rates, reduced neurofilament phosphorylation, increased mitocondria stability, irregular axoglial

junctions and scattered distribution of axonal K+ channel in shiverer mice [137, 144-146]. As a result, deteriorated axonal conduction is seen in shiverer spinal cord as evidenced by decreased amplitude, increased latency and decreased conduction velocity [147]. The deficient myelin sheath was also evidenced by the increased $\lambda_{\perp}$ compared to the myelinated controls [83, 142]. The dysmyelinated axons showed lower $\lambda_{||}$ contributing from more axon counts, smaller axon calibers, more microstructures (e.g. mitochondria, microtubule, and neurofilament) and less extracellular space [137, 144-147].

In a traumatic event, axons and glia suffer direct mechanical injury. The ensuing secondary injury leads to the necrotic and apoptotic death of neurons. The myelinating oligodendrocytes partly contribute to the glutamatergic excitotoxicity, free radical damage, and inflammation [148-151]. On the other hand, myelin sheath provides a protection of axon from the excessive glutamate activity [152, 153] and the essential neurotrophin for neuron survival [136, 154, 155]. In the present study, dysmyelinated shiverer and normally myelinated heterozygous mcie were examined to investigate the effect of myelination on axonal integrity after SCI. Both heterozygous and shiverer mice underwent the identical degree of contusion injury resulting in comparable acute axonal damage indicated by the decreased $\lambda_{||}$. Interestingly, the peak severity of axonal injury was reached immediately after contusion suggesting that the primary damage to the axon resulted from the direct mechanical insult. The secondary axonal degeneration progressed slowly over time leading to significant axonal loss 21 DPI as seen in postmortem histology. The slow secondary degeneration was also evident by the gradual elevation of $\lambda_{\perp}$ reflecting the slow myelin loss after axonal damage. The pattern of the injury to myelinated and dysmyelinated VLWM in response to contusion SCI suggested that dysmyelinated axons in shiverer mice suffered lesser, although not statistically significant, primary injury than the myelinated axons after the mechanical

insult. However, faster secondary axonal degeneration is seen in the dysmyelinated axon in the later time points indicating that compact myelin may be required to support the axonal survival from the detrimental secondary degeneration.

Through the serial in vivo DTI, the noninvasive detections of white matter injury allow direct correlation of white matter damage with the animal's locomotor function. In the hyper-acute to sub-acute phase, BMS scoring did not show a significant difference between the two groups due to the effects of spinal shock and profound inflammation. In the chronic phase when the inflammation receded, the DTI and histology results suggested that the spared axons of the heterozygous and shiverer mice were comparable as well as the resultant locomotor function. In our previous study of graded contusion SCI [34], we demonstrated that the locomotor function nearly linearly correlated to the area when spared white matter area was below 50% of the baseline. The locomotor function was not affected if the spared white matter area was above 50% of the baseline. In the current study, we further demonstrated that the area of spared axons correlated with the hindlimb locomotor function at 21 DPI in both shiverer and heterozygous mice with BMS less than 6 (Fig. 6a, b). However, full myelination is required for high locomotor function, i.e., BMS > 6, in mice.

Axonal loss is the primary reason for atrophy in the white matter diseases [156, 157]. However, the heterozygous and shiverer mice showed different atrophic patterns in response to the same contusion SCI. In the first place after the primary mechanical injury, the spinal cords of the heterozygous and shiverer mice swelled to the similar size (Fig. 4a), but more axon was injured in the heterozygous VLWM due to stress accumulation at node of Ranvier in their myelinated axon [11]. As indicated by $\lambda_{||}$ in the acute phase (Fig. 5a), a rapid decrease was seen in the injured heterozygous VLWM and lesser axon was spared (Fig. 4d). Secondly in the sub-acute phase, compared to the mild atrophy of the heterozygous mice, the shiverer cord exhibited more severe

atrophy in this period with mild shrinkage afterward suggesting that severe axonal loss in the this phase. Finally in the chronic phase, the heterozygous mice cord size was larger with comparable amount of axons spared as that in shiverer mice. These injury patterns were consistent with previous literature reports indicating that the dysmyelinated axon was more vulnerable to the secondary degeneration [153, 158]. Although the responses to the injury were in different timing, when the injury degrees were the same, both heterozygous and shiverer cords eventually concluded to the same injury degree.

Myelin sheath provides neurotrophin for neuron protection and also inhibitor against neuron regeneration. In the current experiment shiverer mice did not show severe tremors after injury. It seems that the reaction of dysmyelinated white matter to SCI eased the unstable synaptic connectivity in shiverer mice. In chronic phase, the shiverer mice preserved more spared axon, though not significantly, suggesting that the myelin deficiency may benefit the axon preservation or the axonal regeneration. The underlying mechanism for the better recovery in shiverer mice is unknown. One speculation may be that the dysmyelinated axon acts like an immature axon in which the tubulin protein is elevated to increase the density of axonal microtubules [137]. In addition, the mitochondrial activity is also elevated in the dysmyelinated axon to provide more energy in maintaining conduction [144]. These alterations in response to the absence of myelin, plus less myelin inhibitors presented in shiverer VLWM may somehow facilitate the axon regeneration. On the contrary, the lack of myelin is also not sufficient to keep those regenerated axon healthy and may end up with immature axonal cytoskeleton. Besides the abundant of literatures that use shiverer mice to study the interaction of myelination and axon maturation [137, 145], myelination interacting with axonal structure and conduction [144, 147], distribution and expression of the K+ channel subunits Kv1.l and Kv1.2 [159, 160] and remyelination therapy [146], it is

worthwhile to conduct further studies using shiverer mice to elucidate the insufficiency of less protection, and the conjectural sufficiency of better regeneration.

4.5 Conclusion

The role of spared axon and myelin integrity in locomotor function was investigated by in vivo DTI on dysmyelinated shiverer mice and their heterozygous controls littlermates. Since the shiverer mice have neither axonal injury nor inflammation, the lower hind limb function may be mainly ascribed to the deficient myelin sheath as evidenced by the higher $\lambda_{\perp}$ and lesser MBP staining with relatively normal $\lambda_{||}$ and SMI31 staining. After severe SCI, however, the hind limb locomotor function became no difference between the heterozygous and shiverer mice. Although in the chronic phase, there is still certain amount of myelin sheath in the heterozygous VLWM, the contribution of such impaired myelin sheath to the locomotor function was not obvious. We found that myelin sheath is critical for a higher hind limb function. When the locomotor function is limited, such as the chronic phase after SCI, the amount of spared axon plays the role.

Chapter 5. Vascular and Axonal Injuries in Contusion SCI

Abstract

In contusion SCI, vascular disruption has been observed proximally and distally resulting in intra-parenchymal hemorrhage to exacerbate the secondary injury. Scarce evidence has been reported to explain such injury patterns. In present study, in vivo diffusion- and T2*-weighted MRI, combined with FE biomechanical simulations, provide evidence that explains the causes of concomitant proximal and distal vascular injury with focal axonal injury. Our study indicates that the unexpected, distally-dominated, vascular injury could significantly affect the characteristics of the injury animal model via hemorrhage-induced secondary injury. Structures, such as nerve roots, narrower rostral area, and the size of laminectomy may contribute to the stress accumulation. Injury severity should be carefully characterized first, using, for example, in vivo MRI, to provide a consistent and reproducible platform on trials of preclinical therapeutic intervention.

5.1 Introduction

Rodent model of SCI has been used widely to study the pathophysiological changes and the herein therapeutic intervention [10]. Therapy in the acute phase is directed toward preventing the progression of these changes and confining the injury to the region that was directly traumatized [9]. However, models of cord injury have been limited by inability to precisely control the injury patterns and the evolution of pathologic changes in a given anima [10]l.

In experimental SCI, for instance, the WM injury is usually localized around the traumatic epicenter, while the proximal and distal vascular disruption has been reported in many studies to expand the WM injury in a later time point resulting from the intraparenchymal hemorrhage [9, 60, 150]. The early vascular damage and the resulting edema, necrosis, demyelination, cyst formation, and infarction greatly impact the neurological function after SCI [161]. The uncontrollable factors occurred when generating the experimental SCI by the impact device could eventually affect the consistency of the injury severity in the secondary injury process [8, 11, 105]. The efficacy of the therapeutic intervention therefore may not be able to assess accordingly, and the conclusion is skeptical. Nevertheless, scarce evidence has been reported regarding the origin of concomitant distal vascular disruption on the proximal WM injury.

Finite element analysis (FEA) overcomes the limit of direct measurement to study the biomechanics of SCI [162, 163]. In cooperating with appropriate material properties and boundary conditions, the FEA simulation provides the best mean to elucidate the crucial biomechanical factors of the injury mechanics in the traumatic SCI. On the other hand, Magnetic Resonance (MR) imaging of the central nervous system (CNS) has shown high sensitivity for detecting hemorrhage and yields quality anatomic details [33, 58, 61, 91]. MR imaging also provides a non-invasively method for detecting the pathological changes of SCI in vivo: T2*-weighted MRI is known sensitive for detecting hemorrhage from the susceptibility effect of deoxygenated hemoglobin; the parallel diffusivity is capable for detecting the axonal injury in the hyperacute phase [36, 58]. In the present study, in vivo T2*- and diffusion-weighted MRI, combined with FEA biomechanical simulations, provide strong evidence that explains the causes of concomitant proximal and distal vascular injury with focal axonal injury.

5.2 Materials and Methods

Contusion Spinal Cord Injury

T9-contusion was generated on fourteen to sixteen-week-old YFP C57BL/6 mice weighing 25-29 g by a modified-OSU impacter with at a depth of 0.3mm (mild), 0.5mm (moderate), or 0.8mm (severe) injuries (n = 5 each group). Age and gender matched mice (n = 3) were sham-operated as controls. The profiles of indentation displacement, acceleration, and force were measured in-situ for monitoring the indentation as well as for the FEA model verification. The force profiles were calibrated by the measured force subtracting the inertia force generated from the mass of the impactor tip. The injured animals were imaged hyper-acutely (~3 hrs) to evaluate the patterns of WM and vascular disruption.

MRI

T2*-weighted 3D data sets were acquired usng a gradient-echo sequence. Acquisition parameters were: FOV: 11 × 11 × 11 mm^3, image matrix = 96 × 96 × 96, TR/TE = 12/6 ms, excitation pulse angle = 20°. Image resolution was 114 μm × 114 μm × 114 μm. In vivo diffusion MRI was acquired by two-direction DWI, (Gx,Gy,Gz) = (1,1,0), (0,0,1), using a multiple spin echo diffusion weighted sequence with 45 slices at 94 μm × 94 μm × 200 μm resolution with respiratory gating. Other imaging parameters were: TR/TE= 2000/27 ms, ΔTE 13ms, Δ 15 ms, δ 5 ms; b-value 0 and 1200 s/mm2, FOV 0.9 × 0.9 cm2, data matrix 96 × 96 zero-filled to 192×192, and 3 echoes averaged. The total scan time was ~2 hrs.

The parallel diffusivity was calculated by equation (3-3) to determine the region of axonal injury; the T2*-weighted images were used to assess the extent of hemorrhage.

The 3D injury patterns were outlined by the ROI analysis of threshold hypointensity regions in T2*-weighted and $D_{||}$ maps using the averaged values of the control group.

Finite Element Analysis

The commercial FEA software package, Abaqus, was used to create the FEA model based on in vivo DWI geometry. The anatomical structures of mouse spinal cord from T6 to T11 were distinctly segmented in the in vivo transverse $D_{\perp}$ map (Fig. 5-1a). The DWI maps not only benefit the determination of SCI components for the FEA model generation, but also facilitate the ease of ROI analysis and. Five transverse slices (2.25mm spacing between) were picked for extruding the 3D structure (Fig. 5-1b-d). Comparing to the previous FEA models considering only identical trans-axial sections in the longitudinal direction, the current study reconstructed the actual varied trans-axial sections from T6 to T11 by using in vivo DWI images to generate the FEA model.

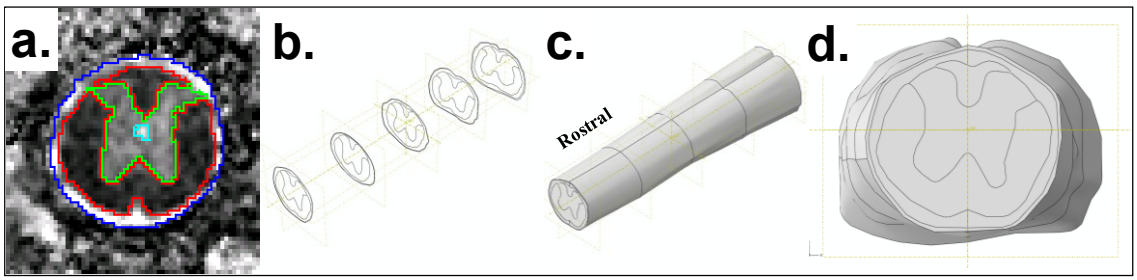

Figure 5-1. Radial diffusivity map clearly demonstrates the structures of in vivo mouse spinal cord. Starting from cerebrospinal fluid, an alternating bright--dark-bright pattern was observed.

Three parts of the contusion SCI components were generated in the model, including the impactor tip of rigid body, vertebrae using tetrahedron mesh, and spinal cord using hexahedron mesh (Fig. 5-2a, b, c). Distinct element sets were meshed to represent vertebrae, dura matter, CSF, pia matter, GM, DWM and VLWM (Fig. 5-2d).

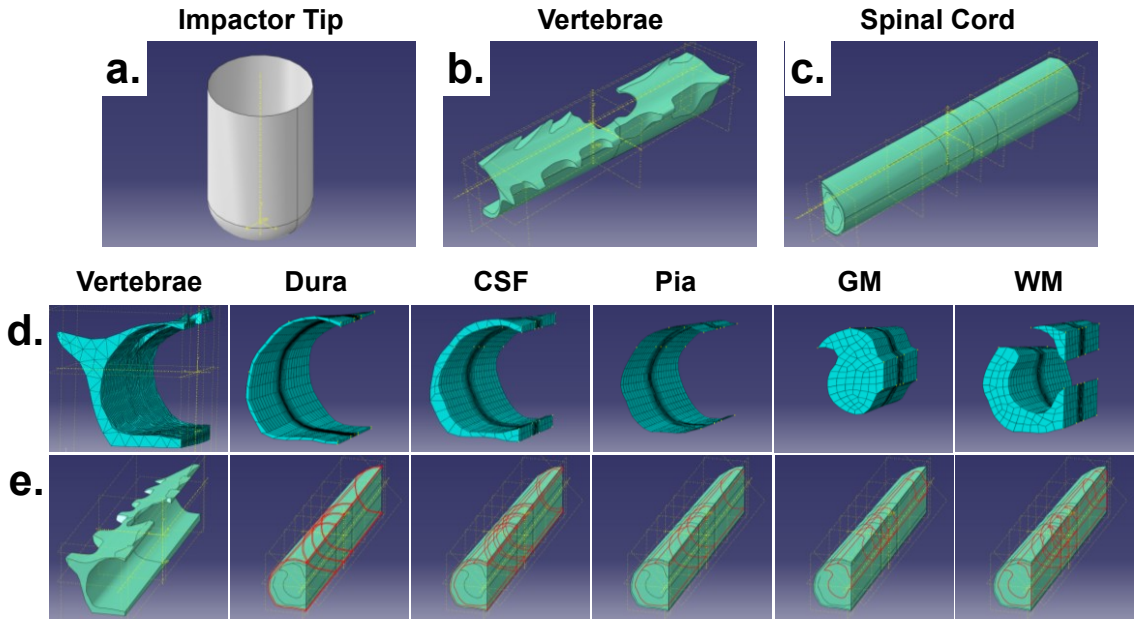

Figure 5-2. Three parts of element are generated in the FEA model (a-c). Six distinct element sets are composed to represent the six fundamental components in the mouse spinal cord.

Constitution Model, Material Properties and Boundary Condition

The Ogden hyperelastic model was used to calculate the biomechanical behavior of spinal cord tissue, which has previously been used to model both spinal cord and brain tissue [23, 164-166]. The Ogden hyperelastic strain energy density function, *U*, is defined by:

$$U = \sum_{i=1}^{N} \frac{2\mu_i}{\alpha_i^2}\left(\bar{\lambda}_1^{\alpha_i} + \bar{\lambda}_2^{\alpha_i} + \bar{\lambda}_3^{\alpha_i} - 3\right) + \sum_{i=1}^{N} \frac{1}{D_i}\left(J^{el} - 1\right)^{2i} \quad (5\text{-}1)$$

, where $\bar{\lambda_\iota}$ are the deviatoric principal stretches$\bar{\lambda_\iota} = J^{-1/3}\lambda_i$; λ_i are the principal stretches; *N* is complexity of the material law; μ_i, α_i and D_i are temperature-dependent material parameters; J^{el} is the elastic volume ratio between current and reference configurations. The initial shear modulus, μ_0, and bulk modulus, K_0, for the Odgen form are given by:

$$\mu_0 = \sum_{i=1}^{N} \mu_i, \quad K_0 = \frac{2}{D_1}, \quad D_1 = \frac{3(1-2\nu)}{\mu(1+\nu)} \tag{5-2}$$

, where μ is equivalent to shear modulus when *N*=1, ν is Poisson's ratio. The viscoelastic portion described with a Prony series exponential decay is defined by:

$$\mu_R(t) = \mu_0 \left[1 - \sum_{k=1}^{N} g_k\left(1 - e^{-t/\tau_k}\right)\right] \tag{5-3}$$

, where the instantaneous shear modulus is multiplied by a normalized function that includes relative relaxations, g_k, at characteristic time constant, τ_k.

The CSF were modeled with solid element with low shear-to-bulk modulus to introduce fluid-like beahavior, [167] using a Mooney-Rivlin hyperelastic model with a 300 times lesser shear modulus than the spinal cord [23]. The Mooney-Rivlin hyperelastic model is defined by:

$$U = C_{10}(\bar{I}_1 - 3) + C_{01}(\bar{I}_2 - 3) + \frac{1}{D_1}(J^{el} - 1)^2, \tag{5-4}$$

where $C_{10} = C_{01}$ in this model are temperature-dependent material parameters; $\bar{I}_1$ and $\bar{I}_2$ are the first and second deviatoric strain invariants defined as:

$$\bar{I}_1 = \bar{\lambda}_1^2 + \bar{\lambda}_2^2 + \bar{\lambda}_3^2 \text{ and } \bar{I}_2 = \bar{\lambda}_1^{(-2)} + \bar{\lambda}_2^{(-2)} + \bar{\lambda}_3^{(-2)}, \tag{5-5}$$

The initial shear modulus is given by:

$$\mu_0 = 2(C_{10} + C_{01})$$ (5-6)

,

The impact tip was set as rigid body, and the vertebrae were applied as elastic material. Material properties applied in literatures were first applied in the calculation, and fine-tuned to fit the in-situ force measurements as listed in Table 5-1. The boundary conditions used previously in the literature were adapted

Table 5-1. The material properties adapted from the literature are applied in the FEA model.

Tissue	Hyperelasticity		Viscoelasticity			Ref.
	Model	Model Constants	Viscoelasticity Law	Constant	Relaxation Time	
Spinal Cord	Ogden (N=1)	G_∞=15 kPa α=4.7 v=0.45 d=1050 kg/m^3	Three-term Prony series decay	G_1=163.2 kPa G_2=35.3 kPa G_3=12.1 kPa	τ_1=1 msec τ_2=10 msec τ_3=100 msec	**Maikos (2008)**
Dura	Ogden (N=1)	G_∞=1205 kPa α=16.2 v=0.45 d=1000 kg/m^3	Four-term Prony series decay	G_1=1069 kPa G_2=416 kPa G_3=335 kPa G_4=335 kPa	τ_1=9 msec τ_2=81 msec τ_3=564 msec τ_4=4690 msec	
CSF	Mooney-Rivlin	G=0.134 kPa C01=C10=0.0335 kPa d=1000 kg/m^3	Not considered			
Bone	Linear Elastic	G= 2.5×10^6 kPa d=1360 kg/m^3	Not considered			**Persson (2010)**
Pia	Linear Elastic	G= 793 kPa d=1040 kg/m^3	Not considered			**Ozawa (2004)**

The spinal column is assumed to be an encastre rigid body providing friction to the spinal cord. The coefficient of friction between spinal cord and spinal column was 0.6; between spinal cord and impact tip was 0.15. The impact was placed in direct contact with the exposed dura and prescribed the in-situ displacement profiles of 0.8mm, 05mm and 0.3mm penetrating into the spinal cord with the speed of 0.2m/s. The model was symmetric at the sagittal midlines of the spinal cord and vertebrae to save computational cost.

Convergence Test and Model Validation

The convergence test was first conducted to determine the most efficient and accurate mesh for further calculation. Once the best mesh had been determined, the models ran with material properties of the literatures to compare with in-situ force profiles. The material properties of the spinal cord were then adjusted accordingly to fall within 95% confidence interval of the in-situ force profiles. The whole model has 19,422 nodes and 22,590 elements.

5.3 Results

Three injury severities at mild (0.3 mm), moderate (0.5 mm), and severe (0.8mm) were generated (Fig. 5-3a). Distinct force profiles of the indentation were seen in three injury groups showing highly viscoelastic properties of the spinal cord tissue (Fig. 5-3b). Compared to the sham-operated controls, all three injury groups displayed obvious WM injuries in the parallel diffusivity maps and vascular disruptions in the T2*W images (Fig.5-4). All WM injury patterns distributed evenly from the injury epicenter to the distal regions. However, the hemorrhage pattern distributes differently between three injury groups (Fig. 5-5). The Mild injured group exhibited only local hemorrhage and WM injury at the epicenter. The moderately injured group exhibited vascular and WM injury patterns coexisting in the epicenter and significant rostral WM injury with less prominent but noticeable rostral vascular damage. The severe group displayed a prominent focal hemorrhage and WM damage both in the epicenter and rostral regions. Both hemorrhage and axonal injury extended more in the rostral than caudal direction.

The convergence test of the FEA model shows that the seeding size 0.007 could be the best mesh design considering both efficiency and accuracy (Fig. 5-6). The model

chosen for further calculation contained 19,422 nodes and 22,590 elements .The validation curves show good match between the FEA model force estimations and the in-situ force measurements (Fig. 5-7).

In the simulation, the initial indentation produced a focal stress and stretch in the epicenter resulting proximal hemorrhage and axonal injury (5-8b, c, d). During the indentation, the strain rate propagated from the epicenter, heavily extending to the rostral direction, consistent with the more severe rostral hemorrhage away from the epicenter. The stress and stretch was confined focally at the epicenter resulting in the even injury distribution. The primary mechanical factor to cause the vascular disruption may be the strain rate. The FEA results confirmed the MRI injury pattern of distal hemorrhage increasing with injury severities. On the other hand, the axonal injury is mainly strain related. The axonal injuries identified in $D_{||}$ maps correspond to the focally centered but evenly spreading von Mises stress and MPS.

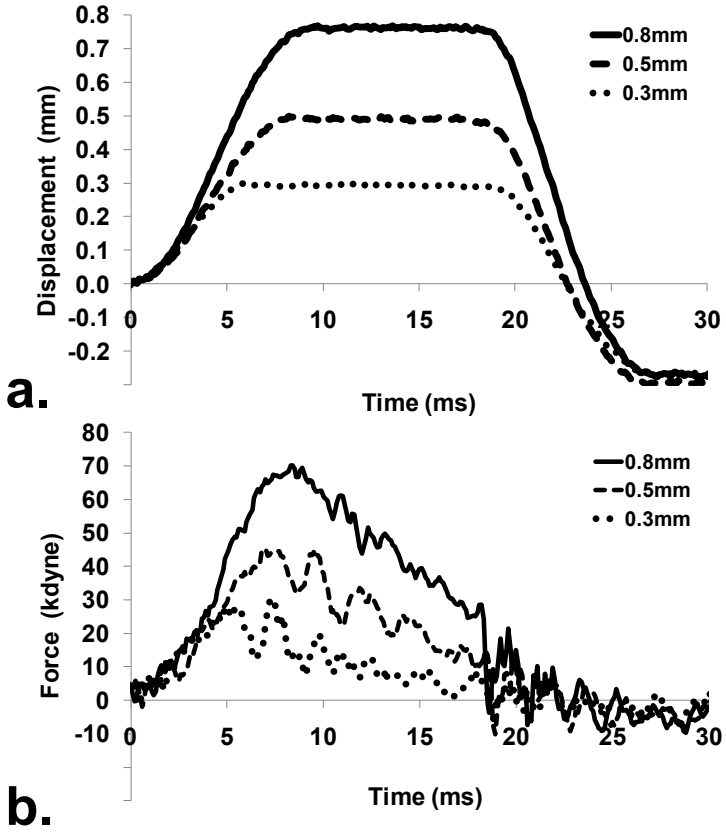

Figure 5-3. The averaged profiles of indentation displacement and force measured in-situ when the spinal cords injured (n=5 each group). Mild (0.3mm), moderate (0.5), and severe (0.8mm) injuries generates three distinguishable profiles of displacements and forces.

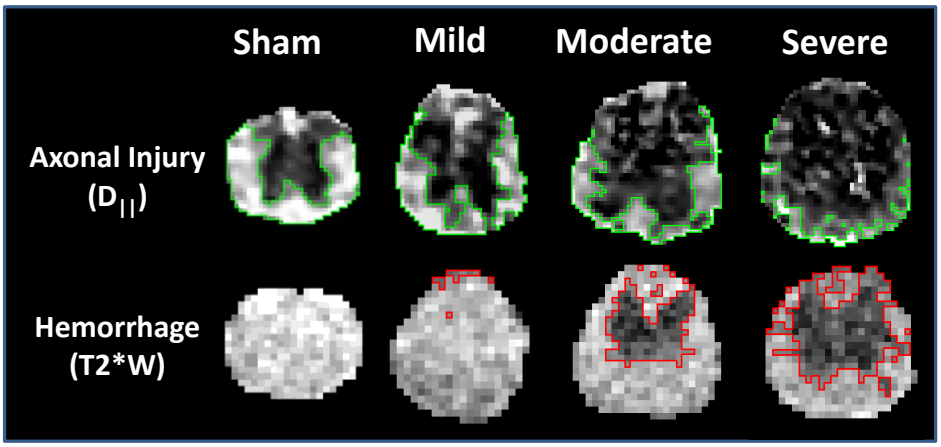

Figure 5-4. The transverse views of the parallel diffusivity map and T2* images show the axonal injury and hemorrhage patterns of sham, mild, moderate, and severe injury groups. The regions of spared axon are encompassed in the ROIs in green in the $D_{||}$ map. The hemorrhage regions are delineated by the ROIs in red in the T2* weighted images.

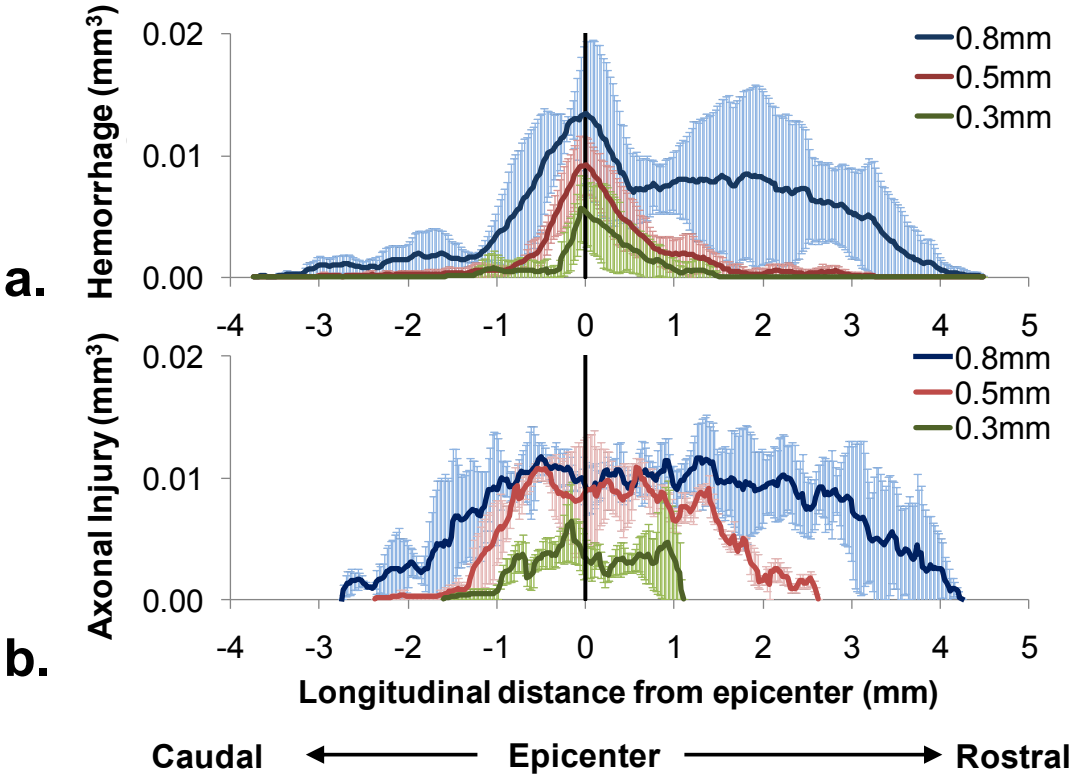

Figure 5-5. Longitudinal projections of the lesion volumes show different patterns in (a) hemorrhage and (b) WM injury. Averaged data are shown with standard deviation (n=3).

The severity of the epicenter vascular injury correlated with the severity of impact. In addition to the epecenter pattern, a distinct distal vascular injury is apparent at 2 mm rostral to the epicenter in the moderate and severe injury cords. In contrast, the WM injuries extend uniformly throughout the injury region with further extension rostrally.

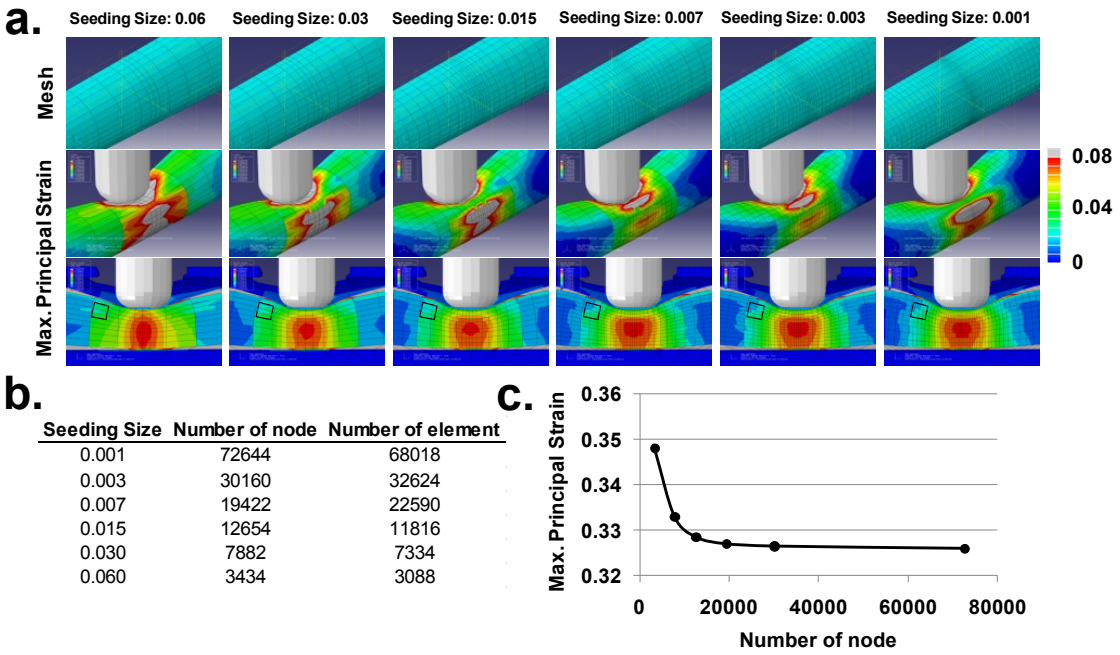

Seeding Size	Number of node	Number of element
0.001	72644	68018
0.003	30160	32624
0.007	19422	22590
0.015	12654	11816
0.030	7882	7334
0.060	3434	3088

Figure 5-6. Results of the convergence test. Meshes and the contour maps of the maximum principal strain (MPS) are plotted in (a). Seeding sizes, number of node and element contained in each mesh (b). The MPS in the convergence test is plotted versus the number of node in Abaqus (c). The data is getting from the region indicated in each contour map. The less the seeding size in a model, the finer the mesh is. The MPS converges at seeding size 0.007.

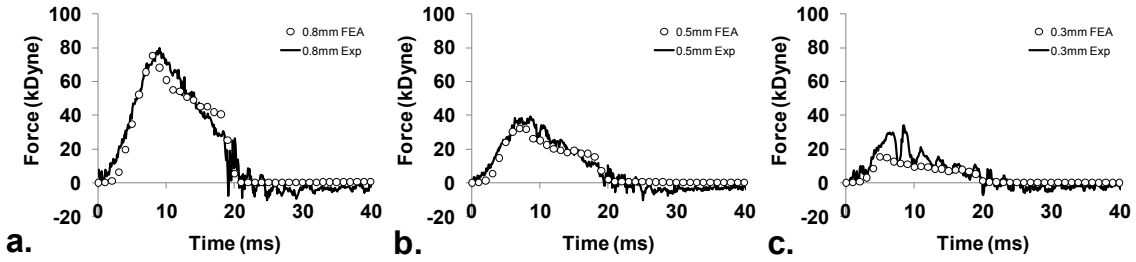

Figure 5-7. The force validation curves are plotted between the in-situ measurements and FEA results in the groups of 0.8mm (a), 0.5mm (b), and 0.3mm (c).

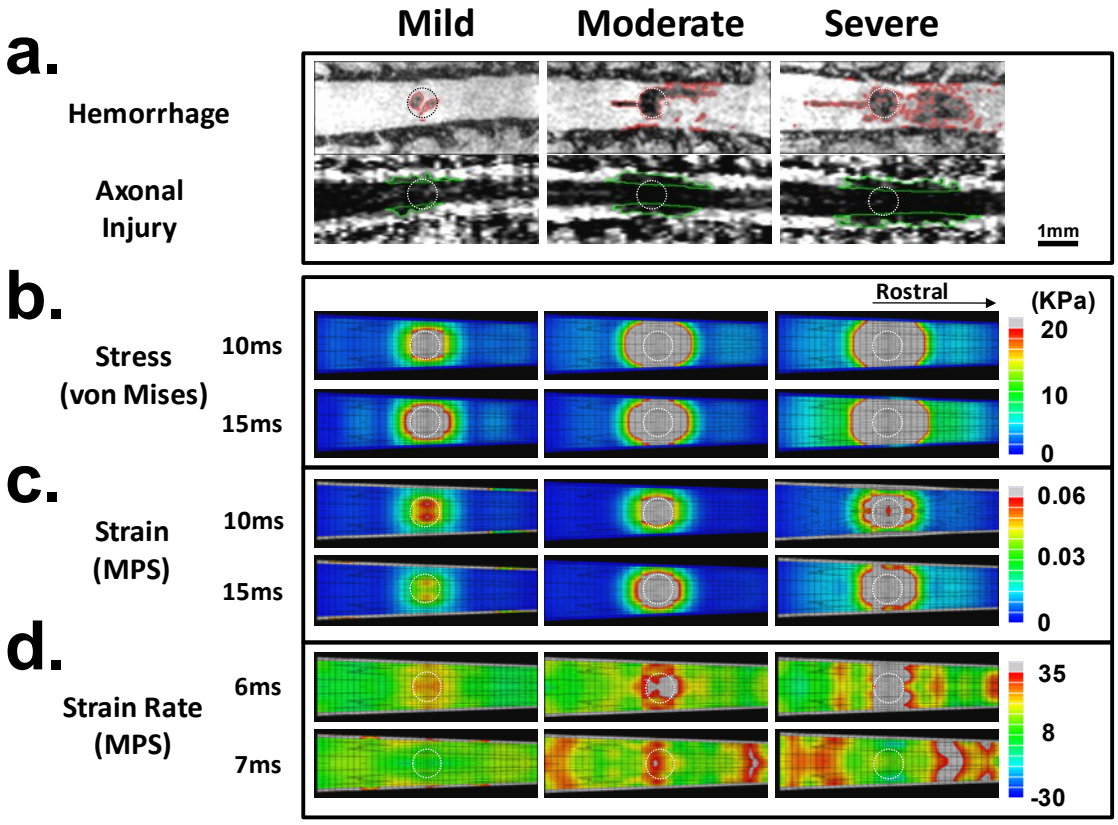

Figure 5-8. Comparison of coronal T2*W images, $D_{||}$ maps and FEA stress, strain, and strain rate contour maps on three injury degrees. Hemorrhage areas are outlined in red in T2*W images and the axonal injury is outlined in green in $D_{||}$ maps (a). The dashed circles indicate the injury epicenter. The von Mises stress and MPS distributions at 10 ms and 15 ms after impact show localized at the epicenter and slightly extend to the rostral sites (b, c). The MPS strain rate shows accumulated at the epicenter at 6ms, however, the strain rate extends to the distal site, especially to the rostral site, at 7ms (d).

5.4 Discussions

The neural and vascular injury patterns in the epicenter and distal sites were first examined by diffusion- and T2*- weighted images. The acute vascular and WM damage extended more significantly rostrally, and the injury patterns show increasing distal damage with increasing injury severity. These acute injury patterns correspond to our FEA simulation results suggesting that the vascular disruption is caused by the strain rate accumulation and propagation while the axon damage is more related to the evenly spreading strain field.

The possible reasons for causing concomitant proximal and distal injury, especially toward the rostral side, may mainly originate from the spine structures, such as narrower rostral area and nerve root locations [8, 9]. The CSF, occupying the subarachnoid space between the arachnoid mater and the pia mater, acts a cushion or buffer for spinal cord. The spinal cord essentially floats inside the vertebrae to prevent the basic mechanical insult [25]. In the rodent spinal cord, the narrowest segment of the spinal cord is at T2~T3, where the largest size of cord is at T12~L1, the lumbar enlargement. The CSF space at the narrower region is also much thinner and not able to provide enough degree of freedom allowing absorbing the impact. In our simulation study, the stress and strain tend to accumulate at the narrower rostral section. The effects are clearly seen in the in vivo MR images with more axonal injury and hemorrhage extending to the rostral side

Another important factor has not been considered in the FEA model is the anchoring effect of the nerve roots. In the dorsal region, the spinal nerve roots emerge from the dorsal horn through an opening intervertebral foramen between adjacent vertebrae [12, 19]. The denticulate ligaments, the attachment to the arachnoid and dura

mater, provide stability for the spinal cord against motion within the vertebral column. The spinal cord indentation causes the denticulate ligaments to present a stress on the spinal cord, and cause more damage near the dorsal root. The segments of the T7/T8 regions rostral to the epicenter are much shorter than the segments of the T10/T11 such that the nerve roots are more closely distributed in the rostral region contributing to the stronger anchoring effect. Though, it is believed that the nerve roots are particularly susceptible to be injured, due to the lack of protective epineurium and perineurium to aid in absorbing large tensile and compressive forces making the effect of nerve root ambiguous in the experimental SCI. Even without considering the anchoring effect, our MR imaging and FEA simulation still show strong evidence that the distal injury is apparent and could be an important issue in controlling the injury severity in the experimental SCI.

It is noticeable that in our experiments, the force profile of the spinal cord indentation shows highly viscoelastic behavior that the force rapidly dissipated 40kdyne in 10ms (Fig. 5-3b). This fast stress relaxation property measured from the lateral indentation is somewhat different from what has been reported in the previous indentation experiment [9]. Besides the behavior of the material properties itself, we speculate that the reason of the fast stress relaxation may come from the fluid-solid interaction within the spinal cord, since the in vivo spinal cord is full of interstitial fluid and soaked in the CSF. The movement of these fluids within the spinal cord may induce a time difference expelling the CSF and the interstitial fluid away from the epicenter when the impact is given fast. The effect of this biphasic fluid-solid interaction may also affect the stress and strain distribution within the spinal cord [168]. Further investigation is needed to elucidate and characterize the actual cause and effect of the fast relaxation property.

Our FEA simulation showed that the WM is more sensitive to the strain, which spreads widely along the longitudinal direction. However, the vascular disruption is more related to the propagating strain rate distribution. Another possible explanation for the distal vascular injury pattern may come from the stress and stain rate induced excessive pressure in micro-vascular leading to the Blood Spinal Cord Barrier breakdown or the direct burst of micro vessels, since the endothelial wall of the blood vessel is known to be able to sustain large stretch without injury [41]. On the other hand, the fiber-like axon structure is known sensitive to the longitudinal deformation that is related to the strain distribution. Thus, any alteration during the surgical procedure, such as the size of laminectomy, and the impact location, which eventually leads to the change of stress and strain distribution of the impact may be responsible to the inconsistency of the injury model. A more accurate assessment of the injury severity may be achieved using in vivo MRI acutely to reduce inter-animal variation on trials of preclinical therapeutic intervention.

Chapter 6. Conclusions and Future Work

SCI is the most devastating injury that often causes the victim permanent paralysis and undergo a lifetime of therapy and care. There are 11,000 people across the country that suffers from these types of injuries every year. Over 200,000 people are living with these serious debilitating injuries. The medical expenses associated with SCI are huge, costing victims a hundred of thousands of dollars a year.

Lots of researches from various fields are devoted to investigate the effective diagnosis and therapy for the traumatic injury by using animal model of the traumatic SCI. The research in this dissertation covers a wide range of SCI studies from studying MR imaging, neuropathology, and biomechanics. We apply the knowledge and technique of every discipline to accomplish the complex SCI studies, and also connect the multidisciplinary perspectives for providing thought to deal with the difficulties in the pathophysiological system. We improve the efficiency of spinal cord imaging, validate the imaging biomarkers in the dysmyelinating WM for detecting axonal injury and myelin damage, and elucidate the biomechanical factors to cause inconsistent mouse model of contusion injury. The contribution of our works to the neurotrauma society is to provide efficient and accurate in vivo detection of spinal cord WM injury, as well as to understand the injury biomechanics in the animal model of contusion SCI.

In the future, the direction of our imaging research should focus on providing imaging biomarkers in reflecting the various stages of SCI, such as inflammation in the sub-acute phase, mitochondria activation in the sub-chronic phase, and neuronal conductivity in the chronic phase. Also, in cooperating with in vivo MR imaging methods detecting various detail information of the contusion SCI, the FEA model could potentially be used to determine the material properties by correlating the mechanical

parameters (from FEA) and the injury pattern (from in vivo MRI). Combining the advantage of FEA and diffusion MRI, the biomechanical properties could be more accurately determined non-invasively. The relationship between these mechanical property distributions and specific injury severity and pattern plays the crucial role to facilitate developing the simulation of neurosurgery and spine-related protection gear and intervention.

Reference

1. Encyclopædia-Britannica, *spinal cord.* 2008, Encyclopædia Britannica Online.
2. Kandel, E.R., *Principles of Neural Science 4/e*. 2000: McGraw-Hill.
3. Benavente, A., et al., *Assessment of disability in spinal cord injury.* Disabil Rehabil, 2003. **25**(18): p. 1065-70.
4. McLlvoy, L., K. Meyer, and T. Vitaz, *Use of an acute spinal cord injury clinical pathway.* Crit Care Nurs Clin North Am, 2000. **12**(4): p. 521-30.
5. DeVivo, M.J., *Causes and costs of spinal cord injury in the United States.* Spinal Cord, 1997. **35**(12): p. 809-13.
6. Valsamis, M.P., *Pathology of trauma.* Neurosurg Clin N Am, 1994. **5**(1): p. 175-83.
7. Kuhn, W., et al., *Comparison of spinal cord injuries in females and in males, 1979-1981 Basle.* Paraplegia, 1983. **21**(3): p. 154-60.
8. Basso, D.M., M.S. Beattie, and J.C. Bresnahan, *Graded histological and locomotor outcomes after spinal cord contusion using the NYU weight-drop device versus transection.* Exp Neurol, 1996. **139**(2): p. 244-56.
9. Jakeman, L.B., et al., *Traumatic spinal cord injury produced by controlled contusion in mouse.* J Neurotrauma, 2000. **17**(4): p. 299-319.
10. Young, W., *Spinal cord contusion models.* Prog Brain Res, 2002. **137**: p. 231-55.
11. Blight, A., *Mechanical factors in experimental spinal cord injury.* J Am Paraplegia Soc, 1988. **11**(2): p. 26-34.
12. Maxwell, W.L., *Histopathological changes at central nodes of Ranvier after stretch-injury.* Microsc Res Tech, 1996. **34**(6): p. 522-35.
13. Shi, R. and J. Whitebone, *Conduction deficits and membrane disruption of spinal cord axons as a function of magnitude and rate of strain.* J Neurophysiol, 2006. **95**(6): p. 3384-90.
14. Young, W., J. Kume-Kick, and S. Constantini, *Glucocorticoid therapy of spinal cord injury.* Ann N Y Acad Sci, 1994. **743**: p. 241-63; discussion 263-5.
15. Constantini, S. and W. Young, *The effects of methylprednisolone and the ganglioside GM1 on acute spinal cord injury in rats.* J Neurosurg, 1994. **80**(1): p. 97-111.
16. Gruner, J.A., *A monitored contusion model of spinal cord injury in the rat.* J Neurotrauma, 1992. **9**(2): p. 123-6; discussion 126-8.
17. Stokes, B.T., D.H. Noyes, and D.L. Behrmann, *An electromechanical spinal injury technique with dynamic sensitivity.* J Neurotrauma, 1992. **9**(3): p. 187-95.
18. Stokes, B.T., *Experimental spinal cord injury: a dynamic and verifiable injury device.* J Neurotrauma, 1992. **9**(2): p. 129-31; discussion 131-4.
19. Scheff, S.W., et al., *Experimental modeling of spinal cord injury: characterization of a force-defined injury device.* J Neurotrauma, 2003. **20**(2): p. 179-93.
20. Kim, J.H., et al., *Impact speed does not determine severity of spinal cord injury in mice with fixed impact displacement.* J Neurotrauma, 2009. **26**(8): p. 1395-404.
21. Shi, R. and J.D. Pryor, *Pathological changes of isolated spinal cord axons in response to mechanical stretch.* Neuroscience, 2002. **110**(4): p. 765-77.
22. Shi, R., *The dynamics of axolemmal disruption in guinea pig spinal cord following compression.* J Neurocytol, 2004. **33**(2): p. 203-11.

23. Maikos, J.T., et al., *Finite element analysis of spinal cord injury in the rat.* J Neurotrauma, 2008. **25**(7): p. 795-816.
24. Ichihara, K., et al., *Mechanism of the spinal cord injury and the cervical spondylotic myelopathy: new approach based on the mechanical features of the spinal cord white and gray matter.* J Neurosurg, 2003. **99**(3 Suppl): p. 278-85.
25. Kato, Y., et al., *Biomechanical study of cervical flexion myelopathy using a three-dimensional finite element method.* J Neurosurg Spine, 2008. **8**(5): p. 436-41.
26. Kato, M., et al., *Ependymal cyst in the lumbar spine associated with cauda equina compression.* J Clin Neurosci, 2008. **15**(7): p. 827-30.
27. Scifert, J., et al., *Spinal cord mechanics during flexion and extension of the cervical spine: a finite element study.* Pain Physician, 2002. **5**(4): p. 394-400.
28. Maikos, J.T., R.A. Elias, and D.I. Shreiber, *Mechanical properties of dura mater from the rat brain and spinal cord.* J Neurotrauma, 2008. **25**(1): p. 38-51.
29. LaPlaca, M.C., et al., *CNS injury biomechanics and experimental models.* Prog Brain Res, 2007. **161**: p. 13-26.
30. Ichihara, K., et al., *Gray matter of the bovine cervical spinal cord is mechanically more rigid and fragile than the white matter.* J Neurotrauma, 2001. **18**(3): p. 361-7.
31. Basso, D.M., et al., *Basso Mouse Scale for locomotion detects differences in recovery after spinal cord injury in five common mouse strains.* J Neurotrauma, 2006. **23**(5): p. 635-59.
32. Kim, J.H., et al., *Detecting axon damage in spinal cord from a mouse model of multiple sclerosis.* Neurobiol Dis, 2006. **21**(3): p. 626-32.
33. Kim, J.H., et al., *Noninvasive diffusion tensor imaging of evolving white matter pathology in a mouse model of acute spinal cord injury.* Magn Reson Med, 2007. **58**(2): p. 253-60.
34. Kim, J.H., et al., *Diffusion tensor imaging at 3 hours after traumatic spinal cord injury predicts long-term locomotor recovery.* J Neurotrauma, 2010. **27**(3): p. 587-98.
35. Kim, J.H., et al., *Impact speed does not determine severity of spinal cord injury in mice with fixed impact displacement.* J Neurotrauma, 2009.
36. Tu, T.W., et al., *Full tensor diffusion imaging is not required to assess the white-matter integrity in mouse contusion spinal cord injury.* J Neurotrauma, 2010. **27**(1): p. 253-62.
37. SIMULIA, *Abaqus Analysis User's Manual.* 2007.
38. Ueno, K., et al., *Development of tissue level brain injury criteria by finite element analysis.* J Neurotrauma, 1995. **12**(4): p. 695-706.
39. Greaves, C.Y., M.S. Gadala, and T.R. Oxland, *A three-dimensional finite element model of the cervical spine with spinal cord: an investigation of three injury mechanisms.* Ann Biomed Eng, 2008. **36**(3): p. 396-405.
40. Ouyang, H., et al., *Biomechanics of spinal cord injury: a multimodal investigation using ex vivo guinea pig spinal cord white matter.* J Neurotrauma, 2008. **25**(1): p. 19-29.
41. Galle, B., et al., *Correlations between tissue-level stresses and strains and cellular damage within the guinea pig spinal cord white matter.* J Biomech, 2007. **40**(13): p. 3029-33.

42. Bertram, C.D., L.E. Bilston, and M.A. Stoodley, *Tensile radial stress in the spinal cord related to arachnoiditis or tethering: a numerical model.* Med Biol Eng Comput, 2008. **46**(7): p. 701-7.
43. Dixon, A.K., et al., *Magnetic resonance imaging of the head and spine: effective for the clinician or the patient?* Bmj, 1991. **302**(6768): p. 79-82.
44. Jackson, E.F., et al., *A review of MRI pulse sequences and techniques in neuroimaging.* Surg Neurol, 1997. **47**(2): p. 185-99.
45. Dagia, C. and M. Ditchfield, *3T MRI in paediatrics: Challenges and clinical applications.* Eur J Radiol, 2008.
46. Bartels, U., et al., *Role of spinal MRI in the follow-up of children treated for medulloblastoma.* Cancer, 2006. **107**(6): p. 1340-7.
47. Bams-Mengerink, A.M., et al., *MRI of the brain and cervical spinal cord in rhizomelic chondrodysplasia punctata.* Neurology, 2006. **66**(6): p. 798-803; discussion 789.
48. Hubbard, A.M., *Ultrafast fetal MRI and prenatal diagnosis.* Semin Pediatr Surg, 2003. **12**(3): p. 143-53.
49. Smith, D.S., *Field guide to bedside diagnosis*. 2007: Lippincott Williams & Wilkins.
50. Fritz, J., et al., *Management of chronic low back pain: rationales, principles, and targets of imaging-guided spinal injections.* Radiographics, 2007. **27**(6): p. 1751-71.
51. Lammertse, D., et al., *Neuroimaging in traumatic spinal cord injury: an evidence-based review for clinical practice and research.* J Spinal Cord Med, 2007. **30**(3): p. 205-14.
52. Guillevin, R., et al., *Spine metastasis imaging: review of the literature.* J Neuroradiol, 2007. **34**(5): p. 311-21.
53. Malfair, D. and D.P. Beall, *Imaging the degenerative diseases of the lumbar spine.* Magn Reson Imaging Clin N Am, 2007. **15**(2): p. 221-38, vi.
54. Aoe, H., et al., *Clinical significance of T1-weighted MR images following transient cerebral ischemia.* J Neurol Sci, 2006. **241**(1-2): p. 19-24.
55. Gissel, H., et al., *Magnetic resonance imaging of changes in muscle tissues after membrane trauma.* Ann N Y Acad Sci, 2005. **1066**: p. 272-85.
56. Mattila, K.T., et al., *Magnetic resonance imaging and magnetization transfer in experimental myonecrosis in the rat.* Magn Reson Med, 1995. **33**(2): p. 185-92.
57. van Lookeren Campagne, M., et al., *Secondary reduction in the apparent diffusion coefficient of water, increase in cerebral blood volume, and delayed neuronal death after middle cerebral artery occlusion and early reperfusion in the rat.* J Cereb Blood Flow Metab, 1999. **19**(12): p. 1354-64.
58. Loy, D.N., et al., *Diffusion tensor imaging predicts hyperacute spinal cord injury severity.* J Neurotrauma, 2007. **24**(6): p. 979-90.
59. Knight, R.A., et al., *Magnetic resonance imaging assessment of evolving focal cerebral ischemia. Comparison with histopathology in rats.* Stroke, 1994. **25**(6): p. 1252-61; discussion 1261-2.
60. Fiford, R.J. and L.E. Bilston, *The mechanical properties of rat spinal cord in vitro.* J Biomech, 2005. **38**(7): p. 1509-15.

61. Fraidakis, M., et al., *High-resolution MRI of intact and transected rat spinal cord.* Exp Neurol, 1998. **153**(2): p. 299-312.
62. Deo, A.A., et al., *In vivo serial diffusion tensor imaging of experimental spinal cord injury.* J Neurosci Res, 2006. **83**(5): p. 801-10.
63. E. Mark Haacke, R.W.B., Michael R. Thompson, Ramesh Venkatesan, *Magnetic Resonance Imaging: Physical Principles and Sequence Design*. 1999: Wiley-Liss.
64. Clark, C.A. and D.J. Werring, *Diffusion tensor imaging in spinal cord: methods and applications - a review.* NMR Biomed, 2002. **15**(7-8): p. 578-86.
65. Bammer, R., et al., *Line scan diffusion imaging of the spine.* AJNR Am J Neuroradiol, 2003. **24**(1): p. 5-12.
66. Bammer, R., *Basic principles of diffusion-weighted imaging.* Eur J Radiol, 2003. **45**(3): p. 169-84.
67. Luypaert, R., et al., *Diffusion and perfusion MRI: basic physics.* Eur J Radiol, 2001. **38**(1): p. 19-27.
68. Mori, S. and J. Zhang, *Principles of diffusion tensor imaging and its applications to basic neuroscience research.* Neuron, 2006. **51**(5): p. 527-39.
69. Matt A. Bernstein, Kevin F. King, and Xiaohong Joe Zhou, *Handbook of MRI Pulse Sequences*. 2004: Academic Press.
70. Kingsley, P.B., *Introduction to Diffusion Tensor Imaging Mathematics Part I~III.* Concepts in Magnetic Resonance Part A, 2006. **28A(2)**: p. 101-176.
71. Beaulieu, C., *The basis of anisotropic water diffusion in the nervous system - a technical review.* NMR Biomed, 2002. **15**(7-8): p. 435-55.
72. Frank, L.R., *Anisotropy in high angular resolution diffusion-weighted MRI.* Magn Reson Med, 2001. **45**(6): p. 935-9.
73. Sun, S.W., et al., *Noninvasive detection of cuprizone induced axonal damage and demyelination in the mouse corpus callosum.* Magn Reson Med, 2006. **55**(2): p. 302-8.
74. Song, S.K., et al., *Diffusion tensor imaging detects and differentiates axon and myelin degeneration in mouse optic nerve after retinal ischemia.* Neuroimage, 2003. **20**(3): p. 1714-22.
75. Basser, P.J. and C. Pierpaoli, *A simplified method to measure the diffusion tensor from seven MR images.* Magn Reson Med, 1998. **39**(6): p. 928-34.
76. Basser, P.J. and D.K. Jones, *Diffusion-tensor MRI: theory, experimental design and data analysis - a technical review.* NMR Biomed, 2002. **15**(7-8): p. 456-67.
77. Pierpaoli, C. and P.J. Basser, *Toward a quantitative assessment of diffusion anisotropy.* Magn Reson Med, 1996. **36**(6): p. 893-906.
78. Hoehn-Berlage, M., *Diffusion-weighted NMR imaging: application to experimental focal cerebral ischemia.* NMR Biomed, 1995. **8**(7-8): p. 345-58.
79. Christiansen, P., et al., *Increased water self-diffusion in chronic plaques and in apparently normal white matter in patients with multiple sclerosis.* Acta Neurol Scand, 1993. **87**(3): p. 195-9.
80. Budde, M.D., et al., *Toward accurate diagnosis of white matter pathology using diffusion tensor imaging.* Magn Reson Med, 2007. **57**(4): p. 688-95.
81. Song, A.W., et al., *Functional activation using apparent diffusion coefficient-dependent contrast allows better spatial localization to the neuronal activity:*

evidence using diffusion tensor imaging and fiber tracking. Neuroimage, 2003. **20**(2): p. 955-61.
82. Song, S.K., et al., *Diffusion tensor imaging detects age-dependent white matter changes in a transgenic mouse model with amyloid deposition.* Neurobiol Dis, 2004. **15**(3): p. 640-7.
83. Song, S.K., et al., *Dysmyelination revealed through MRI as increased radial (but unchanged axial) diffusion of water.* Neuroimage, 2002. **17**(3): p. 1429-36.
84. Song, S.K., et al., *Demyelination increases radial diffusivity in corpus callosum of mouse brain.* Neuroimage, 2005. **26**(1): p. 132-40.
85. Sun, S.W., et al., *Evolving Wallerian degeneration after transient retinal ischemia in mice characterized by diffusion tensor imaging.* Neuroimage, 2008. **40**(1): p. 1-10.
86. Sun, S.W., et al., *Selective vulnerability of cerebral white matter in a murine model of multiple sclerosis detected using diffusion tensor imaging.* Neurobiol Dis, 2007. **28**(1): p. 30-8.
87. Inglis, B.A., et al., *Diffusion anisotropy in excised normal rat spinal cord measured by NMR microscopy.* Magn Reson Imaging, 1997. **15**(4): p. 441-50.
88. Nevo, U., et al., *Diffusion anisotropy MRI for quantitative assessment of recovery in injured rat spinal cord.* Magn Reson Med, 2001. **45**(1): p. 1-9.
89. Schwartz, E.D., et al., *Apparent diffusion coefficients in spinal cord transplants and surrounding white matter correlate with degree of axonal dieback after injury in rats.* AJNR Am J Neuroradiol, 2005. **26**(1): p. 7-18.
90. Schwartz, E.D. and D.B. Hackney, *Diffusion-weighted MRI and the evaluation of spinal cord axonal integrity following injury and treatment.* Exp Neurol, 2003. **184**(2): p. 570-89.
91. Ford, J.C., et al., *MRI characterization of diffusion coefficients in a rat spinal cord injury model.* Magn Reson Med, 1994. **31**(5): p. 488-94.
92. Hasan, K.M., D.L. Parker, and A.L. Alexander, *Comparison of gradient encoding schemes for diffusion-tensor MRI.* J Magn Reson Imaging, 2001. **13**(5): p. 769-80.
93. Jones, D.K., *The effect of gradient sampling schemes on measures derived from diffusion tensor MRI: a Monte Carlo study.* Magn Reson Med, 2004. **51**(4): p. 807-15.
94. Jones, D.K., M.A. Horsfield, and A. Simmons, *Optimal strategies for measuring diffusion in anisotropic systems by magnetic resonance imaging.* Magn Reson Med, 1999. **42**(3): p. 515-25.
95. Gulani, V., et al., *A multiple echo pulse sequence for diffusion tensor imaging and its application in excised rat spinal cords.* Magn Reson Med, 1997. **38**(6): p. 868-73.
96. Clark, C.A., D.J. Werring, and D.H. Miller, *Diffusion imaging of the spinal cord in vivo: estimation of the principal diffusivities and application to multiple sclerosis.* Magn Reson Med, 2000. **43**(1): p. 133-8.
97. Kim, T.H., et al., *Diffusion tensor imaging of ex vivo cervical spinal cord specimens: the immediate and long-term effects of fixation on diffusivity.* Anat Rec (Hoboken), 2009. **292**(2): p. 234-41.
98. Gullapalli, J., J. Krejza, and E.D. Schwartz, *In vivo DTI evaluation of white matter tracts in rat spinal cord.* J Magn Reson Imaging, 2006. **24**(1): p. 231-4.

99. Stejskal, E. and J.E. Tanner, *Spin Echoes in the Presence of a Time-Dependent Field Gradient.* J. Chem. Phys., 1965. **42**(1): p. 288-292.
100. Armitage, P.A. and M.E. Bastin, *Selecting an appropriate anisotropy index for displaying diffusion tensor imaging data with improved contrast and sensitivity.* Magn Reson Med, 2000. **44**(1): p. 117-21.
101. Kung, C.C., J.J. Peissig, and M.J. Tarr, *Is region-of-interest overlap comparison a reliable measure of category specificity?* J Cogn Neurosci, 2007. **19**(12): p. 2019-34.
102. Sun, S.W., et al., *Evolving Wallerian degeneration after transient retinal ischemia in mice characterized by diffusion tensor imaging.* Neuroimage, 2008. **40**(1): p. 1-10.
103. Casha, S., W.R. Yu, and M.G. Fehlings, *FAS deficiency reduces apoptosis, spares axons and improves function after spinal cord injury.* Exp Neurol, 2005. **196**(2): p. 390-400.
104. Farooque, M., J. Isaksson, and Y. Olsson, *White matter preservation after spinal cord injury in ICAM-1/P-selectin-deficient mice.* Acta Neuropathol, 2001. **102**(2): p. 132-40.
105. Basso, D.M., *Neuroanatomical substrates of functional recovery after experimental spinal cord injury: implications of basic science research for human spinal cord injury.* Phys Ther, 2000. **80**(8): p. 808-17.
106. Norris, D.G., et al., *On the application of ultra-fast RARE experiments.* Magn Reson Med, 1992. **27**(1): p. 142-64.
107. Chabert, S., et al., *Diffusion tensor imaging of the human optic nerve using a non-CPMG fast spin echo sequence.* J Magn Reson Imaging, 2005. **22**(2): p. 307-10.
108. Le Roux, P., *Non-CPMG Fast Spin Echo with full signal.* J Magn Reson, 2002. **155**(2): p. 278-92.
109. Turner, R., et al., *Echo-planar imaging of intravoxel incoherent motion.* Radiology, 1990. **177**(2): p. 407-14.
110. Bastin, M.E. and P. Le Roux, *On the application of a non-CPMG single-shot fast spin-echo sequence to diffusion tensor MRI of the human brain.* Magn Reson Med, 2002. **48**(1): p. 6-14.
111. Hori, M., et al., *Mean diffusivity, fractional anisotropy maps, and three-dimensional white-matter tractography by diffusion tensor imaging. Comparison between single-shot fast spin-echo and single-shot echo-planar sequences at 1.5 Tesla.* Eur Radiol, 2008. **18**(4): p. 830-4.
112. Sarlls, J.E. and C. Pierpaoli, *Diffusion-weighted radial fast spin-echo for high-resolution diffusion tensor imaging at 3T.* Magn Reson Med, 2008. **60**(2): p. 270-6.
113. Brockstedt, S., et al., *Quantitative diffusion coefficient maps using fast spin-echo MRI.* Magn Reson Imaging, 1998. **16**(8): p. 877-86.
114. Nana, R., T. Zhao, and X. Hu, *Single-shot multiecho parallel echo-planar imaging (EPI) for diffusion tensor imaging (DTI) with improved signal-to-noise ratio (SNR) and reduced distortion.* Magn Reson Med, 2008. **60**(6): p. 1512-7.
115. Basu, S., T. Fletcher, and R. Whitaker, *Rician noise removal in diffusion tensor MRI.* Med Image Comput Comput Assist Interv, 2006. **9**(Pt 1): p. 117-25.

116. Gudbjartsson, H. and S. Patz, *The Rician distribution of noisy MRI data.* Magn Reson Med, 1995. **34**(6): p. 910-4.
117. Kristoffersen, A., *Optimal estimation of the diffusion coefficient from non-averaged and averaged noisy magnitude data.* J Magn Reson, 2007. **187**(2): p. 293-305.
118. Graumann, R., A. Oppelt, and E. Stetter, *Multiple-spin-echo imaging with a 2D Fourier method.* Magn Reson Med, 1986. **3**(5): p. 707-21.
119. Gulani, V., et al., *Improved time efficiency and accuracy in diffusion tensor microimaging with multiple-echo acquisition.* J Magn Reson, 2005. **177**(2): p. 329-35.
120. Hennig, J., M. Weigel, and K. Scheffler, *Multiecho sequences with variable refocusing flip angles: optimization of signal behavior using smooth transitions between pseudo steady states (TRAPS).* Magn Reson Med, 2003. **49**(3): p. 527-35.
121. Bretthorst, G.L., *Automatic phasing of MR images. Part II: voxel-wise phase estimation.* J Magn Reson, 2008. **191**(2): p. 193-201.
122. Bretthorst, L.G., *Automatic phasing of MR images. Part I: linearly varying phase.* J Magn Reson, 2008. **191**(2): p. 184-92.
123. Quirk, J.D., et al., *Optimal decay rate constant estimates from phased array data utilizing joint Bayesian analysis.* J Magn Reson, 2009. **198**(1): p. 49-56.
124. Tu, T.W., et al., *Full tensor diffusion imaging is not required to assess the white matter integrity in mouse contusion spinal cord injury.* J Neurotrauma, 2009.
125. Kim, J.H., et al., *Impact speed does not determine severity of spinal cord injury in mice with fixed impact displacement.* J Neurotrauma, 2009. **26**(8): p. 1395-1404.
126. Henkelman, R.M., *Measurement of signal intensities in the presence of noise in MR images.* Med Phys, 1985. **12**(2): p. 232-3.
127. Constantinides, C.D., E. Atalar, and E.R. McVeigh, *Signal-to-noise measurements in magnitude images from NMR phased arrays.* Magn Reson Med, 1997. **38**(5): p. 852-7.
128. Firbank, M.J., et al., *A comparison of two methods for measuring the signal to noise ratio on MR images.* Phys Med Biol, 1999. **44**(12): p. N261-4.
129. Kaufman, L., et al., *Measuring signal-to-noise ratios in MR imaging.* Radiology, 1989. **173**(1): p. 265-7.
130. Cohen, J., *A power primer.* Psychol Bull, 1992. **112**(1): p. 155-9.
131. Pipe, J.G., V.G. Farthing, and K.P. Forbes, *Multishot diffusion-weighted FSE using PROPELLER MRI.* Magn Reson Med, 2002. **47**(1): p. 42-52.
132. Bretthorst, G.L., *Bayesian Spectrum Analysis and Parameter Estimation.*, ed. G.J. Berger J FS, Krickeberg K, Singer B. 1988, New York: Springer-Verlag.
133. Biddle, F., March.E. and Miller,J.R. , *Research News.* . Mouse News Lett., 1973. **48**(24).
134. Readhead, C., et al., *Expression of a myelin basic protein gene in transgenic shiverer mice: correction of the dysmyelinating phenotype.* Cell, 1987. **48**(4): p. 703-12.
135. Chernoff, G.F., *Shiverer: an autosomal recessive mutant mouse with myelin deficiency.* J Hered, 1981. **72**(2): p. 128.
136. Griffiths, I., et al., *Axonal swellings and degeneration in mice lacking the major proteolipid of myelin.* Science, 1998. **280**(5369): p. 1610-3.

137. Brady, S.T., et al., *Formation of compact myelin is required for maturation of the axonal cytoskeleton.* J Neurosci, 1999. **19**(17): p. 7278-88.
138. Fenyes, D.A. and P.A. Narayana, *In vivo diffusion tensor imaging of rat spinal cord with echo planar imaging.* Magn Reson Med, 1999. **42**(2): p. 300-6.
139. Budde, M.D., et al., *Axonal injury detected by in vivo diffusion tensor imaging correlates with neurological disability in a mouse model of multiple sclerosis.* NMR Biomed, 2008. **21**(6): p. 589-97.
140. Budde, M.D., et al., *Axial diffusivity is the primary correlate of axonal injury in the experimental autoimmune encephalomyelitis spinal cord: a quantitative pixelwise analysis.* J Neurosci, 2009. **29**(9): p. 2805-13.
141. Harsan, L.A., et al., *Astrocytic hypertrophy in dysmyelination influences the diffusion anisotropy of white matter.* J Neurosci Res, 2007. **85**(5): p. 935-44.
142. Gulani, V., et al., *Apparent diffusion tensor measurements in myelin-deficient rat spinal cords.* Magn Reson Med, 2001. **45**(2): p. 191-5.
143. Harsan, L.A., et al., *Brain dysmyelination and recovery assessment by noninvasive in vivo diffusion tensor magnetic resonance imaging.* J Neurosci Res, 2006. **83**(3): p. 392-402.
144. Andrews, H., et al., *Increased axonal mitochondrial activity as an adaptation to myelin deficiency in the Shiverer mouse.* J Neurosci Res, 2006. **83**(8): p. 1533-9.
145. Kirkpatrick, L.L., et al., *Changes in microtubule stability and density in myelin-deficient shiverer mouse CNS axons.* J Neurosci, 2001. **21**(7): p. 2288-97.
146. Eftekharpour, E., et al., *Myelination of congenitally dysmyelinated spinal cord axons by adult neural precursor cells results in formation of nodes of Ranvier and improved axonal conduction.* J Neurosci, 2007. **27**(13): p. 3416-28.
147. Bando, Y., et al., *Differential changes in axonal conduction following CNS demyelination in two mouse models.* Eur J Neurosci, 2008. **28**(9): p. 1731-42.
148. Popovich, P.G., P. Wei, and B.T. Stokes, *Cellular inflammatory response after spinal cord injury in Sprague-Dawley and Lewis rats.* J Comp Neurol, 1997. **377**(3): p. 443-64.
149. Donnelly, D.J. and P.G. Popovich, *Inflammation and its role in neuroprotection, axonal regeneration and functional recovery after spinal cord injury.* Exp Neurol, 2008. **209**(2): p. 378-88.
150. Hausmann, O.N., *Post-traumatic inflammation following spinal cord injury.* Spinal Cord, 2003. **41**(7): p. 369-78.
151. Park, E., A.A. Velumian, and M.G. Fehlings, *The role of excitotoxicity in secondary mechanisms of spinal cord injury: a review with an emphasis on the implications for white matter degeneration.* J Neurotrauma, 2004. **21**(6): p. 754-74.
152. Oka, A., et al., *Vulnerability of oligodendroglia to glutamate: pharmacology, mechanisms, and prevention.* J Neurosci, 1993. **13**(4): p. 1441-53.
153. Pitt, D., et al., *Glutamate uptake by oligodendrocytes: Implications for excitotoxicity in multiple sclerosis.* Neurology, 2003. **61**(8): p. 1113-20.
154. Yin, X., et al., *Myelin-associated glycoprotein is a myelin signal that modulates the caliber of myelinated axons.* J Neurosci, 1998. **18**(6): p. 1953-62.

155. Edgar, J.M., et al., *Oligodendroglial modulation of fast axonal transport in a mouse model of hereditary spastic paraplegia.* J Cell Biol, 2004. **166**(1): p. 121-31.
156. McGavern, D.B., et al., *Axonal loss results in spinal cord atrophy, electrophysiological abnormalities and neurological deficits following demyelination in a chronic inflammatory model of multiple sclerosis.* Brain, 2000. **123 Pt 3**: p. 519-31.
157. McGavern, D.B., P.D. Murray, and M. Rodriguez, *Quantitation of spinal cord demyelination, remyelination, atrophy, and axonal loss in a model of progressive neurologic injury.* J Neurosci Res, 1999. **58**(4): p. 492-504.
158. Pitt, D., et al., *Dysmyelinated axons in shiverer mice are highly vulnerable to alpha-amino-3-hydroxy-5-methylisoxazole-4-propionic acid (AMPA) receptor-mediated toxicity.* Brain Res, 2010. **1309**: p. 146-54.
159. Sinha, K., et al., *Functional changes in genetically dysmyelinated spinal cord axons of shiverer mice: role of juxtaparanodal Kv1 family K+ channels.* J Neurophysiol, 2006. **95**(3): p. 1683-95.
160. Rasband, M.N., et al., *K+ channel distribution and clustering in developing and hypomyelinated axons of the optic nerve.* J Neurocytol, 1999. **28**(4-5): p. 319-31.
161. Anderson, T.E., *Spinal cord contusion injury: experimental dissociation of hemorrhagic necrosis and subacute loss of axonal conduction.* J Neurosurg, 1985. **62**(1): p. 115-9.
162. Simon, B.R., et al., *Porohyperelastic finite element analysis of large arteries using ABAQUS.* J Biomech Eng, 1998. **120**(2): p. 296-8.
163. Wu, J.Z., W. Herzog, and M. Epstein, *Evaluation of the finite element software ABAQUS for biomechanical modelling of biphasic tissues.* J Biomech, 1998. **31**(2): p. 165-9.
164. Miller, K. and K. Chinzei, *Mechanical properties of brain tissue in tension.* J Biomech, 2002. **35**(4): p. 483-90.
165. Bilston, L.E. and L.E. Thibault, *The mechanical properties of the human cervical spinal cord in vitro.* Ann Biomed Eng, 1996. **24**(1): p. 67-74.
166. Prange, M.T. and S.S. Margulies, *Regional, directional, and age-dependent properties of the brain undergoing large deformation.* J Biomech Eng, 2002. **124**(2): p. 244-52.
167. King, A.I., et al., *Recent advances in biomechanics of brain injury research: a review.* J Neurotrauma, 1995. **12**(4): p. 651-8.
168. Persson, C., J. Summers, and R.M. Hall, *The importance of fluid-structure interaction in spinal trauma models.* J Neurotrauma. **28**(1): p. 113-25.

Curriculum Vita

Tsang-Wei Tu
tut@wustl.edu
6605, Clayton Ave. #205, St. Louis, MO, 63139
Tel: (314) 484-0873; Fax: (314) 362-9996

EDUCATION

2011 Ph.D.,
Mechanical Engineering, Washington Univ., St. Louis, MO
2000 M.S.,
Hydraulic and Ocean Engineering, National Cheng Kung Univ., Tainan, Taiwan
1998 B.S.,
Hydraulic and Ocean Engineering, National Cheng Kung Univ., Tainan, Taiwan

EMPLOYMENT

2007 – Present Research Assistant, Biomedical MR Lab, Washington Univ., St. Louis
- In vivo DTI biomarkers of central nerve system white matter diseases.
- Biomechanical and pathological characteristics of traumatic spinal cord injury.

2004 – 2005 Associate Technical Specialist, Taitung County Government, Taiwan
- Harbor and marine planning; Numerical simulation and hydraulic experiment.

2002 – 2004 Assistant Scientist, Chemical Engrg., Institute of Nuclear Energy Research, Taiwan
- Nuclear Waste Management; Radionuclide, heat and mass transport modeling.

2000 – 2002 Hydraulic Engineer, Water Resources Agency, Ministry of Economic Affairs, Taiwan
- Hydraulic structure design and cadastral survey.

FUNDED RESEARCH

2009 – 2010 Principal Investigator, "Feedback determination of the biomechanical properties of rodent spinal cord using in vivo diffusion MRI", *University of Missouri Spinal Cord Injury Program,* $50,000

EXPERIENCES AND SKILLS

- Diffusion MRI; O-17 MR Spectroscopy; Automatic B0 Shimming.
- In vivo small animal MRI; Animal holder design; Live animal handling.
- Biomechanical simulation; Heat and mass transport modeling; Computational fluid dynamics; Hydraulic experiment and simulation.
- Animal surgery; Rodent models of spinal cord injury; MCAO stroke; Experimental autoimmune encephalomyelitis (EAE).
- Design and fabrication of actively decoupled Helmholtz and spinal cord surface RF coils.
- Sequence design and post acquisition signal/imaging processing.
- Tissue process and preparation; Immunohistology; Behavior assessment; Statistical analysis.
- Programming and software: CAD, Abaqus, AMIRA, ImageJ, SAS, Matlab, C++, FORTRAN

PUBLICATIONS

1. **Tu TW**, Kim JH, Wang J, Song SK, “Full tensor diffusion imaging is not required to assess the white matter integrity in mouse contusion spinal cord injury.” *Journal of Neurotrauma* 2010 Jan; 27(1):253-62.
2. Kim JH, **Tu TW**, Bayly PV, Song SK, “Impact speed does not determine severity of spinal cord injury in mice with fixed impact displacement.” *Journal of Neurotrauma* 2009 Aug; 26(8):1395-404.
3. **Tu TW**, Chang FL, Shih CF and Chuang WS, “Thermal analysis for spent nuclear fuel in deep geological disposal”, *Monthly Journal of Taipower’s Engineering* 2005 Jan; 677, 64-74
4. Twu SW, Liu CC, **Tu TW**, “Wave damping characteristics of vertically stratified porous structures under oblique wave action”, *Ocean Engineering* 2002 Sep; 29(11), 1295-1311

MANUSCRIPTS IN PREPARATION

1. **Tu TW**, Kim JH, Jakeman LB, Song SK, “The impact of myelination in locomotor functional recovery in spinal cord injury.” *Neurobiology of Disease*. (to be submitted)
2. **Tu TW**, Budde MD, Quirk JD, Xie M, Chen YJ, Song SK, “Improved in vivo multiple-echo diffusion tensor measurement using phased absorption images.” *NMR Biomedicine*. (to be submitted)
3. **Tu TW**, Bayly PV, Song SK, “Coexistence of remote vascular injury and local white matter injury in contusion spinal cord injury.” *Journal of Neurotrauma*. (in preparation)
4. **Tu TW**, Bayly PV, Song SK, “Feedback determination of mouse spinal cord material properties with diffusion MR and finite element analysis.” *Journal of Biomechanics*. (in preparation)
5. **Tu TW**, Wang Y, Chiang CW, Lin TH, Song SK, “Diffusion basis spectrum imaging detects evolving cell infiltration in EAE mice.” *BRAIN*. (in preparation)

CONFERENCE PRESENTATIONS

1. **Tu TW**, Bayly PV, Song SK, "Understanding the coexisting distal vascular and proximal axonal injuries in contusion spinal cord injury.”, *National Neurotrauma Symposium*, July 2011, Fort Lauderdale, Florida
2. **Tu TW**, Bayly PV, Song SK, "MRI of neural and vascular injury pattern in contusion spinal cord injury.”, *ISMRM*, May 2011, Montreal, Canada
3. Zhu XH, Chen J, **Tu TW**, Chen W, and Song SK, "Exploring the new utility of the 17O-MRS Imaging technique for studying CMRO2 and perfusion in stroke mice.” *ISMRM*, May 2011, Montreal, Canada
4. **Tu TW**, Budde MD, Quirk JD, Song SK, "Using absorption-mode images to improve *in vivo* DTI quality.”, *ISMRM*, May 2010, Stockholm, Sweden
5. **Tu TW**, Bayly, PV, Song SK, "Correlation of in Vivo DWI injury patterns with finite element analysis of mouse spinal cord injury.”, *ISMRM*, May 2010, Stockholm, Sweden
6. Spees WM, **Tu TW**, Song SK, and Garbow J, "Optimized single-acquisition lipid- and water-selective imaging at high field.”, *ISMRM*, May 2010, Stockholm, Sweden
7. Chen YJ, Kim JH, Wang J, **Tu TW** and Song SK, ”Increasing diffusion time improves in vivo DTI sensitivity to white matter degeneration.”, *ISMRM*, May 2010, Stockholm, Sweden
8. **Tu TW**, Kim JH, Song SK, "Less severe spinal cord injury in dysmyelinated mice evaluated using DTI and locomotion", *ISMRM*, May 2009, Honolulu, Hawaii

9. **Tu TW**, Kim JH, Huang JH, Song BR, Song SK, "Injury severity is independent on the impact speed between 0.1 and 0.4 m/s.", *National Neurotrauma Symposium*, July 2008, Orlando, Florida
10. Kim JH, **Tu TW**, Song BR, Song SK, "Long-term locomotor outcome predicted using hyper-acute in vivo diffusion tensor imaging.", *National Neurotrauma Symposium*, July 2008, Orlando, Florida
11. **Tu TW**, Kim JH, Song SK, "Sub-acute DTI predicts long-term behavioral outcome in the mouse model of spinal cord injury.", *ISMRM*, May 2008, Toronto, Ontario, Canada
12. **Tu TW**, Kim JH, Mingqiang Xie, Song SK, "Correlating the decreased axial diffusivity with morphological changes after axonal injury.", *ISMRM*, May 2008, Toronto ON, Canada
13. **Tu TW**, F.L. Chang, C.F. Shih and W.S. Chuang, "Thermal Analysis for engineer barrier system in deep geological disposal.", *International symposium on Nanotechnology and Energy*, April 2004, Hsinchu, Taiwan

TECHNICAL REPORTS

1. **Tu TW,** "Advanced application and exemplifications of FEHM package", *INER*, Mar. 2004, INER-2617
2. **Tu TW,** "On the applicability of thermal analysis computing packages in SNF deep geology disposal", *INER*, Oct. 2003, INER-2616
3. **Tu TW**, Hung CL, "Thermal analysis of engineer barrier system in nuclear fuel waste emplacement", *INER*, Oct. 2003, INER-2615
4. **Tu TW**, Lin CJ, Hung CL, "Geosphere assessment technique", *INER*, Aug. 2003, SNFD-INER-90-534